Master thesis and internship[BR]- Master's thesis : Numerical study of boundary layer stability and compressible flow phenomena in a high-speed low pressure turbine with elevated free-stream turbulence[BR]- Internship

Auteur : Deneffe, Nathan
Promoteur(s) : Hillewaert, Koen
Faculté : Faculté des Sciences appliquées
Diplôme : Master en ingénieur civil en aérospatiale, à finalité spécialisée en "aerospace engineering"
Année académique : 2023-2024
URI/URL : http://hdl.handle.net/2268.2/20839



UNIVERSITY OF LIÈGE - FACULTY OF APPLIED SCIENCES

NUMERICAL STUDY OF BOUNDARY LAYER STABILITY AND COMPRESSIBLE FLOW PHENOMENA IN A HIGH-SPEED LOW PRESSURE TURBINE WITH ELEVATED FREE-STREAM TURBULENCE

Master's Thesis conducted by Nathan DENEFFE

IN PARTIAL FULFILMENT OF THE REQUIREMENTS FOR THE DEGREE OF
MASTER OF SCIENCE IN AEROSPACE ENGINEERING

ACADEMIC SUPERVISOR
PR. KOEN HILLEWAERT

JURY MEMBERS
PR. VINCENT TERRAPON (*University of Liège*),
PR. SERGIO LAVAGNOLI (*von Karman Institute for Fluid Dynamics*),
DR. MARGAUX BOXHO (*Cenaero*)

ACADEMIC YEAR 2023 - 2024

Abstract

This work aims to study the flow through high-speed low pressure turbines encountered under on- and off-design conditions in geared turbofans. DNS are performed on the Belgian tier-1 cluster Lucia using the numerical solver ArgoDG implementing the discontinuous Galerkin method. Mach numbers of 0.7, 0.9 and 0.95 are considered combined with a Reynolds number of $70,000$. A free-stream turbulence intensity ranging between 2.8-3.0% at the blade is generated using a precursor turbulence injection method. The blade loading, the boundary layer, the wake behaviour as well as the separation and transition phenomena play key roles in flow physics. A direct comparison is performed with experimental data from the SPLEEN project and numerical data obtained with clean inlet conditions.

A close match with the experimental data is observed for blade loading and wake. In the subsonic case, a long separation bubble provoked by an adverse pressure gradient is observed at 61% of the suction side (SS). The flow reattaches before the trailing edge thanks to the flow transition enhanced by free-stream turbulence. In the transonic and the choked case, the shock spanning the flow passage considerably impacts the separation located approximately at 71% of the SS. The shock generates a strong compression followed by pressure recovery which first detaches the flow prematurely before its rapid reattachment. Throughout this separation bubble, the flow remains laminar even though an onset of transition is observed. The quasi-laminar nature impacts the BL characteristics and induces a strong momentum defect. Furthermore, observed losses increase with Mach number.

Acknowledgements

Firstly, I would like to express my deepest gratitude towards my academic supervisor, Pr. Koen Hillewaert, for guiding me through this research work with numerous advice and insights. His support and availability were of immense value in the progress of this study while the shared expertise fundamentally contributed to the quality and pertinence of the held discussions. Furthermore, I am very grateful for the passionate introduction and insights into the topic of turbomachinery he gave me. Through classes and lectures but especially in the context of this Master's thesis during the last few months, he stimulated my profound attention to this specific topic.

I want to dedicate special thanks to Dr. Margaux Boxho, research engineer at Cenaero, who assisted my journey with her crucial help, her expertise as well as all her positive energy. From the use of the supercomputing cluster to the implementation of the turbulence injection, her numerous pieces of advice were very precious in the process of this work. I also want to warmly thank Dr. Michel Rasquin, senior research engineer at Cenaero, who helped me several times with his valuable experience in HPC and high-fidelity simulations. Furthermore, I want to express my acknowledgement to all the other people at Cenaero with who I had the pleasure to interact on-site during the weekly visits.

I would like to express deep gratitude to Maxime Borbouse, PhD candidate at ULiège, for his countless pieces of advice as well as solutions to my encountered problems. His experience and know-how were of great importance throughout the complete length of this study. I want to additionally thank him for proofreading the present work, thus greatly contributing to its quality and coherence.

Furthermore, I want to express great thanks to the different people involved at the von Karman Institute for Fluid Dynamics (VKI). Special thanks are due to Pr. Sergio Lavagnoli who gave us interesting insights into the experimental facilities and approaches used at the VKI during the SPLEEN project. Its valuable comments based on its experimental expertise were of important value in the study and discussion of the observed flow phenomena. In this context, I acknowledge the support of the SPLEEN project funded by the European Union's Horizon 2020 research and innovation program.

I am very grateful to Cenaero for enabling the realization of this numerical study by supplying the necessary computational resources and tools, thus forming the framework for the present study. The computational resources have been provided by the Consortium des Équipements de Calcul Intensif (CÉCI), funded by the Fonds de la Recherche Scientifique de Belgique (F.R.S.-FNRS) under Grant No. 2.5020.11 and by the Walloon Region. The present research benefited from computational resources made available on Lucia, the Tier-1 supercomputer of the Walloon Region, infrastructure funded by the Walloon Region under the grant agreement n°1910247.

I also want to extend my gratitude to the members of my jury, who made the effort to read and evaluate the present work.

Last but certainly not least, I would like to thank the people in my direct environment, family and friends, for giving me precious support. Immense thanks hereby go to my parents who have always been present to help me and never stopped believing in me. Their commitment and dedication represent a huge inspiration for me such that my gratitude towards them can not be condensed into words. Special thanks also go to my girlfriend who supported me during this, sometimes stressful, period and never stopped pushing me towards a better self.

Contents

Nomenclature

Acronyms

APG	Adverse pressure gradient
BL	Boundary layer
CECI	Consortium des équipements de calcul intensif
CFD	Computational fluid dynamics
CPU	Central processing unit
DGM	Discontinuous Galerkin method
DHIT	Decaying homogeneous isotropic turbulence
DNS	Direct numerical simulation
DOF	Degree of freedom
FEM	Finite element method
FNRS	Fond national de la recherche scientifique
FSTI	Free-stream turbulence intensity
FVM	Finite volume method
GPU	Graphical processing unit
GTF	Geared turbofan
HPC	High performance computing
IBM	International Business Machines Corporation
LE	Leading edge
LES	Large eddy simulation
LPT	Low pressure turbine
ML	Machine learning
NN	Neural network
NSE	Navier-Stokes equation
PG	Pressure gradient
PS	Pressure side
RANS	Reynolds averaged Navier-Stockes
RMS	Root mean square
SPLEEN	Secondary and leakage flow effects in high-speed low-pressure Turbines
SS	Suction side
TE	Trailing edge
TI	Turbulent intensity
TKE	Turbulent kinetic energy
VKI	Von Karman Institute for Fluid Dynamics

Parameters

α	Flow angle
β	Blade metal angle
δ	Boundary layer thickness
δ^*	Boundary layer displacement thickness
ε	Dissipation
γ	Heat capacity ratio
κ	Wave number
λ	Stagger angle
Pr	Prandtl number
Re	Reynolds number
Ro	Roshko number
St	Strouhal number
μ	Dynamic viscosity
ν	Kinematic viscosity
ω	Vorticity
Φ_{ij}	Wavenumber velocity spectrum

ρ	Density
σ	Solidity factor
τ	Shear stress
θ	Boundary layer momentum thickness
ζ	Pressure loss coefficient
a	Speed of sound
c	Chord
c_f	Friction coefficient
c_p	Pressure coefficient
c_ax	Axial chord
d	Flow deviation
E	Spectral energy density
f	Frequency
g	Blade pitchwise spacing
H	Boundary layer shape factor
K	Acceleration parameter
k	Turbulent kinetic energy
L_ij	Integral length scale
M	Mach number
n	Normal distance
o	Blade throat opening
p	Pressure
R	Gas constant
R_ij	Velocity correlation function
s	Entropy
T	Temperature
t	Time
Tu	Turbulence intensity
u / v / w	Velocities related to the spatial coordinates
u_*	Friction velocity
x / y / z	Spatial coordinates
z_d	Spanwise thickness of domain

Indices and operators

$.'$	Fluctuating quantity
$.^+$	Quantity in wall units
$\cdot 0$	Total quantity
$\cdot \mathrm{ij}$	Matrix component
$\cdot \mathrm{in}$	Inlet quantity
$\cdot \mathrm{is}$	Isentropic quantity
$\cdot \mathrm{out}$	Outlet quantity
$\frac{\partial .}{\partial x_\mathrm{i}}$	Partial derivative (spatial)
$\frac{D .}{D t}$	Total derivative (temporal)
$\frac{d .}{d x_\mathrm{i}}$	Total derivative (spatial)
$\overline{.}$	Average quantity

1 Introduction

Due to their increased efficiency properties, turbofan engines are the most common engine types used for civil aircraft. They are based on the idea that the thrust is generated nearly exclusively by a fan which is driven by an internal engine. The latter is composed of combustion chambers as well as several compressor and turbine stages. Over the past decades, the goal has been to continually increase the efficiency of the engines thus leading to lower fuel consumption next to an overall lower weight enhanced by better performances. On the one hand, the thermodynamic efficiency can be optimized by improving the aerodynamic performances of the blades and the overall characteristics of each compressor and turbine stage. The use of new and better materials also increases efficiency since the stages can be operated at higher temperatures. Hence, more optimal flow conditions are created such that larger loadings as well as higher pressure ratios can be achieved. On the other hand, the propulsive efficiency can be improved by typically increasing the bypass ratio accorded to the fan. Nevertheless, this enlargement of the fan section can not be done indefinitely. Indeed, a limitation in traditional engines is that the fan and the low-pressure turbine (LPT) are interconnected via the low-pressure shaft. The rotation speeds of both components are thus intrinsically linked together. While the LPTs reach better performances for high rotation speeds, the rotation of the fan is constrained by emerging compressibility effects. Due to the large radius of the fan, the tip of the blades can experience sonic conditions even at moderate rotation speeds. If the rotations are too fast and supersonic conditions are reached, detrimental effects are observed, typically reducing the performance. The traditional solution was thus to limit the speed of the fan to the drawback of the LPT which then operated at suboptimal conditions. Hence, the slower rotation speed provokes a reduced loading of the LPT stages. To perform a given work on the flow, the LPT requires a large number of stages which has a fundamental impact on the engine size and weight. An innovative approach has emerged in the past decades based on the idea of decoupling the rotation of the fan and the LPT. In this context, Pratt & Whitney was the first to introduce a commercial engine concept, called the geared turbofan (GTF). The model of their PW1000G engine is shown Figure 1.1.

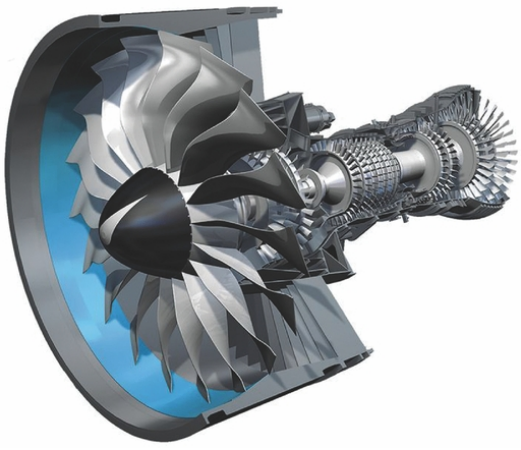

Figure 1.1: Schematic of the Pratt & Whitney PW1000G GTF, taken from [42].

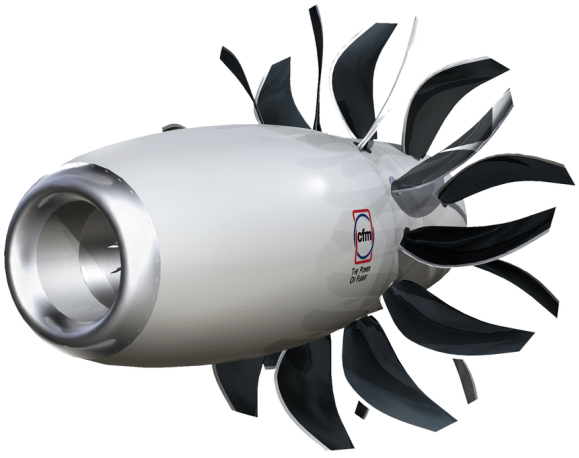

Figure 1.2: 3D model of the Safran open rotor concept, taken from [73].

The GTF engine is characterized by the presence of a complex gearbox transferring the energy from the LPT to the fan and potentially the low-pressure compressor. Hereby, the rotation speed is rescaled by a given ratio such that the fan as well as the LPT can operate under more optimal conditions. Using this technique, even larger bypass ratios can be considered. Propulsive efficiency can thus be further increased while having a reduced impact on the performance of the LPT. Beyond that, the LPT's higher induced rotation speeds lead to improved performances compared to traditional designs. Under such conditions, the high-speed LPT blades can be more loaded such that fewer stages may be necessary thus resulting in a potential weight reduction. The current design efforts of the major aeronautical acteurs in terms of civil aircraft propulsion all follow the idea of decoupling fans and LPT to allow higher bypass ratios. Nevertheless, other concepts, mainly at the prototype stage, exist to increase the propulsive efficiency and thus the overall performance of an engine. In this context, Safran is developing an open rotor concept following a similar idea with the overall goal of improving global efficiencies. A model of their developed prototype is shown in Figure 1.2.

Compared to the LPT in traditional turbofans, the high-speed LPT is characterized by fundamentally different operating conditions. Indeed, the higher rotation speeds lead to a mix of low Reynolds numbers with transonic flow conditions. The role played by compressible effects rises in importance under such conditions while classic LPTs remain in subsonic regimes. The low Reynolds number property limits the turbulent content of the flow while increasing the proneness to phenomena such as boundary layer (BL) separation. Especially the flow behaviour on the suction side (SS) of the LPT blade plays a fundamental role in terms of performance and loading. The presence of a bursting laminar separation bubble generating an open separation region would provoke a drastic rise in created losses and thus a collapse in performance. To counteract these detrimental effects, the blade design can be reviewed by adapting the shape in such a way as to optimise the blade loading (aft- or front-loaded). Alternatively, the premature transition of the flow can be considered as a further solution. Indeed, the transition leads to a turbulent regime governed by increased momentum transfers that exhibit beneficial characteristics. The presence of this flow regime allows the BL developing on the suction side to better resist the adverse pressure gradients and thus against a potential flow separation. The onset of transition can be induced by several means such that the types of transition can be categorized into different classes: natural, bypass, separated-flow or forced transition. Natural transition being the slowest type, the transition process can be accelerated by external flow features. For the bypass transition in LPT flows, such phenomena typically consist of free-stream turbulence or the effect of passing turbulent wakes. The fundamental behaviour of the interactions between transition and separation was assessed in [8], [24], [39]. The effect of free-stream turbulence on the transition and separation behaviour in LPT was studied in numerous studies as [2], [14], [17], [21], [40], [57]. Also, the wake-induced transition enhanced through the interaction with incoming wakes generated by upstream LPT stages has been investigated in [35], [37], [41], [66]. The mentioned works are either based on experimental measurements or numerical data obtained through simulations.

Several numerical approaches exist with different levels of fidelity. The highest fidelity is obtained with a Direct numerical simulation (DNS) which resolves all the length scales of the flow even the smallest ones. The latter are usually of turbulent nature and related to the viscous dissipation process. However, the precision comes to a significant cost in terms of computational resources required to run the simulation. Lower fidelity approaches such as the Large eddy simulation (LES) or even further the Reynolds averaged Navier-Stokes simulations (RANS) do not represent the flow with such an accuracy but are also considerably cheaper in terms of computation. To obtain a complete and in-depth view of the flow, high-fidelity approaches are required in order to correctly capture and describe the various features present in the flow field. Especially complex phenomena such as transition and separation require specific caution in order to be correctly predicted by a numerical approach. Since these features are omnipresent in the context of LPT flow, high-fidelity methods are required to adequately simulate these configurations and allow an in-depth understanding of the flow behaviour. For the study of LPT flows during the recent decades, a large range of configurations, geometries and operating conditions has been evaluated by varying the most important flow parameters and observing their induced effects. Nevertheless, some off-design conditions are still missing in-depth studies to assess the occurring detailed flow phenomena. This is the case especially for the high Mach number flows thus associated with transonic conditions in which compressible effects develop into dominating features. On an experimental basis, the Secondary and Leakage Flow Effects in High-Speed Low-Pressure Turbine (SPLEEN) project led by the von Karman Institute for Fluid Dynamics (VKI) [35] covered large condition ranges and described several different flow features such as the wake interactions and secondary flow effects. In terms of numerical approaches, the work of Bolyn [3] continued by Khateeb [30] and especially Borbouse [4] laid the groundstone to obtain reliable numerical data for the transonic regimes

considered in the SPLEEN experiments.

In [4], meaningful converged results were obtained for a Mach number range 0.7-0.95 and $\mathrm{Re} = 70 \times 10^3$ without any turbulence present in the free stream. The present work based on quasi-DNS constitutes the continuity of the discussions held in [4] such that the same flow configurations are considered with the addition that significant levels of turbulence are present in the flow field. By using a turbulence injection method, turbulent structures of a given intensity are added to the free stream before travelling downstream and interacting with the flow around the LPT blade. Hereby, the flow conditions are tuned to closely match the ones experienced experimentally such that comparisons can be drawn among both approaches. Also, the effect of free-stream turbulence will be assessed through direct comparison with the clean numerical simulations from [4]. The present study thus has the goal to further fill the gap existing between the available experimental data and the missing numerical counterpart. The fundamental ambition being the understanding of the flow fields around high-speed LPT as well as their associated complex flow features. This understanding in turn allows the development of improved models formalizing and describing the different flow phenomena encountered in LPT. To a larger extent, thus contributing to the design of more efficient LPT blades and flow configurations.

1.1 Methodology

As mentioned previously the present study can be seen as the continuation of [3], [30] and especially [4]. The fundamentals were thus laid in these works such that similar approaches and methodologies have been employed in the present work. Overall, the different tasks performed in the frame of this study are all contained within this report and explained accordingly following a decent chronology.

In chapter 2 the experimental background is introduced. From the experimental setup and instrumentation over to the flow conditions, the major aspects related to the experiments conducted by the VKI in the context of the SPLEEN project will be discussed. Specific attention will be given to the free-stream turbulence content of the flow experienced during the experiments. chapter 3 will investigate the flow in high-speed LPT. After assessing the geometrical specifications as well as the operating conditions, the quantification of the performances of LPT will be formalized. Then, the important flow phenomena encountered in turbine flows are considered. Therefore, specific sections are dedicated to turbulence physics, boundary layer behaviours as well as the wake generated by the blade. A detailed discussion of the flow features encountered in LPT flow based on previous studies and inspired by [4] is held in the continuity of the introduced phenomena. The chapter is closed with a brief introduction to the existing turbulence injection methods. chapter 4 is dedicated to the numerical tools used to facilitate the simulations. An important role is hereby played by the high-performance computing (HPC) field which allows the computation of large-scale simulation through the exploitation of parallelization. Nevertheless, considerable amounts of computational resources are required to perform such tasks. For this purpose, the tier-1 supercomputing cluster Lucia has been used. The implemented numerical method as well as the solver are briefly presented which respectively consist of the discontinuous Galerkin method (DGM) and ArgoDG. It follows chapter 5 providing the remaining computational framework of the numerical simulations. Indeed, the computational domain as well as the mesh needs to be defined and checked. Also, the definition of the boundary conditions as well as the numerical setup of the solver require specific attention. In order to extract meaningful results, the transitory of the simulation needs to be assessed by considering the convergence of the flow field based on significant physical quantities and fluxes. Closely related to the latter, the employed computational resources are investigated and quantified. Finally, the instrumentation of the numerical case is highlighted by describing the typical data that is extracted and used for postprocessing purposes. The chapter 6 includes all the different tasks and developments made in terms of turbulence injection. The method of choice consists of a precursor method which will be presented and explained in detail. With this kind of method, an auxiliary simulation is performed which solves the decay of homogenous and isotropic turbulence (DHIT) in a triply periodic domain. The different assumptions and limitations will be highlighted while the complete setup and procedures related to the precursor simulation are explained. Then, the final turbulence box is generated by blending the solution extracted from the auxiliary simulation. This chapter also integrates the discussion and evaluation of the turbulence injection in the main simulation. In this context, the evolution of the turbulence over the inlet region of the domain is considered in order to assess the turbulence level reaching the LPT blade. The turbulence intensity achieved at the blade level being satisfactory, yet some discrepancies related to the turbulence injection procedure are observable. These unexpected behaviours manifest in the form of anisotropy in the turbulence content and

may be ascribed to various reasons. Finally, chapter 7 contains the main numerical results obtained in the frame of this study consisting of high-speed LPT flows with free-stream turbulence. The analysis of the complete flow field is here fundamental to get an in-depth understanding of the flow before assessing more specific characteristics. Hereby, flow quantities such as the Mach number, the vorticity, the entropy or the numerical Schlieren are considered to highlight distinct flow features. Note that specific attention is brought to the compressible flow effects such as shock and acoustic perturbations. The blade loading is investigated to analyse the aerodynamic efforts applied to the blade by considering the isentropic Mach number as well as the skin friction coefficient. The boundary layer study marks another key topic. Indeed, by analysing the flow in close proximity to the blade, the separation and transition phenomena can coherently be described. Their mutual interactions will give rise to exhaustive discussions and observations. Finally, the wake region is considered which is characterized by the von Karman vortex street. This region of increased turbulent activity is typically one of the main indicators in terms of loss generation and thus performance of the blade.

2 Experimental background

An important role in the Secondary and Leakage Flow Effects in High-Speed Low-Pressure Turbines (SPLEEN) project is played by the von Karman Institute for Fluid Dynamics (VKI) which led a series of experiments in the context of high-speed low-pressure turbine flows. During the test campaigns, different flow configurations were investigated to better understand flow phenomena in low-pressure turbines (LPT) such as compressible effects, wake interaction, secondary flow structures, cavity purge/leakage flow effects and others. Overall, specifically designed turbine blades were tested under on- and off-design conditions to span the largest range of possible cases. A large experimental dataset containing the measurements of the different test cases was generated. Most of this collected data is openly accessible in [35].

The following description corresponds only to a brief introduction to what was investigated and accomplished during this experimental campaign at the VKI. Furthermore, it is mainly inspired by the documents and descriptions accessible in [35], [59], [67] as well as the discussions developed in [57], [58] which explore in more depth some of the observed phenomena.

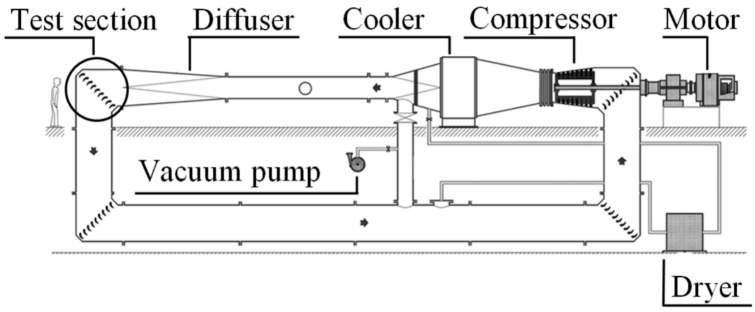

Figure 2.1: VKI S1-C wind tunnel, taken from [57].

A schematic of the VKI wind tunnel, used to carry out the test campaign is presented in Figure 2.1. This facility corresponds to a closed-loop wind tunnel driven by a 615 kW axial flow compressor. Initially, the facility was used to perform external aerodynamics experiments under supersonic conditions in a converging-diverging test section. Later, the layout was changed and a test section was specifically designed for the testing of linear turbine cascades. Instead of being located at its usual position in front of the diffuser, the test section was moved to the following elbow of the loop. This modification was done to handle the large deviation of the flow induced by the turbine blades. Next to a heat exchanger used to regulate the temperature and maintain ambient conditions, the vacuum pump rarifies the air and thus generates a lower total pressure in the closed-loop circuit. The fact that the test section can fit a large-scale LPT cascade model leading to quite high aspect ratios, enables the facility to handle high deviations as well as transonic exit conditions. Overall a wide range of conditions and regimes can be generated going from sea-level take-off to high-altitude cruising. This flexibility allows to satisfy the similarity conditions related to the exit Reynolds and Mach number which can typically be varied from $20,000$-$300,000$ and 0.6-1.2 respectively. These two quantities can be controlled independently by regulating respectively the total pressure induced by the vacuum pump and the compressor rotation speed.

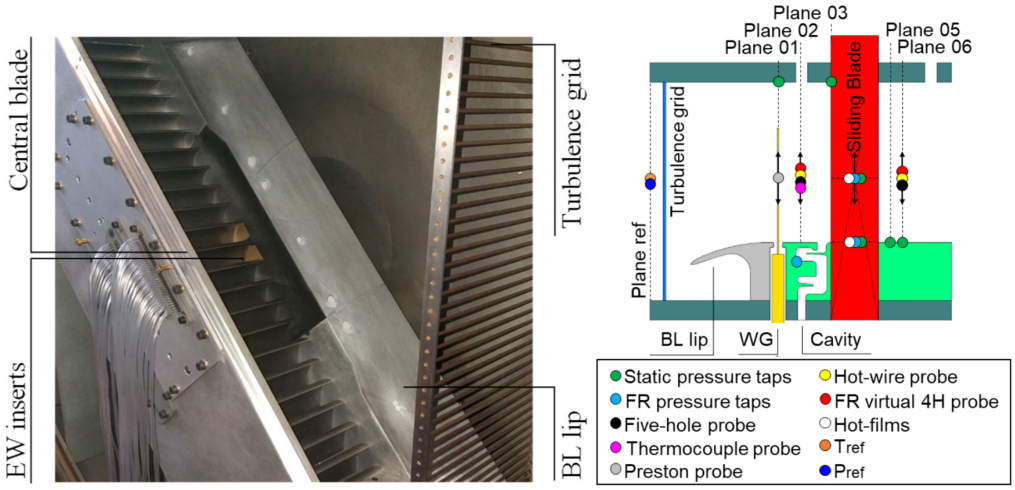

Figure 2.2: Picture **(left)** and schematic with the measurement planes and techniques **(right)** of the SPLEEN C1 cascade in the test section of the VKI S1-C wind tunnel, taken from [57].

Figure 2.2 shows a planar schematic view and a corresponding picture of the aforementioned wind tunnel test section. Different main elements can be noticed. Firstly, a turbulence grid is placed upstream of the cascade to generate free-stream turbulence in the flow. The grid is designed to reach turbulence levels of approximately 2.5% in terms of turbulence intensity (TI) at the blade level knowing that the background turbulence in the wind tunnel is about 0.9%. These topics directly related to the free-stream turbulence will be discussed in the following section in more detail. Secondly, a boundary layer lip is placed in front of the cascade to prevent the dirty boundary layer which developed throughout the upstream wind tunnel sections from reaching the test section. Indeed, the perturbations generated by interaction with the wind tunnel walls being present in the BL can potentially influence the flow behaviour as well as the measurements. Thirdly, a wake generator can be activated to simulate the presence of passing wakes related to upstream turbine stages. This wake generator is composed of 96 cylindrical bars mounted on a rotating axis. The diameters of the bars as well as the rotation speed are adaptable and can be tuned with respect to the adequate wake frequency, velocity and flow deviation. Finally, an injection and suction cavity system is present in front of the blade row to generate purge and leakage flows to evaluate their effect on the flow behaviour through the cascade.

The wake generator and the cavity flow are optional elements of the test section layout such that the experiments can be performed with or without them depending on which case is studied. Hence, three different experimental setups have been studied throughout the project: (1) no wake generator & no purge/leakage flow, (2) wake generator & no purge/leakage flow and (3) wake generator & purge/leakage flow. In the present study, only the first case is investigated in a numerical manner such that later comparisons and discussions will only be performed with this specific experimental case.

The different measurement planes and devices are presented in Figure 2.2. The measurement techniques are designed to extract significant data from the experiments not only to monitor the operating conditions but also to quantify the flow behaviour and properties. On the one hand, the upstream and downstream flow characteristics are measured by pneumatic wall static pressure taps, multi-hole pneumatic pressure probes, thermocouple sensors as well as miniature fast-response directional probes and hot-wires. Those quantities are typically extracted at specific planes but also at different pitchwise positions by using movable probes to obtain a complete view of the flow. On the other hand, the linear cascade is also equipped with surface pneumatic pressure taps, fast-response pressure sensors and hot-film gauges are used which are located on the central blade of the cascade as well as on the inner end walls. Overall, the cascade is constituted of around twenty individual blades but only the central one is equipped with several sensors. This specific blade is additionally designed in such a way that it is not only interchangeable but can also be slid along the spanwise direction, allowing measurements along the whole span of the blade. By doing so, complete time-resolved distributions can be generated for the quantities of interest which are in this case the velocity and pseudo shear stress.

2.1 Free-stream turbulence intensity

The free-stream turbulence is generated by a turbulence grid placed upstream of the blade. The TI level which is tried to be matched close to the blade in the experimental framework lies within the range of 1.5-3.5%. The passive grid is made out of a row of thin cylinders placed next to each other. The turbulence is created by interacting with the passing flow. The cylinders composing the grid have a diameter of 3 mm while the grid is characterized by a solidity factor σ of 0.25. Knowing the geometry of the turbulence grid, the important remaining parameter consists of the distance at which the grid is placed upstream of the blade. By varying this distance, the level of turbulence reaching the blade can be tuned. The grid position has been estimated by relying on the approach developed by Roach in [49]. The presented method consists of a combination of literature data and experimental measurements to provide the coefficients for the semi-empirical power law introduced by Frenkiel in [18] to model the decay of isotropic turbulence. The resulting correlation only depends on the grid geometry and thus neglects the flow conditions. Its expression is given by

$$Tu = A\left(\frac{x}{d}\right)^{-5/7}, \tag{2.1}$$

where A is the coefficient of the power law (typically set to 0.80 for a grid with parallel and round bars), x is the distance from the grid and d is the diameter of the bars. To achieve an adequate turbulence level of approximately 2.5%, the distance separating the grid from the LE of the blade is set to 400 mm. Following the decay law presented in Equation (2.1), the expected turbulence intensity at the blade level is equal to 2.42%. Knowing that the measurements are done at the reference plane 2 shown in Figure 2.2, the measured TI level should thus be equal to 2.59% at this location. Another flow property, which is interesting to characterize when considering free-stream turbulence, is the turbulent length scale. Therefore, Roach [49] introduced a second correlation which describes the evolution of the integral length scale. The corresponding semi-empirical law is defined as

$$\frac{L_x}{d} = I\left(\frac{x}{d}\right)^{2}, \tag{2.2}$$

where I is a constant usually equal to 0.2 for the type of turbulence grid considered. The predicted integral length scale at the blade and the reference measurement plane correspond respectively to 6.92 and 6.61 mm. Note that the length scale experiences growth when travelling downstream in opposition to the TI. Finally, the turbulence quantities measured with a hot-wire probe at the reference section in the wind tunnel are presented in Table 2.1. One can notice that the free-stream TI measured experimentally is slightly lower than the expected level of 2.59%. The TI reaching the blade should thus be accordingly smaller with respect to the targeted turbulence level. The deduced value of TI should nevertheless still be of satisfactory magnitude compared to the initial TI range targeted. More considerable differences are noticeable concerning the integral length scales. Indeed, the predicted value corresponds to nearly half of the measured quantity. Note that both the semi-empirical correlations from [49] and the experimental measurements use some weaker and some stronger hypotheses to obtain their values such that the observed deviations are not alarming in this context.

Table 2.1: Experimental inlet turbulence parameters measured with a hot-wire probe at plane 02 and averaged in the pitchwise direction.

Quantity	Units	Value
Tu	[%]	2.34
L_x	[mm]	12.05

3 Flow characteristics and generation of turbulent inflow data

The present chapter approaches all the different facets that are encountered when studying the flow through a high-speed low-pressure turbine. Starting with a section dedicated to the presentation of the geometrical specifications as well as the formalization of the operating conditions. Parallely, the most important parameters will be introduced to evaluate the turbine cascade performances when subjected to the passing flow. Afterwards, the attention is consecrated to the flow physics and thus the proper understanding of the flow features that appear in the flow field of a turbine blade. Firstly, the complex phenomenon of turbulence is detailed. After introducing some statistical tools and quantities, the physics behind turbulent flows are presented and some fundamental implications are mentioned. Secondly, boundary layers (BL) are discussed. Inspired by the structure used in [4], the general definition of a boundary layer is stated and its traditional layouts and behaviours are described. Specific phenomena as the separation of the BL from the surface or the transition of the BL from a laminar to a turbulent state are then the subject of further explanations. Thirdly, wakes generated by bodies submerged in a flow are studied and the particular case of the von Karman vortex street is illustrated and explained in more detail. Fourthly, a more precise look is taken at the results and flow fields of LPT cascades obtained by other previous studies. Inspired by [4], their works will be presented and compared among each other while the most significant flow features and results will be highlighted and discussed in depth. First, the separation and transition phenomena will be investigated in the context of LPT. Their influence on the generated losses is considered as well at this point. Then, the typical blade loading encountered in LPT is discussed by varying the most important parameters and observing their effects thus providing a better understanding of the complete flow physics. Finally, a direct analysis of the behaviour of the boundary layer is made. This last part is accompanied by a brief discussion of the compressibility effects occurring at transonic flow conditions in LPT. Note that particularly the flow on the blade suction side will be investigated due to its high importance in terms of performance and efficiency.

To close this chapter, a brief review of existing turbulence injection approaches is made. Indeed, several methods exist to numerically generate the turbulent inflow data. Popular approaches are synthetic methods which use analytical expressions to provide completely artificial fluctuations. Precursor methods on the other hand use an auxiliary simulation to provide a physical flow field but are thus linked to a more significant computational cost. These as well as some other known methods will be presented and compared with each other during the final part of this chapter.

3.1 High-speed low pressure turbine blades

In this first section, the preliminary knowledge regarding the flow in high-speed low-pressure turbine blades is presented. The specific flow conditions emerging with the appearance of new-generation turbines come with some fundamental changes. Indeed, a combination of high velocity and low Reynolds number is faced in such cases and specific flow features can be observed in the direct flow field. To address the problem in a rigorous manner, first, the geometrical specifications which define the layout of the low-pressure turbine passage will be explained in more detail. After introducing the most important geometrical parameters, the operating conditions

are discussed. By performing an adimensionalization process, the most relevant parameters, typically corresponding to the Mach number as well as the Reynolds number in such kind of applications, are established with respect to known flow quantities. Finally, the performance of an LPT is assessed. Therefore, the loading of the blade plays a fundamental role since it quantifies the aerodynamic loads applied to the blade. In this optic, next to the normal forces described by the pressure distribution around the blade also the tangential forces linked to the skin friction exerted on the blade can be evaluated. The deviation of the flow represents another important quantity in terms of the performance of a given blade design. Finally, the losses generated in the flow can be assessed. Especially the wake forms a region where high losses are generated due to its high turbulent content.

3.1.1 Geometrical specifications

The geometrical design of the turbine stage is an essential feature regarding the performance of the turbine. The blade is designed to redirect the flow while being subjected to a specific aerodynamic loading. Its shape is typically optimized to maximize the work performed by the blade for given flow conditions. Therefore, different physical phenomena and flow behaviours need to be understood and taken into account in order to improve a given blade shape as well as its overall performance. Not only the flow around the blade and the losses generated are important, but also the interaction between blade rows is essential. Additionally, the mechanical properties and structure as well as the reliability and the resistance to degradation are important aspects. A simplified and schematic view of a turbine stage is shown in Figure 3.1 in which some geometrical key parameters are highlighted.

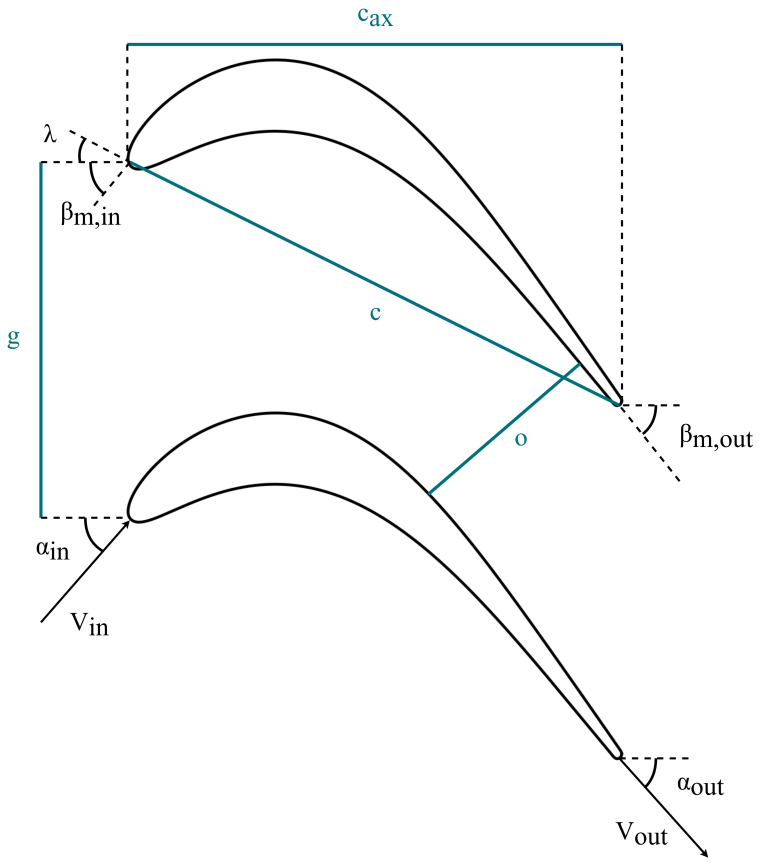

Figure 3.1: Schematic of the LPT cascade geometry with the SPLEEN blade.

The true chord c typically characterizes the size of the blade while the axial chord c_{ax} acts more as a size reference in the streamwise direction. The inlet and outlet metal angle ($\beta_{m,in}$ and $\beta_{m,out}$) represent the deflection of the blade and give an approximate measure of the expected deviation of the incoming flow. The stagger angle λ is defined as the angle between the true chord and the streamwise reference axis. The pitch g imposes the distance between adjacent blades in a given rotor or stator stage. This quantity directly impacts the throat opening o that

defines the minimum flow section existing between neighbouring blades. Thus the throat opening characterizes the maximum flow rate able to pass through the turbine stage for a given flow configuration. The solidity factor σ is given by the ratio of the true chord c over the pitch g. The trailing edge (TE) is designed in a circular shape with a characteristic diameter denoted d_{TE}. The flow will hit the blade at the leading edge (LE) with an inlet flow angle α_{in} at a given relative velocity V_{in} while it will depart from the TE with an outlet flow angle α_{out} at a relative outlet velocity V_{out}. Thus the flow is redirected by a certain angle when interacting with the blade row. This angle is called the turning angle. Note that the metal angles β_{m} and the flow angles α do not necessarily coincide. At the LE, the difference formed between the blade angle and the flow angle is called the incidence angle while at the TE the angular difference is denoted deviation angle.

The airfoil used in this study corresponds to the blade geometry used in the SPLEEN C1 cascade at the VKI which consists of an adapted version of the T106 blade. The actual blade, as it is used in a real engine, has been rescaled by a factor of 1.6 following the principle of similarity in order to experimentally reproduce the turbine flow configurations. The thickness of the TE was specifically enlarged to enable the installation of measurement devices on the blade. The solidity factor was specifically chosen to attenuate the separation on the SS. Overall, the adaptations all aimed to reproduce a flow as close as possible to the one in an actual turbine. To achieve this match, especially the pressure distribution was targeted to be reproduced correctly. Additionally, the adequate equipment of the experimental setup has to be considered in order to correctly measure the flow quantities of interest. The most important geometrical parameters are summarized in Table 3.1 with their respective values taken in the framework of this study.

Table 3.1: Geometrical parameters.

Parameter	c	c_{ax}	g	o	$\beta_{\mathrm{m,in}}$	$\beta_{\mathrm{m,out}}$	λ	d_{TE}
Unit	[mm]	[mm]	[mm]	[mm]	[°]	[°]	[°]	[mm]
Value	52.28	47.61	32.95	19.40	37.30	53.80	24.40	0.87

3.1.2 Operating conditions

The operating conditions play a fundamental role in the design as well as the final performance of turbines. As discussed previously, the development towards new kinds of turbines such as the GTF provokes a change in the typical established operating conditions of the LPT. In these new configurations, the turbine stages can thus be employed at higher rotational speeds compared to previous designs in which the LPT was limited in a direct manner by the rotation of the fan. This important change allows the LPT to be more performing and more efficient. Furthermore, one of the main goals of GTF consists of reducing the stage count of the LPT with these improved performances and so have a positive impact on the overall weight of the engine. In the past several studies have been conducted on the former operating points related to lower speeds thus a complete description of the flow mechanisms and features has been set up. With these new configurations emerging, the need for advanced knowledge and data regarding the physics in these flow conditions is present. Experimentally, several studies were performed on high-speed LPT as in [35], [65], [66]. From a numerical point of view, studies as in [5], [15], [17], [54] were already conducted. The work done in this thesis as well as the prior studies [3], [4], [30] dealing with conditions characterized by a low Re and transonic M are well in line with this goal. Note that next to the performance aspect, the operating conditions can also have an impact on the reliability of the turbine. Finally, the durability of the blades is also affected by these conditions since the blades will be more or less subjected to harsh flow conditions depending on the operation point.

While the operating regime of compressors is typically specified with respect to the inlet, the one of turbines is characterized by the outlet quantities. After performing a dimensional analysis of the case based on the principle of similarity [55], a reduced number of adimensional parameters are necessary to describe the flow. Overall, the 5 typical parameters (γ, Pr, α, M, Re) can be considered. Knowing that the perfect gas law is assumed to be applicable in the considered flow configurations, the heat capacity $\gamma = 1.4$ behaves as constant. Note that, Pr is the Prandtl number which defines the ratio of the momentum diffusivity over the thermal diffusivity. α stands for the flow incidence angle. From there, more specific adimensional parameters can be introduced for the study of turbine stages. The chosen characteristic quantities usually consist of the outlet isentropic Mach number

$M_{\text{is,out}}$, the outlet isentropic Reynolds number $\rho_{\text{is,out}}$ as well as the inlet and outlet flow angles (α_{in} and α_{out}). The Mach number which compares the flow velocity with respect to the speed of sound quantifies the compressibility effects encountered in the flow field. Its isentropic definition in terms of the outlet static conditions is given by

$$M_{\text{is,out}} = \sqrt{\frac{2}{\gamma-1}\left[\left(\frac{p_{0,\text{in}}}{p_{\text{out}}}\right)^{\frac{\gamma-1}{\gamma}} - 1\right]}, \tag{3.1}$$

where $p_{0,\text{in}}$ is the inlet total pressure, p_{out} is the outlet static pressure and $\gamma = 1.4$ is the heat capacity ratio. The Reynolds number in turn measures the ratio of the inertia forces over the viscous forces. It characterizes the proneness of the flow to transition to turbulence and thus conditions in a more general manner the turbulent activities. The Reynolds number which is widely used to quantify the operating conditions of the turbine cascades is defined by

$$\text{Re}_{\text{is,out}} = \frac{\rho_{\text{is,out}} U_{\text{is,out}} c}{\mu(T_{\text{out}})}, \tag{3.2}$$

where $\rho_{\text{is,out}}$ is the outlet isentropic density, $U_{\text{is,out}}$ is the outlet isentropic velocity, c is the chord of the blade and μ is the dynamic viscosity. The latter is defined as a function of the outlet static temperature T_{out} following the semi-empirical Sutherland's law established in [60]. Furthermore, the outlet static temperature is given in terms of the total inlet temperature $T_{0,\text{in}}$ and the isentropic outlet Mach number, such that

$$T_{\text{out}} = T_{0,\text{in}}\left(1 + \frac{\gamma-1}{2} M_{\text{is,out}}^2\right)^{-1}. \tag{3.3}$$

The outlet isentropic density and velocity can be obtained from the previously defined parameters by using respectively the perfect gas relation and the definition of the Mach number. This yields

$$\rho_{\text{is,out}} = \frac{p_{\text{out}}}{T_{\text{out}} R}, \tag{3.4}$$

$$U_{\text{is,out}} = M_{\text{is,out}} \sqrt{\gamma R T_{\text{out}}}, \tag{3.5}$$

where $R = 287.06$ [J K^{-1}kg^{-1}] is the gas constant.

3.1.3 Performance parameters

The global performance of a turbine stage can be characterized by several quantities. Important aspects to consider are the aerodynamic loading of the blade, the deviation of the flow as well as the loss present in the wake. Those quantitative parameters are especially useful for turbine designers. The latter will typically not try to understand every small instantaneous flow feature but, in a larger sense, try to optimize the performance of a blade shape by considering a defined set of parameters.

The blade loading corresponds to the aerodynamic forces exerted by the flow on the blade, thus characterizing the global momentum exchange between fluid and body. Two main contributions can traditionally be highlighted. One component of the force is given by the pressure distribution applied to the blade acting normal to the surface while the other component relates to the shear stress to which the blade is subjected. Straightforwardly, the pressure distribution can be studied by considering the pressure coefficient defined as

$$c_p = \frac{p - p_{\text{out}}}{\frac{1}{2}\rho_{\text{out}} U_{\text{out}}^2}, \tag{3.6}$$

where p is the static pressure and p_{out}, ρ_{out} and U_{out} are the isentropic outlet conditions commonly used as reference quantities. In practice, another parameter is often preferred to describe the pressure loading around the blade, the isentropic Mach number. It is an alternative way to express the pressure distribution, more specifically describing the velocity field around the apparent blade body thus also containing information about compressibility features. It is given by

$$M_{\text{is}} = \sqrt{\frac{2}{\gamma-1}\left[\left(\frac{p_{0,\text{in}}}{p}\right)^{\frac{\gamma-1}{\gamma}} - 1\right]}, \tag{3.7}$$

where the total inlet pressure $p_{0,\text{in}}$ is used as reference value. The second contribution to the blade loading is quantified by the wall shear stress distribution around the blade. The latter generates an effort tangential to the blade surface. Its definition is based on the near-wall velocity derivative such that the following expression is obtained,

$$\tau_\text{w} = \mu \left.\frac{\partial u}{\partial y}\right|_{y=0}, \tag{3.8}$$

where μ is the dynamic viscosity, y is the coordinate normal to the wall and u is the velocity tangential to the wall. An adimensional quantity can be derived from τ_w which corresponds to the skin-friction coefficient. As its name suggests it characterizes the friction that the blade is experiencing and it is mathematically defined as

$$c_\text{f} = \frac{\tau_\text{w}}{\frac{1}{2}\rho_\text{out} U_\text{out}^2}. \tag{3.9}$$

The direction of the flow plays a key role in terms of the performance of a cascade. The turbine blades are designed for an optimal inlet flow angle and should turn the flow by a specific angle in order to optimize the interaction between the following turbine stages. Indeed, wrongly tuned stages lead to suboptimal blade loading and reduced performances. Note that phenomena like separation typically happening on the suction side of the blade near the TE can have a non-negligible impact on the outlet flow angle. Thus, a precise understanding but also accurate predictions of these mechanisms are needed to correctly design the shape of the blades. Therefore, the flow deviation angle is introduced as a performance parameter. It is defined as the difference between the outlet flow angle and the outlet metal angle at the blades TE which translates as

$$d = \alpha_\text{out} - \beta_\text{m,out}. \tag{3.10}$$

The losses generated by the blade can be characterized by the pressure loss coefficient evaluated downstream of the blade thus in its wake. In this region, strong losses related to a significant total pressure drop can be observed which are mainly due to the important turbulence present in the wake. The total pressure loss coefficient is given in a general manner by the ratio

$$\zeta = \frac{p_{0,\text{in}} - p_{0,\text{out}}}{p_{0,\text{out}} - p_\text{out}}, \tag{3.11}$$

where $p_{0,\text{out}}$ and $p_{0,\text{in}}$ are respectively the inlet and outlet total pressure. Alternatively, one can also consider the entropy or the energy which are quantities containing similar information compared to the total pressure concerning the loss phenomena. Their loss coefficients are respectively defined as

$$\zeta_e = \frac{h_\text{out} - h_\text{is,out}}{h_{0,\text{out}} - h_\text{out}} \qquad \& \qquad \zeta_s = \frac{T_\text{out}\Delta s}{h_{0,\text{out}} - h_\text{out}}, \tag{3.12}$$

where h denotes the enthalpy. Denton has further formalized the study of losses in turbomachinery in [10] on which the following developments are based. Losses are thus ascribed to the generation of entropy through mainly four different mechanisms: (1) viscous effects in the BL, (2) friction in free shear layers typically encountered in mixing processes, (3) non-equilibrium phenomena such as shock waves and (4) heat transfer. Using entropy as a reference quantity represents a robust approach since it delivers a complete description and is independent of any rotations of the frame of reference. Through thermodynamics, the entropy state can be related to other properties of the fluid. By taking into account the perfect gas hypothesis, the change of entropy between two states is given by

$$s - s_\text{ref} = c_p \ln\left(\frac{T}{T_\text{ref}}\right) - R \ln\left(\frac{p}{p_\text{ref}}\right), \tag{3.13}$$

where the properties are either all total or all static quantities for the expression to be valid. Indeed both cases are true since the change from static quantity to its total value is done in an isentropic way. In the presence of an adiabatic and stationary flow, the total temperature becomes constant such that the temperature term in Equation (3.13) no more affects the entropy variation. Additionally, the previous expression can further be developed by assuming that the changes in total pressure are small. This yields

$$\Delta s = -R \ln\left(\frac{p_{0,2}}{p_{0,1}}\right) \approx -R\frac{\Delta p_0}{p_{0,1}}. \tag{3.14}$$

Through this reasoning, the measure of the total pressure becomes a good approximation to the evaluation of the entropy generation in order to assess the losses generated by the linear turbine cascade. Additionally, Denton

introduced a parameterized expression to model the total pressure loss coefficient. Its equation is obtained by considering the previously mentioned major contributors regarding the creation of entropy and is given by

$$\zeta = \frac{\Delta p_0}{\frac{1}{2}\rho U_{\text{ref}}^2} = \frac{C_{\text{p,b}} d_{\text{TE}}}{g} + \frac{2\theta}{g} + \left(\frac{\delta^* + d_{\text{TE}}}{g}\right)^2, \tag{3.15}$$

where θ and δ^* denote respectively the momentum and displacement BL thickness (see section 3.3), g is the pitchwise distance between the blades, d_{TE} is the TE diameter and $C_{\text{p,b}}$ is the base pressure coefficient. Thus, the second term corresponds to the boundary layer contribution (1). Indeed, strong viscous effects happen in the region close to the surface, also called the inner region of the BL (see section 3.3), which provoke the generation of entropy. Physically, this translates by heat that is generated through viscous shear work performed by the fluid. Since the entropy is mainly created in the inner layer, it should be relatively insensitive to the state of the boundary layer. In flow conditions where both turbulent and laminar BL regimes are possible, it was observed that a turbulent BL generates considerably more entropy compared to its laminar counterpart. This leads us to the importance of correctly understanding and predicting the BL transition phenomena for the studied turbine blade. The Mach number should not greatly affect the entropy generation which is also linked to its small influence on the skin friction. The pressure gradient present in the flow has in turn a considerable impact on the entropy generation such that adverse pressure gradients are usually linked to larger entropy creations. The first and third terms of Equation (3.15) relate to mixing processes characterized by free shear layers generating entropy (2). Those appear as soon as a rate of shear strain is applied to the fluid. For turbine blades, they are specifically present in the direct wake of the blade but also in separation regions (see subsection 3.3.1). Since the processes are highly localised phenomena, it is difficult to model them properly. Nevertheless, one can accurately quantify the overall entropy creation by using conservation laws inside of a defined control volume. Using this approach, the previously introduced base pressure coefficient can be expressed as

$$C_{\text{p,b}} = \frac{p_{\text{b}} - p_{\text{ref}}}{\frac{1}{2}\rho U_{\text{ref}}^2}. \tag{3.16}$$

The base flow is the flow region directly downstream of the TE, the coefficient describes the entropy creation linked to the mixing between the wake and the main flow. The specific flow phenomena related to the trailing edge of the blade are presented in more detail in [56]. In the presence of open separation regions reaching the TE of the blade, the apparent diameter of the TE is increased leading to important additional losses. The third term of Equation (3.15) contains this extra loss due to separation. The specific contribution is approximated as a function of the displacement thickness and the TE diameter and writes

$$\zeta_{\text{sep}} = \frac{(\delta^*)^2 + 2t\delta^*}{g^2}. \tag{3.17}$$

The dependency of the losses to the square of δ^* indicates its significant impact on the losses as soon as large separations are present while the inferred losses remain negligible for small separations. Note that Equation (3.15) neither takes into account the entropy creation due to shocks (3) nor the one linked to heat transfer (4). Next to that, unsteady flow features such as the von Karman vortex street or the viscous decay of eddies downstream of the blade which are considerable entropy sources are not quantified by this approach.

The entropy generated by non-equilibrium phenomena such as shock waves (3) can be ascribed to the heat conduction and strong normal viscous stresses inside of the shock. By developing the equations for a normal shock, one can find that the entropy creation scales to the cube of $(M^2 - 1)$. This concept can also be applied to oblique shocks which are encountered way more often in real turbine applications. For the oblique shocks, the losses are exclusively conditioned by their normal component and overall their corresponding losses are typically small compared to the other main contributors. In turbines, the effects of shocks are usually not desired due to the compression work that is performed by the shock on the flow. However, the presence of shocks only gets problematic when a shock system builds up downstream of the trailing edge. In this case, the flow will expand around the TE but will then be strongly compressed by the shock which will provoke strong viscous dissipation and thus lead to significant TE losses. The source of entropy represented by the heat transfer (4) is usually negligible in turbine applications. This is especially true in the studied case since the flow is considered as adiabatic and no heat exchange with the surroundings is possible.

3.2 Turbulence

In this section, the fundamentals of turbulent flows are presented which are required for a proper understanding of flow features encountered in the frame of this study. In the first approach, some tools are presented to adequately describe turbulence. Next to the definitions of basic statistic variables such as averages and correlations, more specific quantities are introduced regarding the turbulence frame. In this view, the integral length scales as well as the energy spectra are presented. In a second approach, the physics of turbulent flows are introduced. Turbulence being characterized by chaotic flow behaviour combined with coherent vortical structures manifests some fundamental properties which will be addressed. Then, the notion of energy cascade as well as the idealized view of homogeneous and isotropic turbulence (HIT) will be discussed and its corresponding implications in the spectral domain will be illustrated. Afterwards, the Reynolds decomposition and the Reynolds averaged Navier-Stokes (RANS) equations are presented while briefly addressing the related challenges faced by this approach in terms of modelling. In this frame, important quantities such as the turbulent kinetic energy (TKE) and the turbulent intensity (TI) will be defined for later usage regarding the characterization of the turbulent content of the studied flow. Finally, the attention is dedicated to the frozen-turbulence hypothesis introduced by Taylor which has significant implications in terms of the employed numerical and experimental approaches.

3.2.1 Statistics and correlations

Based on [46], one can consider an unknown random variable U which is allowed to take values inside a sample space V. The statistical behaviour of U can described based on a probabilistic approach. When a realization is made meaning that U takes a value inside of V, certain events can happen and become true with given probabilities. The cumulative distribution function F (CDF) can be introduced to describe the behaviours of these events since it defines the probability of U being smaller than a certain value of V, written $F(V) \equiv P(U < V)$. From there, the probability density function f can be obtained which consists of the derivative of the CDF with respect to the sample space V. Its integral over a portion of the sample space defines the probability of U belonging to this given interval of V, such that

$$P(V_\mathrm{a} < U < V_\mathrm{b}) = \int_{V_\mathrm{a}}^{V_b\mathrm{b}} f(V)dV. \tag{3.18}$$

By definition, the probability density function satisfies the following properties

$$f(V) \geq 0, \qquad \int_{-\infty}^{+\infty} f(V)dV = 1. \tag{3.19}$$

Different quantities can additionally be introduced to describe the statistical distribution and behaviour of U. Therefore, statistical moments are of great interest. These moments can be evaluated in countless orders, each describing more specific characteristics of the distribution. The first-order moment, known as the mean, is defined as

$$\langle U \rangle = \int_{-\infty}^{+\infty} V f(V)dV, \tag{3.20}$$

and gives the expected values of U. So it basically corresponds to the mean value of U. The second-order moment describes the typical deviation from this mean value. The so-called variance is given by

$$\sigma_U^2 = \int_{-\infty}^{+\infty} (V - \langle U \rangle)^2 f(V)dV. \tag{3.21}$$

Finally, this process can be continued all over again to evaluate higher-order moments. The n^{th}-order moment is given in a generic manner by

$$\mu_n = \int_{-\infty}^{+\infty} (V - \langle U \rangle)^n f(V)dV. \tag{3.22}$$

Note that the 3^{rd}- and 4^{th}-order moments are respectively known as the skewness and the flatness factors. In the presence of a series of N independent identically distributed (i.i.d.) random variables $U^{(i)}$, an arithmetic average can be performed on these samples in order to determine the mean of the ensemble. Following the central-limit theorem, the expected value of the computed ensemble average should converge to the true expected value of the random variable U, when N becomes large enough. Yielding

$$\langle U \rangle_N \equiv \frac{1}{N} \sum_{n=1}^{N} U^{(n)} \quad \Rightarrow \quad \langle \langle U \rangle_N \rangle = \langle U \rangle. \tag{3.23}$$

This theorem has important implications in the computation of averages in all kinds of applications. Hence, the possible procedures to evaluate averages become all equivalent under those circumstances. The estimation of the average is no longer limited to be based only on distinct realizations but can also be complemented by temporal or spatial averages, respectively written as

$$\langle U \rangle_T \equiv T^{-1} \int_0^T U(t)dt, \qquad \langle U \rangle_S \equiv S^{-1} \int_S U(\mathbf{x})d\mathbf{x}. \tag{3.24}$$

The covariance of two random variables corresponds to their mixed 2$^{\text{nd}}$-order statistical moment. This quantity can be further developed to the correlation coefficient which is defined by the ratio of the covariance divided by the product of the variances of both variables. It describes the existing correlation and thus in a wider sense the mutual influence of both variables on each other. In the frame of this study, a closely related parameter that is worth introducing is the two-point, one-time autocovariance given by

$$R_{ij}(\mathbf{x},\mathbf{r},t) = \langle u_i(\mathbf{x},t) u_j(\mathbf{x}+\mathbf{r},t) \rangle. \tag{3.25}$$

The autocovariance describes the influence of a parameter value on its own value at a later time. In Equation (3.25), the correlation between the velocity at a given point and time and its value at some distance from the initial point is evaluated. From this expression, one can deduce a characteristic length scale quantifying the distance at which the parameters influence is still sensible in a significant manner. This leads us to the integral length scale which is defined by

$$L_{ii}(t) = \frac{1}{R_{ii}(0,t)} \int_0^\infty R_{ii}(\mathbf{e}_i r,t)dr, \tag{3.26}$$

where i refers to a specific direction in space. Furthermore, the wavenumber velocity spectrum can be introduced which corresponds to the Fourier transform of the two-point correlation defined in Equation (3.25). It is given by the following integral expression:

$$\Phi_{ij}(\kappa,t) \equiv \frac{1}{(2\pi)^3} \iiint_{-\infty}^{+\infty} e^{-i\kappa\cdot\mathbf{r}} R_{ij}(\mathbf{r},t)d\mathbf{r}, \tag{3.27}$$

where κ is the wavenumber. It basically contains two types of directional information, one related to the velocity components and the other related to the direction of κ. By removing this directionality, one can establish the spectral energy density which is defined as

$$E(\kappa,t) \equiv \iiint \frac{1}{2}\Phi_{ii}(\kappa',t)\delta(|\kappa'|-\kappa)d\kappa'. \tag{3.28}$$

3.2.2 Turbulent flow

Turbulent flows are characterized by strong mixing and momentum transfer induced by coherent flow structures (see [9], [45], [46]). The turbulent behaviour of the flow depends on a major parameter which is the Reynolds number describing the ratio of inertial over viscous forces. In the presence of large Re, the non-linear terms of the NSE tend to become dominant leading to a chaotic flow shaped by strong instabilities and fluctuations. The turbulent flow features are three-dimensional, coherent structures existing in a large range of length scales where the size conditions their behaviour in the flow. The largest ones are typically dictated by the flow geometry and contain the largest amounts of energy while the smallest structures are associated with large velocity gradients and contribute to the dissipation of the energy through viscosity. In real applications, turbulence is omnipresent often reducing the laminar flow state to an exceptional flow behaviour. Its apparently chaotic nature leads to an instantaneous flow field characterized by random realizations. Hence, turbulent flows are assumed to be non-reproducible but some flow statistics can be assessed and used to describe the turbulence as will be detailed later. The coherent structures present in a turbulent flow are known as vortices or eddies which correspond to an organized region of vorticity. The latter, noted ω, is defined as the rotation of fluid particles around their own axis which can be written mathematically as

$$\omega = \nabla \times \mathbf{u}. \tag{3.29}$$

The unsteadiness combined with advection inside of the turbulent flow will provoke the stretching of the vortical structures. By doing so, smaller vortices are fed through the passing of the energy to the smaller scales. This continuous process will lead to the creation of small-scale fluctuations which will be spread by diffusion before being dissipated by viscosity. Note that the previously discussed features apply to 3D turbulence but are not

necessarily true for 2D cases. Indeed, the vortex stretching is not able to occur properly in 2D turbulent flows. In such cases, eddies are not decomposed into smaller ones by passing on their energy but will interfere and potentially assemble together leading to the creation of larger vortices. This process is known as the inverse energy cascade.

The first one to introduce the notion of energy cascade in the field of turbulence was Richardson in 1922 [48]. According to his view, turbulence consists of an aleatory superposition of different-sized vortices. The largest eddies are created by perturbations in the mean flow and are by nature unstable. By continuously breaking up into smaller eddies, the cascade is stopped by viscous dissipation at the smallest scales η where $u_\eta \eta/\nu \approx 1$. The rate at which the turbulent kinetic energy is dissipated is given by

$$\varepsilon = 2\nu \left\langle \frac{\partial u_i'}{\partial x_j} \frac{\partial u_i'}{\partial x_j} \right\rangle. \tag{3.30}$$

The energy cascade is by definition inviscid and conserves the energy when passing it from the large to the small scales. By performing a dimensional analysis of the energy cascade, one can deduce that the smallest scales are set by viscosity as $\eta = (\nu^3/\varepsilon)^{1/4}$ and are proportional to $\eta \sim \mathrm{Re}^{-3/4} l$ thus getting smaller with increasing Re.

In 1941, Kolmogorov further formalized this vision of turbulence [32]. Overall, he emitted three main hypotheses to develop his idealized view regarding the statistics of a turbulent flow characterized by $\mathrm{Re} \gg 1$. Firstly, the assumption of local isotropy (1) describes that the directional information is lost when reaching the smallest scales. Thus, the velocity spectrum $\Phi_{ij}(\kappa)$ can be completely determined by the energy spectrum $E(\kappa)$ under these conditions. Secondly, the first assumption of similarity (2) concerns again the smallest scales. Indeed, these scales are assumed to be universal while depending only on the flow properties ν and ε. This has a fundamental implication on the energy spectra E reducing to a universal function of κ, ν and ε, such that

$$E(\kappa) = \varepsilon^{2/3} \kappa^{-5/3} \Psi(\kappa\eta), \tag{3.31}$$

where $\Psi(\kappa\eta)$ corresponds to the Kolmogorov compensated spectrum function. Finally, the second hypothesis of similarity (3) states that an inertial subrange exists whose scales depend only on ε. The implication regarding the energy spectrum translates as

$$E(\kappa) = C\varepsilon^{2/3} \kappa^{-5/3}, \tag{3.32}$$

where C corresponds to a coefficient obtained for $\Psi(\kappa\eta)$ in the limit $\kappa\eta \to 0$. The established power law for the energy spectrum of homogeneous isotropic turbulence (HIT), which has been verified experimentally, is illustrated in Figure 3.2. One can notice that the major part of the energy is indeed contained in the large scales. The largest scales are furthermore described by $\sim \kappa^2$ before reaching a maximum at κ_0. The inertial subrange is characterized by the $-5/3$ slope describing the energy cascade linking large and small scales. An abrupt decrease in the energy spectrum can be observed in the smallest scales which is provoked by the viscous dissipation.

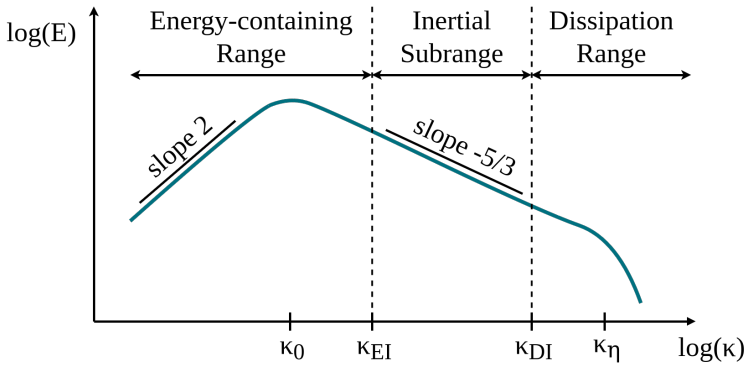

Figure 3.2: Typical energy spectrum for an ideal turbulent flow (HIT), reproduced from [46].

The random character of a turbulent flow makes it a highly unsteady phenomenon. Even though instantaneous snapshots of the flow seem chaotic, their statistics are typically assumed to be well-defined. Simple statistical

tools have been introduced to take advantage of this characteristic. The most famous approach consists of decomposing the actual flow velocity u in the sum of two contributions: the mean velocity $\overline{u}$ and the velocity fluctuation u'. The procedure is known as the Reynolds decomposition. By applying this approach to the NS flow equations, the Reynolds averaged Navier-Stokes equations (RANS) can be obtained. Considering the unsteady momentum conservation equation, its Reynolds averaged version is given by

$$\begin{aligned} \frac{\partial(\rho\overline{u}_\mathrm{i})}{\partial t} + \frac{\partial(\rho\overline{u}_\mathrm{i}\overline{u}_\mathrm{j})}{\partial x_\mathrm{j}} &= -\frac{\partial\overline{p}}{\partial x_\mathrm{i}} + \frac{\partial}{\partial x_\mathrm{j}}\left(\overline{\tau}_\mathrm{ij} - \rho\overline{u'_\mathrm{i}u'_\mathrm{j}}\right), \\ \text{where} \quad \overline{\tau}_\mathrm{ij} &= \mu\left(\frac{\partial\overline{u}_\mathrm{i}}{\partial x_\mathrm{j}} + \frac{\partial\overline{u}_\mathrm{j}}{\partial x_\mathrm{i}} - \frac{2}{3}\delta_\mathrm{ij}\frac{\partial\overline{u}_\mathrm{m}}{\partial x_\mathrm{m}}\right). \end{aligned} \tag{3.33}$$

Note that next to the mean flow quantities, a single additional term emerges due to the non-linearity of the equations. It corresponds to the averaged product of the velocity fluctuations given by $\rho\overline{u'_\mathrm{i}u'_\mathrm{j}}$ and is referred to as Reynolds stresses. This new variable represents a crucial quantity in turbulence by characterizing the velocity fluctuations present in the flow. Being an additional unknown in the equations, it causes a closure problem regarding the RANS equations. The most direct solution to this issue consists of modelling the most accurately as possible the new term to close the system and thus to be able to solve the simplified set of NSE. This procedure represents an important challenge in the field of turbulence and is discussed in many works (see [16], [45]). From the Reynolds stresses, another significant quantity can be derived known as the turbulent kinetic energy (TKE). It is related to the trace of the Reynolds stress tensor and characterizes the magnitude of the turbulent content in the flow. The TKE contains no directional information and is commonly defined as

$$k = \int_0^\infty E(\kappa)d\kappa = \frac{1}{2}\overline{u'_\mathrm{i}u'_\mathrm{i}}. \tag{3.34}$$

Additionally to the TKE, the turbulence intensity (TI) can be introduced which represents a normalized version of TKE. Similar to k, it describes the overall turbulence level of the flow. The TI is normalized with respect to the free-stream velocity of the flow U_∞ and its expression is given by

$$Tu = \sqrt{\frac{2}{3}\frac{k}{(U_\infty)^2}}. \tag{3.35}$$

An important hypothesis which will be exploited widely in the frame of this study is the frozen-turbulence approximation [61]. Also known as Taylor's hypothesis, it basically describes the conversion from a temporal to a spatial spectra based on the convection velocity of the flow U_c. The assumption thus allows the conversion of a time signal $u(t)$, for instance, measured by a sensor into a spatially coherent signal $u(x)$. Next to homogeneity, it requires the convective time of the flow to be much smaller than the turbulent time scales. In other words, the convective velocity should be way larger than the turbulent fluctuations. By developing this idea, one can introduce the TKE which quantifies exactly these turbulent fluctuations. Successively, one obtains

$$U_\mathrm{c} \gg \langle u^2\rangle^{1/2} \quad \Rightarrow \quad \sqrt{k}/U_\mathrm{c} \ll 1. \tag{3.36}$$

Since the convection velocity in many cases equivalently corresponds to the mean flow and thus to the free-stream velocity, it can be concluded from Equation (3.35) and Equation (3.36) that for the frozen-turbulence hypothesis to be valid, the TI needs to be small [16]. On the one hand, the hypothesis has significant implications in the experimental approach since most sensor measurements, especially the ones concerning turbulence quantities, are performed under this assumption [35]. On the other hand, the procedure of turbulence injection detailed in chapter 6 is based on the frozen-turbulence assumption. The turbulent fluctuations extracted from a precursor turbulence box simulation are injected at the inlet section by being superimposed with the convective inlet velocity. The turbulent flow is thus generated by combining a mean flow with velocity fluctuations which according to Taylor's hypothesis should be small compared to the mean velocity to be valid.

3.3 Boundary layer

Following the ideas developed by Schlichting and Gersten [53], the boundary layer represents a thin region close to the wall in which the relative velocity of the fluid transitions from zero to the free stream velocity. This velocity

variation is possible through the dominant effect played by the viscosity of the fluid in the near-wall region. A velocity gradient normal to the wall is present inside the boundary layer characterizing the velocity distribution. The BL usually grows in thickness along the surface when advancing downstream. This spatial evolution depends on different parameters such as the flow velocity, geometry and fluid properties but also on the flow state which can be either laminar, turbulent or in transition between both regimes. Another important characteristic of the boundary layer is that it is typically thinner for a higher Reynolds number, *e.g.* lower viscosity.

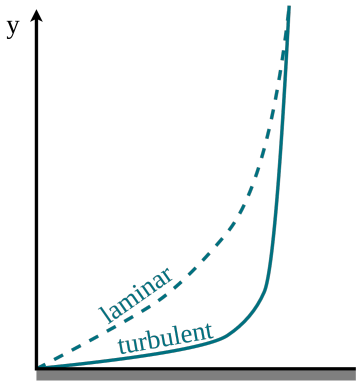

Figure 3.3: Schematic view of laminar and turbulent velocity profiles in a boundary layer, reproduced from [33].

By developing the NSE under certain hypotheses, one can obtain the BL equations. They approximate the evolution of the flow in the region close to the wall. Using theoretical relations such as the von Karman momentum integral equation or even empirical correlations, self-similar solutions for the velocity profiles can be determined for different cases. An important note is that, depending on the flow regime, the boundary layer behaves differently and the flow physics changes. As is illustrated in Figure 3.3, a turbulent boundary layer will typically grow faster and thus have a larger thickness than a laminar one. Simultaneously, the turbulent BL has larger velocity gradients along the wall-normal direction such that larger shear stress is present leading to higher friction losses. However due to the turbulent mixing defined by a strong momentum exchange the turbulent BL is more resistant to potential separations compared to a laminar BL.

Multiple physical quantities are used to describe a BL, but commonly the following ones are preferred [53]:

- the boundary layer thickness δ,
- the wall shear stress τ_w or the skin-friction coefficient c_f introduced respectively in Equation (3.8) and Equation (3.9) to estimate the friction forces exerted,
- the displacement thickness δ^* to represent the deviation of the streamlines induced by the presence of the BL:

$$\delta^*(x) = \int_0^\infty \left(1 - \frac{\rho}{\rho_e}\frac{u}{U_e}\right) dy, \tag{3.37}$$

  where x and y are the coordinates respectively tangent and normal to the surface while $U_e(x)$ denotes the local free stream velocity. Note that density factors account for compressibility effects.

- the momentum thickness θ that quantifies the drag force generated:

$$\theta(x) = \int_0^\infty \frac{\rho}{\rho_e}\frac{u}{U_e}\left(1 - \frac{\rho}{\rho_e}\frac{u}{U_e}\right) dy, \tag{3.38}$$

- the shape factor H given by:

$$H = \frac{\delta^*}{\theta}. \tag{3.39}$$

  It describes in a complementary manner the state of the BL such that for $H > 2$ the BL is in a laminar regime. For lower values than 2, typically around 1.4 the BL is in turbulent regime.

For more coherence, a convenient non-dimensionalization is introduced. First, the friction velocity u_* is defined at the level of the wall

$$u_* = \sqrt{\frac{\tau_w}{\rho}}. \tag{3.40}$$

From there, one can deduce the different wall units

$$n^+ = \frac{nu_*}{\nu},\ s^+ = \frac{su_*}{\nu},\ U^+ = \frac{\overline{U}}{u_*}, \tag{3.41}$$

where n and s correspond to the distance in the normal and tangential direction with respect to the surface, respectively.

It is well known that the boundary layer can be decomposed into several regions in which different phenomena are dominant, thus leading to distinct behaviours. As discussed in [63] and illustrated in Figure 3.4, one can differentiate between the three main regions.

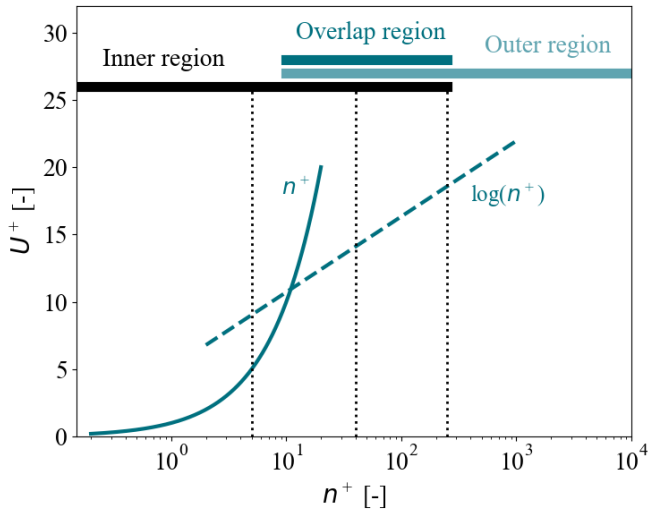

Figure 3.4: Asymptotic shape of the turbulent velocity profile close to the surface, reproduced from [63].

Firstly, there is the inner region which is the closest to the wall. In this region, only the wall units are relevant compared to the outer scales regarding the mean velocity. Furthermore, this region can be further subdivided into three layers, namely the viscous sublayer, the buffer layer and the log layer.

1. The viscous sublayer is located at $n_+ \lesssim 5$ and is dominated by viscosity causing a laminar flow and making the turbulent stresses negligible. Note that the velocity profile scales linearly as n_+.

2. The buffer layer is located at $5 \lesssim n_+ \lesssim 40$ and corresponds to a junction layer in which maximum production of turbulent kinetic energy is reached. Here, the viscous and the turbulent stresses scale with each other and none of them is negligible. The velocity profile is obtained by combining the two profiles of the neighbouring layers.

3. The log layer starts at $n_+ \gtrsim 40$ and reaches values of around $n_+ \lesssim 1000$ depending on the Reynolds number. It belongs at the same time to the inner and outer regions, thus constituting the main part of the overlapping region. In this intermediate layer, the properties of both the inner and outer regions come together such that neither the wall units nor the outer dimensions are truly relevant. The velocity profile is given by the universal logarithmic law $U_+ = \frac{1}{\kappa}\ln(n_+) + B$ with κ and B typically taking the values 0.41 and 5.1. In this layer the turbulent mixing is dominant.

Secondly, the outer layer, also known as the wake region or defect layer, constitutes the major part of the boundary layer making up around 80% of it. Furthermore, the viscosity effects become negligible while the outer scales gain a strong influence on the mean velocity outside of the log layer.

Finally, the overlap region mostly corresponds to the log layer that has been previously discussed. Being an intermediate region, it is less precisely defined and also spreads out towards the buffer layer of the inner region as well as towards the outer region. Nevertheless, its behaviour is mainly dictated by the buffer layer such that neither the inner scaling of the BL nor the outer scales play a relevant role with respect to the mean velocity.

3.3.1 Separation

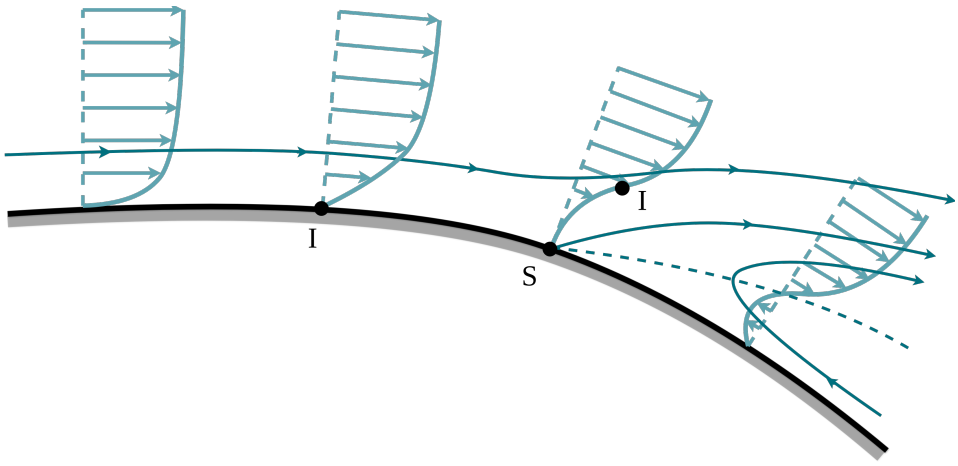

Figure 3.5: Streamlines and velocity profiles in the presence of a boundary layer separation, where S and I denote respectively the separation and inflection points. The dashed line corresponds to the locations where the tangential velocity with respect to the wall is zero. Reproduced from [33].

Following [33], the typical case of flow separation is encountered when dealing with diverging geometries inducing an adverse pressure gradient in the flow field. This general configuration is illustrated in Figure 3.5. In such a case, a deceleration of the flow happens due to the enlargement of the section. The boundary layer shape is directly impacted and the apparition of an inflexion point I can be observed in the velocity profile. The presence as well as the evolution of the inflection point is induced by a specifically low velocity close to the wall. At some point, the existing adverse pressure gradient becomes more important than the incoming flow stream thus provoking a reversed flow. The region in proximity to the wall in which the flow moves backwards is called the separation or recirculation region. Its most upstream position is given by the separation point S which corresponds to the location where the downwards and upwards moving flows meet. This flow feature relates to a zero tangential velocity close to the wall. At the same time, a flow normal to the wall pushes the fluid into the main flow by following a specific streamline which in turn characterizes the border of the separation region. Accordingly, the value of the stresses vanishes at this specific location such that

$$\tau_w = 0 \quad \textbf{(at separation)}. \tag{3.42}$$

At low Reynolds numbers, the separation region is usually well-defined and composed of a steady vortex recirculating the flow. When increasing the Reynolds number, this region becomes unsteady behaving in an intrinsically chaotic manner. The separation region provokes large drag values which are especially dominated by the form drag generated. In many applications, one wants to minimize drag such that streamlined bodies are preferred over bluff bodies in order to prevent separation as much as possible. While streamlined bodies allow the flow to pass smoothly around the body, bluff bodies typically have sharp edges and abrupt direction changes leading to separation even at low flow velocity. As mentioned previously, turbulent BL typically resist better to adverse pressure gradients and thus separation than laminar ones. The property is related to their energy content which is associated with much stronger convection rates. This feature translates by much fuller mean velocity profiles as shown in Figure 3.3. To resist or delay separation, the BL can thus be excited artificially to generate a fully turbulent BL. One example of a practical application of this approach is the golf ball which possesses small bumps on its surface to induce the transition of the flow to turbulence leading to a retarded separation. The later separation implies a reduced wake and thus a smaller drag. The pressure gradient of the flow being an important

parameter in terms of separation study, is traditionally quantified by the acceleration parameter defined as

$$K = \frac{\nu}{U^2}\frac{dU}{ds}, \tag{3.43}$$

where U denotes the local velocity outside of the BL and s refers to the curvilinear coordinate tangential to the surface. From its expression, it can be seen that the acceleration parameter directly depends on the velocity derivative. The sign of K is thus dictated by the local variation of velocity. Negative values of K are related to decelerating flows and by deduction representative of an adverse pressure gradient.

In some cases when separation happens but the flow geometry is favourable, the flow is able to reattach to the surface forming a closed separation bubble. Favorable conditions are typically related to a negative pressure gradient allowing the flow to reaccelerate and reattach to the surface. In the presence of large enough positive values of K, a synonym of important favourable pressure gradients, a turbulent flow can also experience relaminarization. Another main mechanism is related to the transition of the flow to a turbulent regime, the physics behind this phenomenon are explained in further detail in the following subsection. When dealing with a laminar BL that detaches from the surface, the flow may be able to become turbulent and reattach to the surface through an increased momentum exchange. At the reattachment point, both flow directions tangential to the surface meet. So, as for the separation point, zero velocity and stress are observed at that location. The shape of the formed separation bubble is typically similar to the half of an ellipse. The recirculation area forces the surrounding flow to deviate around it. Indeed, the flow passing close to the separation region will first experience an acceleration before facing a considerable adverse pressure gradient once being passed by the peak of the bubble. Due to the unstable shear flow at the interface between separation and free-stream, the passing flow is often subjected to strong momentum exchange leading to the onset of transition in the flow until reaching the turbulent regime. This description is in direct relation to the previously mentioned reattachment mechanism through the transition of the flow.

3.3.2 Transition

Transition describes the fundamental change in the flow regime when passing from a laminar to a turbulent flow. It is an unsteady phenomenon that is very complex and thus difficult to model and predict. In most cases, the transition of a clean laminar flow to a turbulent one is not wanted meaning that this flow mechanism is tried to be prevented. A laminar BL is usually preferable because turbulent boundary layers generate in theory higher skin friction due to stronger momentum exchange with the mean flow. In some specific applications such as flow configurations where separation plays an important role, transition becomes a favorable phenomenon. In those cases, turbulent boundary layers will resist better to adverse pressure gradients and thus to separation than laminar BL because of their increased momentum transfer leading to overall better performances. For both approaches, a clear understanding of the mechanisms that generate transition is required to either delay or trigger the transition phenomenon in practice. Transition depends on numerous parameters but the most important ones are generally the Reynolds number, the turbulence intensity of the free stream and the surface characteristics such as the roughness or existing imperfections. Under favourable conditions often encountered with a high Reynolds number, several mechanisms exist to provide a sufficient level of perturbation to the flow to trigger the transition to turbulence. The most fundamental mechanism is the natural transition. The process itself consists of 6 different steps which are schematized in Figure 3.6 for an idealized flat plate [53].

As can be seen in Figure 3.6, the initial laminar flow is steady (1). The flow then slowly evolves and enters the transition phase when reaching the first critical value of the Reynolds number $\mathrm{Re}_{\mathrm{ind}}$, called the indifference Reynolds number. Afterwards, instabilities appear and two-dimensional Tollmien-Schichtling waves are generated (2). These first perturbations provoke the creation of three-dimensional disturbances as waves and vortices (3). By travelling further downstream, the three-dimensional structures, mainly consisting of Λ-vortices, decay by enhancing the momentum exchange (4). This process gives birth to so-called turbulent spots (5). Finally, these spots of concentrated turbulence trigger the transition to a fully turbulent regime (6). A second critical Reynolds number $\mathrm{Re}_{\mathrm{crit}}$ is used to mark the location where the transition process is completed and the turbulent state is reached.

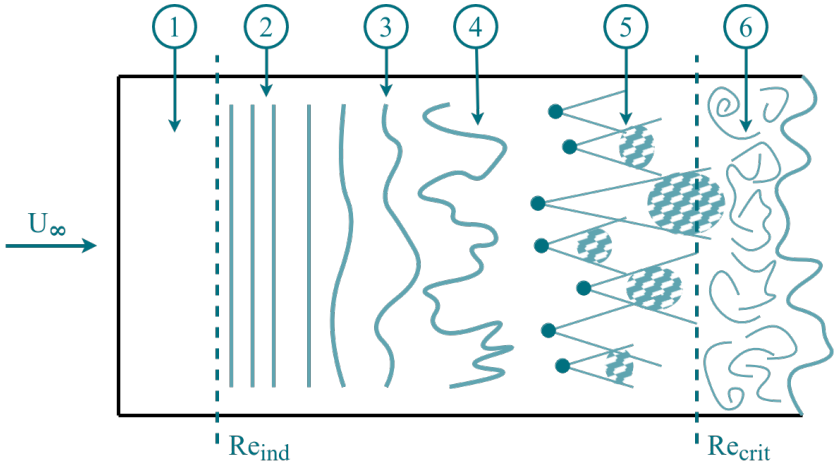

Figure 3.6: Schematic of the natural transition in the boundary layer of a flat plate. Reproduced from [53].

The process described in Figure 3.6 can also be modelled in a more rigorous and quantitative way. This is achieved by using the linear stability theory which assumes that a mean flow exists on which perturbation motions can be superimposed. The stability of these disturbances which are typically small compared to the main flow is then studied to evaluate their proneness to being amplified. The disturbances in the flow can either be described by simple partial perturbations or by complete modes. The latter types correspond to two-dimensional waves travelling in the streamwise direction. By using the notion of modes and considering the frequency domain, a perturbation differential equation known as the Orr-Sommerfeld equation can be established [53]. From there, the stability analysis of a laminar flow reduces to an eigenvalue problem that needs to be solved to determine the stability and thus the behaviour of the perturbations. The modes described by the Orr-Sommerfeld equation are the previously introduced Tollmien-Schlichting waves which can grow rapidly and induce a sufficient excitation level to the flow to trigger transition if the given modes are unstable. Non-linear factors exist that influence the transition of the flow but are not accounted for in the briefly presented linear stability approach. In reality, the initial amplitude or even the lifetime of a perturbation will generate non-linear effects that in turn will have an impact on the transition phenomenon.

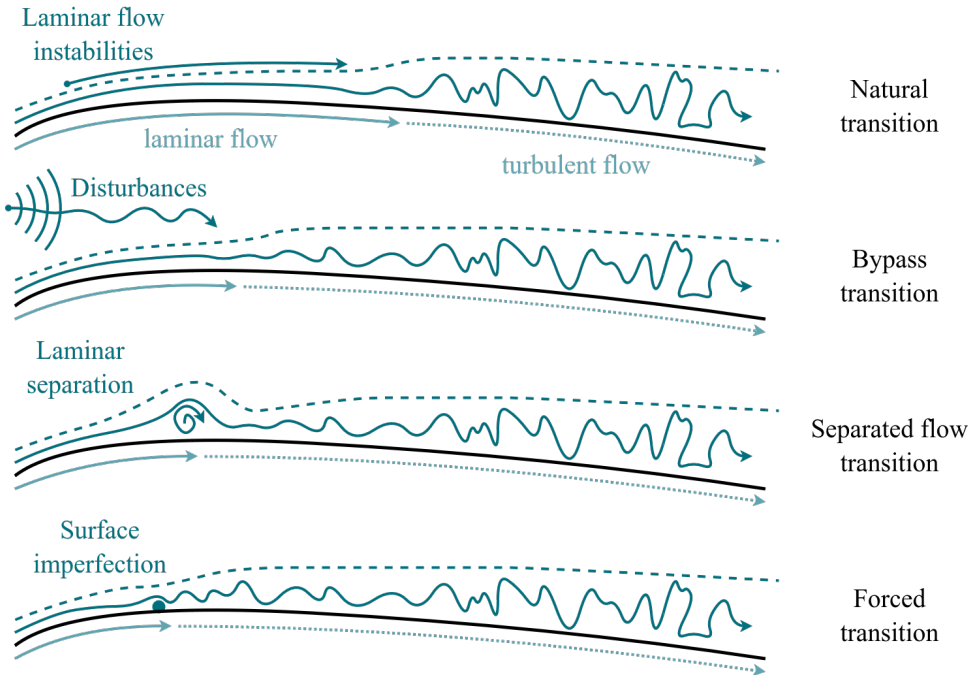

Figure 3.7: Illustration of the different transition mechanisms. Reproduced from [64].

In Figure 3.7 are illustrated in a simplified manner the four most common transition mechanisms. First of all, there is the natural transition which has already been discussed previously. It is typically the slowest process since it generates its turbulent content through small instabilities which develop in the flow. Secondly, the bypass transition consists of some sort of accelerated natural transition. With this mechanism, the first 3 of the 6 discussed steps related to Figure 3.6 are skipped. Thus, turbulent spots are directly created by interfering external flow features such as an increased turbulence intensity of the free stream or other unsteady flow phenomena. Thirdly, the separated flow transition is encountered when facing laminar separation. A free shear layer forms which is located at the interface between the main flow and the separation region since significant velocity differences exist among both regions. The presence of large velocity gradients will generate large shear stresses and will lead to important energy exchanges which will in turn provoke the transition to a turbulent flow. Finally, the forced transition is defined, as its name suggests, as a mechanism in which the transition is artificially accelerated. This premature transition to turbulence is either provoked by the presence of surface imperfections or achieved by specific devices that are mounted to the surface to excite the flow.

3.3.3 Shock interaction

Another phenomenon which needs to be introduced in the frame of this study is related to the potential interaction between shocks and boundary layers [52], [63]. Indeed, the present work will deal with transonic outlet Mach number, ranging from 0.7-0.95, such that sonic conditions can be reached due to local acceleration regions in the flow. This is especially true for the highest considered Mach numbers for which the compressibility effects will be the most visible. Since considerable acceleration is required to generate the shock, the suction side will be the most susceptible location where shocks will be formed. In Figure 3.8 is shown a typical interaction occurring between a laminar boundary layer over a flat plat and a shock. The main shock is accompanied by a downstream system of several weaker shocks generated by reflections and expansion fans. In fact, the main shock will have a fundamental impact on the thermodynamic flow state which will abruptly change from one side of the shock to the other. The downstream side of the shock is characterized by a considerable pressure increase which is provoking an important adverse pressure gradient. As discussed in subsection 3.3.1, adverse PG are favourable conditions for separation to occur. Since the boundary layer flow is moving at reduced velocities with respect to the main flow, the boundary layer itself is in a subsonic regime. This allows the information to travel upstream through the BL such that the strong adverse PG is felt more upstream than the shock location and the separation will occur at an according location. Note that the shock itself will block any information propagating upstream. In the present study, this feature will especially be observed by the acoustic perturbations generated by the wake which will be blocked at the level of the shock leaving the upstream region clean of these perturbations. As depicted in Figure 3.8, after the shock and the separation occurred, the flow is able to experience a significant pressure recovery leading to an acceleration of the flow and thus a potential reattachment of the separation region. The boundary layer then returns to its previous behaviour in the case in which the separation was not strong enough to sufficiently disturb the flow to initiate transition and thus a turbulent regime. In the free stream on the other side, the incoming shock is reflected by the BL. The flow deviation induced by the start of the separation bubble will provoke an auxiliary shock. Over the following region being characterized by the shape of the separation bubble, the flow experiences an isentropic acceleration leading to the presence of an expansion fan whose end is defined by a reattachment shock. A resultant reflected shock is then formed by the combination of the reattachment shock and the reflection of the main shock. Nevertheless, the precise flow field is very case-dependent such that various configurations can be encountered when dealing with compressibility effects as shocks. Further explanations and insights are given in [51], [52].

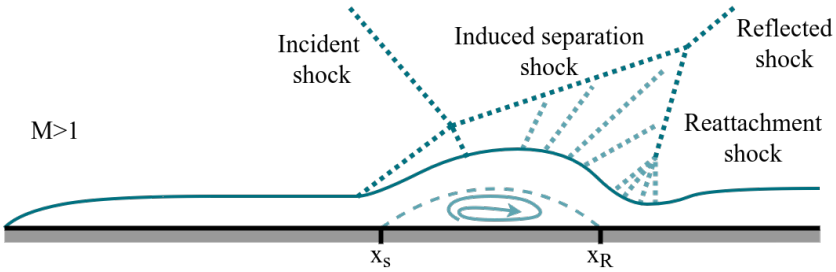

Figure 3.8: Illustration of the typical interaction between a shock and the boundary layer. Reproduced from [63].

3.4 Wake

The wake of a body corresponds to the downstream flow region which is strongly impacted by the momentum exchange between the object and the main flow. The phenomenon is illustrated in a simplified manner in Figure 3.9 for a rectangular-shaped body subjected to a uniform free stream. Since the considered body is not streamlined at its end, the flow separates at the upper and lower corners generating a highly turbulent wake region. The wake is delimited by two free shear layers which continuously spread out when moving downstream. The average velocity inside of the wake is initially close to the velocity of the body but then the velocity profile smoothly evolves and tends to the free stream velocity by exchanging momentum with the main flow. This process takes place due to the entrainment of the free stream by the slower wake. The phenomenon is additionally accelerated by the turbulent nature of the wake as well as the presence of large vortices provoking engulfment of the main flow inside of the wake thus leading to increased momentum exchange. Usually, the wake is composed of a highly chaotic flow, it is a region with a high energetic content and a significant presence of Reynolds stresses. These characteristics make it a very important region in terms of assessing the performance of a studied body. In many applications, this is done by evaluating the drag of the body which is directly linked to the wake. Indeed, in the present case, the wake of the turbine blade will especially condition the generated losses and thus have a considerable impact on the overall performance.

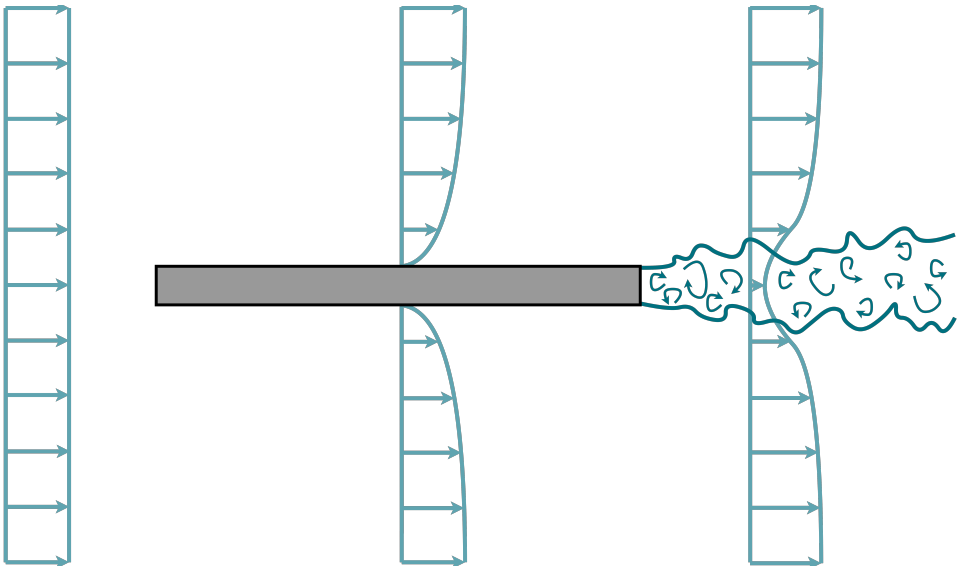

Figure 3.9: Schematic of the wake and mean velocity profiles generated by a bluff body, adapted from [16].

For an idealized planar wake as considered in [16], the width δ of the wake grows as $\sqrt{x}$, where x corresponds to the streamwise coordinate. Through momentum exchange, the velocity difference ΔU between the freestream and the extreme velocity faced inside of the wake behaves as $1/\delta$, or alternatively as $x^{-1/2}$. Note that the velocity distribution evolves in the streamwise direction by obeying a self-similarity law described by a mean velocity profile. The momentum deficit D generated by the body is conserved in this simple considered case and is given by the integral

$$D = \int_{-\infty}^{\infty} \rho U (U_\infty - U) dy. \tag{3.44}$$

3.4.1 von Karman vortex street

When considering the 2D flow around a cylinder, several flow configurations can be encountered (see [72]). At low Reynolds number ($\mathrm{Re} < 4$), a fully laminar flow surrounds the cylinder creating a symmetry between the upstream and downstream regions. This configuration corresponds to the Stokes flow. Small recirculation regions appear behind the cylinder when increasing the Reynolds number. The flow then passes by the cylinder and reattaches just after the separation bubbles. When the Reynolds number is further increased (typically $40 < \mathrm{Re} < 200$), the wake behind the cylinder becomes unstable. In this case, the cylinder successively releases vortices from its upper and lower side creating a periodic pattern in the downstream flow field. The oscillating

wake is thus composed of two staggered rows of counterrotating vortices. This phenomenon known as von Karman vortex street is illustrated in Figure 3.10.

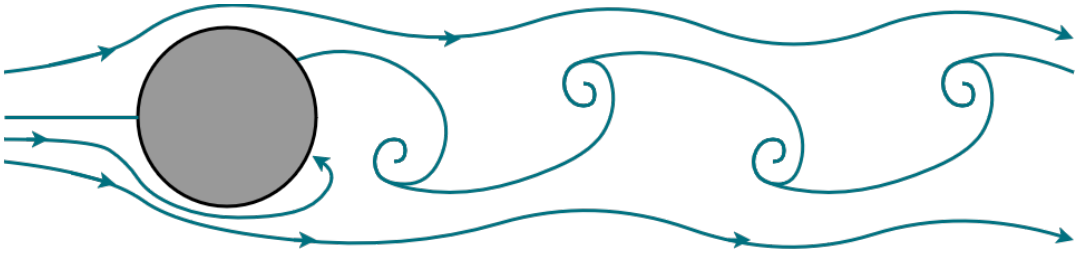

Figure 3.10: Schematic of the von Karman vortex street downstream of a circular cylinder for a typical Re range of 80-200, reproduced from [33].

The name von Karman vortex street is ascribed to Theodore von Karman who studied this flow feature. He formalized these specific flow physics as a superposition of irrotational vortices and studied the stability of the phenomenon. Thus, non-staggered rows of vortices are unstable while staggered rows satisfy the stability criterion only if their ratio of lateral over the longitudinal distance between vortices is equal to 0.28 [33]. The vortex structures released by the cylinder do not travel downstream at the freestream velocity U but at a significantly smaller convection velocity. The creation of released vortices can differ depending on the flow regime. For cases with $\mathrm{Re} < 80$, the vortex street is located further downstream and does not interfere with the attached recirculation regions behind the cylinder. When increasing the Reynolds number, the vortex street approaches the back of the cylinder thus affecting these flow bubbles. Indeed, the attached vortices start to fluctuate in an oscillatory manner leading to their successive and periodic break-off to feed the vortex street. The latter configuration corresponds to what is shown in Figure 3.10. When further increasing the Reynolds number, the wake behind the cylinder evolves into a fully turbulent wake. The characteristic size of the wake depends on the separation location of the flow on the cylinder which directly relates to the state of the boundary layer developing over the cylinder. Other configurations exist depending on the flow conditions for instance when taking into account compressibility effects.

The unsteadiness of the vortex street also affects the loading that the body is subjected to. Since the eddies are formed and released successively on each side of the cylinder, the applied lateral force oscillates accordingly. When the natural frequency of the body is close to the frequency f at which the vortex street fluctuates, resonance effects can generated. The provoked amplifications can potentially lead to important levels of structural vibrations and stresses. To quantify the frequency of the vortex street, the adimensional Strouhal number is used. It is defined as

$$\mathrm{St} = \frac{fL}{U}, \tag{3.45}$$

where L corresponds to the characteristic length scale and U to the characteristic velocity. Note that for circular cylinder shapes St typically takes values that are close to 0.21 [33]. This dimensionless frequency can also be related to the Reynolds number by means of the Roshko number (Ro). The expression for the Strouhal number then becomes

$$\mathrm{St} = \frac{\mathrm{Ro}}{\mathrm{Re}} = 0.212\left(1 - \frac{12.7}{\mathrm{Re}}\right), \tag{3.46}$$

where Ro is given by the empirical correlation for a cylinder established in [72]. Note that the previous explanations apply to the case of a simple cylinder. Since the trailing edge of the blade has a circular shape, its behaviour can be compared with the one of a cylinder. Similar phenomena are indeed observed in terms of the wake flow. Of course, the flow upstream of the TE will be fundamentally different for both cases and induce distinct flow behaviours. Nevertheless, the wakes will typically be of the same nature.

3.5 Flow passage physics

The turbine blades considered in this study are adapted versions of the T106C which are high-lift blades. This means that each blade will be subjected to important loads and thus pressure gradients. The combination of large pressure gradients (especially of adverse nature) and low Reynolds number encountered in LPT makes the flow

along the blade very prone to separation. Especially, the flow over the suction side will generate important losses when in the presence of large separation regions. The T106C blade is by design more loaded towards the rear, called aft-loaded. In comparison, the T108 blade is another existing geometry which is more front-loaded. The different designs as well as the resulting flow configurations were investigated in several studies as in [2], [54]. For the T106C, the separation typically occurs in the rear region of the SS such that its shape and induced pressure distribution can have a considerable impact on the load distribution. Nevertheless, the largest losses are generated when the separation region reaches the TE and interferes with the wake region leading to strong pressure defects. Different mechanisms exist to close the recirculation region before the TE, a synonym for reattaching the flow to the blade, thus considerably improving the performance. These separation behaviours will be investigated in a first approach by especially considering phenomena like transition. Afterwards, the blade loading in several configurations will be analysed. Different parameters will be investigated as the Reynolds number, the free-stream turbulence, the Mach number and even compressibility effects as shocks. Hereby, the focus will be laid especially on the suction side since it dictates the main performance of the turbine blade. The pressure side does not have a considerable impact on the overall losses. Nevertheless, the PS is characterized by a small separation bubble close to the LE which will be closed soon after by transition of the flow. Then the flow, which is again attached to the blade, is reaccelerated by a strong favorable pressure gradient. The losses linked to the flow over the PS are thus only local and not of significant magnitude since the flow will in all cases be attached to the blade over a large region until reaching the TE. Many studies were conducted during the past decades to investigate the different flow features encountered in the LPT. Note that the reference studies are mainly conducted at low Mach numbers between $M = 0.6$-0.7 whereas in this study transonic turbine flows will be considered. In fact, Mach numbers ranging from 0.7 up to 0.95 will be investigated in this work combined with a significant level of TI. No unsteady wake effects as passing wakes generated by upstream rotating bars will be studied in the frame of this work. The latter can have an important beneficial impact on the transition of the flow if the frequency of the incoming wakes is well tuned (see [2], [41], [65]). Finally, the Reynolds number ($\mathrm{Re} = 0.7 \times 10^5$ in this study) will be of the same magnitude but typically lower than the ones used in the main studies presented in the following. Note that the present section is considerably inspired from the literature review done in [4].

3.5.1 Separation and transition phenomena

Transition and separation are two flow mechanisms which are closely linked together and are both fundamental in the study of the flow in LPT. Through the transition, the flow will change its flow regime towards a turbulent state characterized by a chaotic flow field with important momentum transfer. Turbulent flows are usually combined with larger friction and losses generated but in some cases, their properties can become advantageous, especially in terms of mixing and stability of the flow. This leads us to the separation process which typically occurs in the presence of adverse pressure gradients provoking the flow to separate from the surface. Hereby a recirculation area is formed which in some cases can be closed either through relaminarization or through an increased momentum transfer in the flow linked to the transition to the turbulent regime. In the context of LPT, a convenient approach to investigate these phenomena is by considering the momentum thickness Reynolds number Re_θ and the acceleration parameter K. The former provides a quantification of the turbulent content of the flow while the latter, which has been introduced in Equation (3.43), describes the pressure gradient effects in proximity of the blade surface. Taking into account these parameters the different transition modes can be studied and classified. Indeed, Mayle analysed in detail the transition mechanisms encountered in LPT in [39]. An important conclusion of his considerations consists in the schematic shown in Figure 3.11 describing the most convenient transition mechanisms based on the variation of the flow parameters Re_θ and K. Hence, the transition of the BL from laminar to turbulent regime can take place following three different modes: the separated flow, the natural and the bypass transition. The three mechanisms are separated by two distinct criteria plotted in Figure 3.11. The stability criterion describes the limit over which transitional flow features happen to appear in the flow, typically of the nature of the 2-dimensional TS waves thus linked to the onset of natural transition. The separation criterion delimits a region with a strong adverse pressure gradient and high Re_θ which is dominated by the separated flow transition. This criterion follows the mathematical expression

$$\mathrm{Re}_\theta K = -0.082. \tag{3.47}$$

The turbulence intensity plays another important role as can be observed. For large TIs, the transition process is typically bypassed since the free-stream turbulence level is then high enough to deliver sufficient excitation to the flow in order to trigger the transition. The external disturbance for the bypass transition could also originate from other flow features such as shock waves. Acoustic waves on the other hand are often present to perturb the flow

and trigger the natural transition mode but are usually not energetic enough to bypass the process. The effect of TI becomes less important in terms of influence on transition when considering large adverse pressure gradients. In LPT, the suction side of the blade is characterized by a first region of the negative pressure gradient (PG) over which the flow is accelerated followed by a significant adverse PG. Hence, the transition on the first part can potentially occur through bypass transition if the perturbations (*e.g.* TI) are strong enough. Next to that, on the second part of the SS, the transition is more prone to occur naturally or even by separation depending on the flow characteristics. Since the effect of the TI is considerably reduced in this configuration, the bypass transition is less usual and does not represent the dominant transition mode. It is still possible to happen under certain conditions. On the PS, the inverse topology is observed. At the very beginning, the flow is subjected to a very large adverse PG leading typically to separation transition. Afterwards, a strong favorable PG is encountered leading to a strong acceleration of the flow provoking the reattachment and a potential relaminarization.

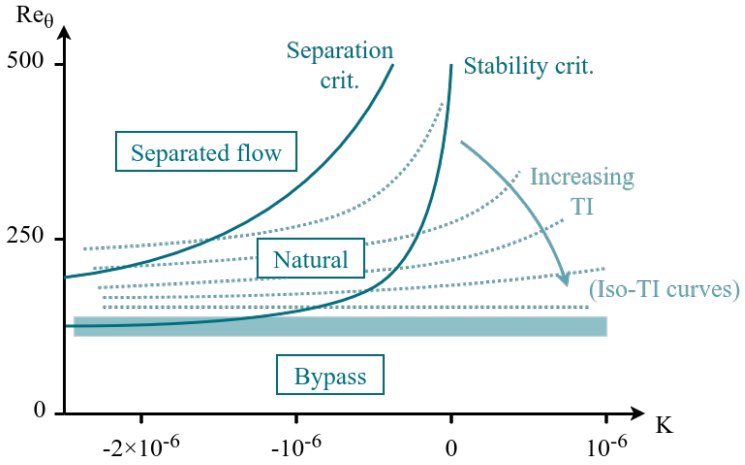

Figure 3.11: Main transition modes taking place in LPT for given variable sets of the momentum thickness Reynolds number Re_θ and the acceleration parameter K, reproduced from [39].

When studying separation different flow behaviours can be encountered. The separation region can be open such that no reattachment at surface level is taking place. Otherwise, the region is defined as closed taking the form of a bubble around which the free stream will be deviated. Indeed, several types of bubbles exist but typically two big families are encountered: the short and the long separation bubbles. Both types are associated with different properties and effects on the main flow. An important feature in LPT concerns the pressure distribution around the bubble. As discussed in [39], long bubbles will tend to provoke an increased pressure with significant implications in the overall pressure distribution while short bubbles will have a reduced impact characterized by the local deviation of the flow. As investigated in [27], [37], the nature and behaviour of the separation have a considerable impact on the performance of the LPT blades and can give rise to possible improvements through the understanding and control of these phenomena.

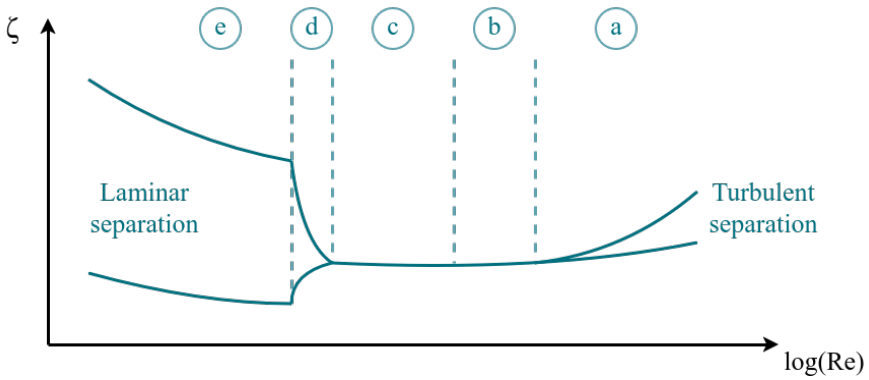

Figure 3.12: Behaviour of the loss coefficient ζ with respect to the Reynolds number under consideration of separation and transition phenomena, reproduced from [27].

A fundamental parameter in the study of separation is incorporated by the Reynolds number. Figure 3.12 shows the qualitative dependence which can be observed between the generated losses and the Re for the SS of the blade. For large values of Re (a), turbulent separation takes place near the TE with a transition initiating far upstream. In such cases, the losses are mostly characterized by the resulting mixing process as well as the shear layer contribution. When decreasing Re (b), the transition point moves downstream and the turbulent separation is successively suppressed. By following the previous trend, the transition location will at some point pass the laminar separation location (c). Thus, a laminar separation is occurring which is quickly reattached by creating a separation bubble. The overall losses associated with this configuration are limited since their only contributions consist of the wall hear layers losses and the wake of the trailing edge. For even smaller Re, the transition will happen further downstream such that the distance needed to reattach the flow increases provoking a separation bubble which is steadily becoming longer. The interaction between separation and transition is typically marked by the unstable laminar shear layer and more specifically the length over which it can resist before turbulence establishes. At some point transition moves so far that the length of transition is not sufficient and the bubble cannot be closed anymore, known as the bubble bursting. Since the flow is not able to reattach and the separation thus mixes with the wake, a drastic increase in losses can be noticed (d). The peak of this phase is reached when the onset of transition reaches the TE of the blade. The final range related to the smallest values of Re (e) is characterized by an important growth of the losses induced by the continual growth of the free shear layer thickness. Note that an additional curve is present in Figure 3.12 describing the minimal expected losses for the considered Reynolds number range. It is mainly based on idealized flow configurations such as perfect laminar flows over the complete SS which give rise to incredible performances. In real flows with the presence of perturbations and potentially considerable TI levels, such flows are not stable and are thus not representative of quantifying the expected blade performances.

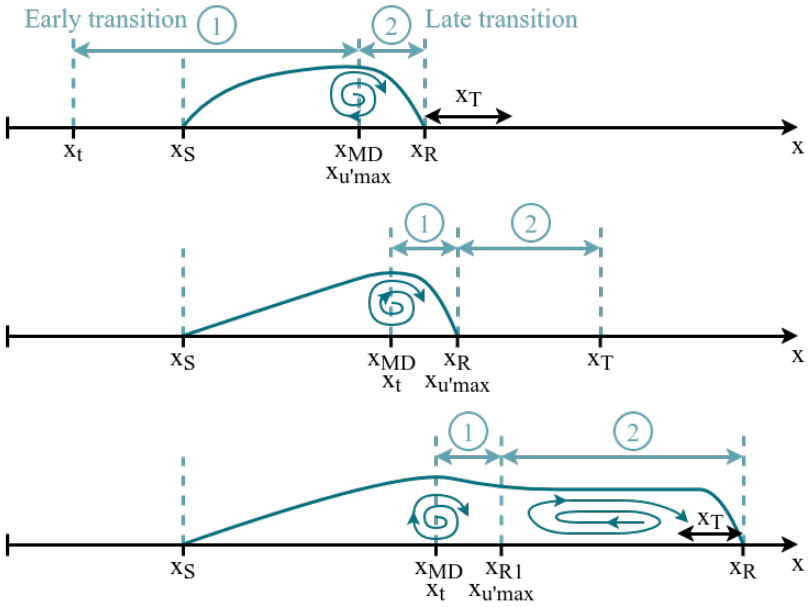

Figure 3.13: Illustration of the different separation bubbles encountered in LPT. The temporal average of the shape of the separation region is depicted for the transitional separation **(top)**, the laminar separation by short bubble mode **(centre)** and the laminar separation by long bubble mode **(bottom)**. Reproduced from [24] by inspiring from [4].

Further studies showed that overall 3 different types of separation bubbles are mainly encountered in LPT flows. Hatman and Wang [24] assessed their nature and overall behaviour. Illustrated in Figure 3.13, the three configurations correspond namely to the transitional separation, the laminar separation by short and by long bubble modes. In terms of nomenclature x_t denotes the onset of transition, x_T the end of transition and so the onset of turbulence, x_S the separation point, x_R the reattachment point, x_{MD} the point of maximum displacement and $x_{u'max}$ the mid-transition point (where velocity fluctuations are maximum). Note that the point of maximum deflection plays a key role in the characterization of the different modes and their flow effects. The top configuration of Figure 3.11 refers to the transitional separation bubble. It is typically linked to low Re values and small adverse

PG such that its physics are mostly characterized by the natural transition process engaged upstream of the bubble. The middle schematic describes the laminar separation mode with a short bubble. It can be related to low Reynolds numbers and moderate adverse PG. The transition starts after the separation location and is initiated by the inflexional instability at the point of maximum deflection of the shear layer. Lastly, for the laminar separation by large bubble, the separation region is strongly increased. Typically associated with low Re and large APG, the transition starts further downstream and is in addition restrained in its evolution. The flow achieves to reattach only after a considerable length provoking a large separation bubble. A first reattachment type behaviour can be seen at x_{R1} but due to the combination of low Re and strong APG, the mixing is not powerful enough to reattach the shear layer. Then in a second phase, the late transition zone is stretched out until finally closing the bubble. An interesting result of the study is that the Reynolds number evaluated at the separation gives rise to a better description of the phenomena than the traditionally used momentum Reynolds number Re_θ. Additionally, a precise strategy was elaborated to predict the separated flow transition based on a set of several criteria.

3.5.2 Blade loading

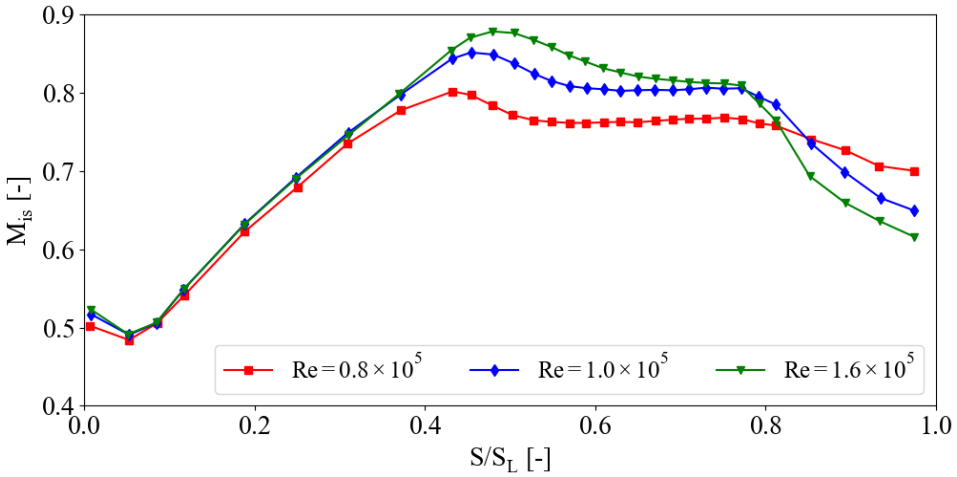

Figure 3.14: Isentropic Mach number distribution along the suction side of the T106C for different Re values, $M = 0.65$ and a free stream TI of 0.8%. Reproduced from [40].

The blade loading can be investigated with the distribution of the isentropic Mach number introduced in Equation (3.7). As mentioned previously, the T106C blade is characterized by a loading that is shifted towards the rear part of the blade. In Figure 3.14 are shown three distributions of the blade loading over the SS of the blade presented by Michalek in [40]. With a Mach number of 0.65 and low turbulence levels, the effect of a varying Reynolds number is investigated. The turbulence level considered is approximately $Tu = 0.8\%$. This corresponds to the background turbulence of the wind tunnel and thus represents the lower limit which is possible to achieve in experiments in terms of TI. Note that several other works considered the phenomenon as well by studying the flow around LPT blades (see [2], [14], [20], [54]). In the first part of the M_{is} distribution one can observe very similar behaviours among the three cases. Indeed, the flow is considerably accelerated over the SS corresponding to a laminar BL flow. When considering the loading after the peak, distinct behaviours can be seen. The presence of a strong adverse PG provokes the laminar separation of the flow from the blade. Only the high Re configuration achieves to close the bubble and reattach to the blade before the TE by transition of the flow to turbulence. It can be observed from the M_{is} curves that the intermediate case is also quite developed in terms of the transition of the flow. However, the turbulence is not developed enough and the flow remains detached in this case even though the trend is similar to the high Re case. Note that the transition typically takes place through the separation and the associated shear layer interactions but can also be dictated by an early initiated natural transition (characterized by TS waves) encountered especially for high Re configurations. The presence of the separation bubble impacts the distribution of loading due to its direct influence on the pressure distribution as has been discussed previously. As can be deduced from Figure 3.14, the considered Reynolds number has a direct impact on the transition effect and thus the reattachment procedure of the separation region. Higher Re are thus linked to smaller bubbles and prevent the bursting of the bubble which is associated with important losses.

The turbulent flow developing over the back part of the SS is in general linked to lower efficiencies and higher friction compared to the laminar flow. By transitioning to a turbulent regime, the flow is capable of closing the separation bubble. A significant impact on the total losses can then be observed since very high losses are typically generated when interactions between the separation region and the wake occur. These phenomena are prevented by the reattachment of the flow. The marginal losses due to the presence of turbulence are more than acceptable in this context. Since the transition happens towards the rear end of the SS, hence a limited area of the blade, this detrimental phenomenon is additionally reduced in importance.

Another important role is played by the free-stream turbulence level. Indeed, turbulent fluctuations present in the flow field can lead to a sufficient amount of perturbation to provoke a bypass transition. This is the case only in specific conditions as will be seen in the following. In Figure 3.15 are shown three different cases taken from [2], [43] to illustrate this phenomenon. For the case studied by Pacciani et al. [43] with a relatively low Re (80×10^5) significant differences can be observed. While the configuration without turbulence grid ($Tu = 0.8\%$) is associated with an open separation region until the TE of the blade, the two cases with high TI achieve to engage transition and close the bubble before the TE. In bypass transition, the classic procedure of natural transition with TS waves is accelerated and turbulent spots are directly generated by external perturbations, as the free stream turbulence in the present case. Both configurations with turbulence grid ($Tu = 1.8\%$ & 2.6%) follow nearly the same behaviour. It can be deduced that the exact level of TI is not the most significant parameter as long as it is above a certain minimum value. This behaviour observed for an increasing TI is well studied in literature such that the evolution of the effects on the separation and BL is limited when surpassing a given TI threshold (see [40]). For the higher Reynolds numbers investigated by Benyahia et al. in [2] the influence of the TI seems to be less important. Indeed, one can observe for $\mathrm{Re} = 1.0 \times 10^5$ that transition establishes faster and the separation bubble is closed sooner with a higher turbulence level. This observation is also noticeable for the high Re case but the impact of the TI is becoming less significant with increasing Reynolds number. Note that the TI does not influence the BL evolution over the first part of the suction side. Due to the strong acceleration and the reduced BL thickness, the turbulent structures are not able to interfere directly with the BL. By continually increasing the BL momentum thickness, particularly when encountering separation, the effect of the turbulence intensity on the BL becomes significant. Note that several other works assessed the phenomenon of steady free-stream turbulence interacting with the LPT blade (see [15], [17], [21], [40]).

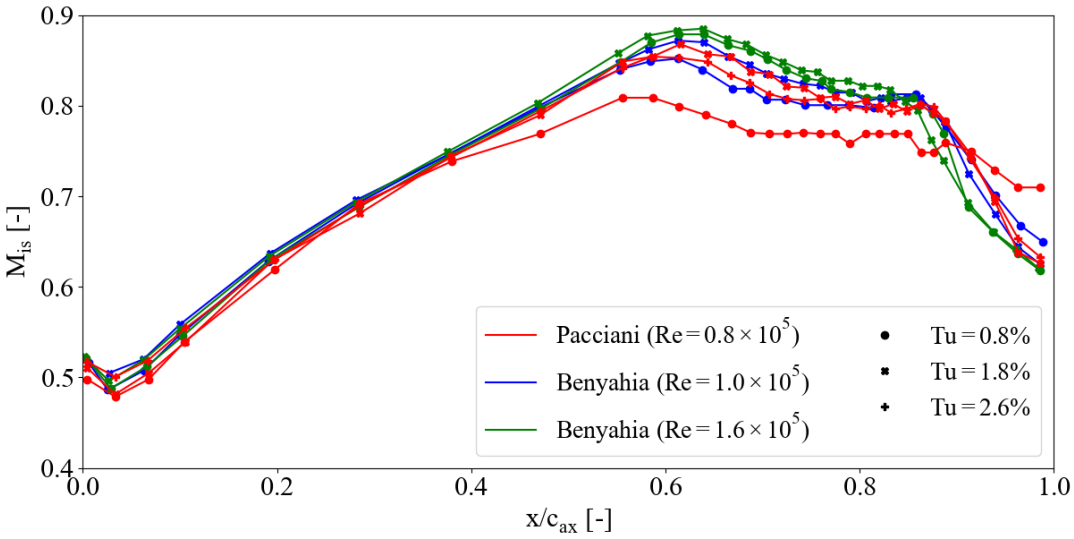

Figure 3.15: Isentropic Mach number distribution along the suction side with different combinations of Re and M for a varying free stream TI. Benyahia et al. [2] studied two cases at $\mathrm{Re} = 1.0 \times 10^5$ and 1.6×10^5 with varying TI at $M = 0.65$. Pacciani et al. [43] considered a similar setup with a Reynolds number of 0.8×10^5, $M = 0.65$ and for 3 different TI levels. Note that all measurements correspond to the T106C blades.

3.5.3 Boundary layer characteristics

Further understanding can be obtained by studying the flow behaviour of the boundary layer along the suction side. In this context, Dähnert et al. [8] conducted experiments for a range of low Reynolds numbers combined with a low level of free-stream turbulence of 0.5%. In Figure 3.16 are shown some of the obtained results consisting of integral BL quantities as well as surface variables such as friction. The shape factor H for two typical Reynolds numbers is presented in Figure 3.16b. It is characterized by initial laminar values before considerably growing and reaching a maximum which corresponds to the start of transition. The latter is mainly induced by Kelvin-Helmholtz instabilities acting at the shear layer level of the laminar separation region. It is followed by a decrease of H which is provoked by a simultaneous increase of the momentum thickness and decrease of the displacement thickness. This behaviour is directly related to the transition of the flow. One can notice that the onset of transition happens earlier for the higher Reynolds number which is well in line with the previous discussions. In Figure 3.16b are also plotted the evolution of the momentum thickness Reynolds number for both cases which experience a significant increase in the region of transition before stabilizing. By analysing the intermittency typically characterizing the turbulent nature of the flow, Dähnert assessed the transition to turbulence of the flow which he found to be fully developed before reaching the end of the SS. Note that even though turbulence developed, the flow has not been able to reattach to the surface for the low Reynolds number. Moreover, the skin friction coefficient was measured, as is shown in Figure 3.16a. The graph using Re_θ as abscissa is accompanied by two correlations for laminar and turbulent flow regimes. For small momentum thickness Reynolds numbers, the measured quantities match quite well the laminar correlations. Afterwards, a strong difference is observable most probably because the correlation is only valid in the presence of a zero PG which is clearly not the case, especially for the high Re_θ values. The flow being detached for the low Re case, the skin friction values remain accordingly small. For $\mathrm{Re} = 1.6 \times 10^5$, the development of the flow towards a turbulent regime is observable at the blade level since the flow reattaches. Indeed, Figure 3.16a shows that after the c_f values corresponding to the separation bubble, the skin friction increases for the highest Re_θ and matches the turbulent correlation.

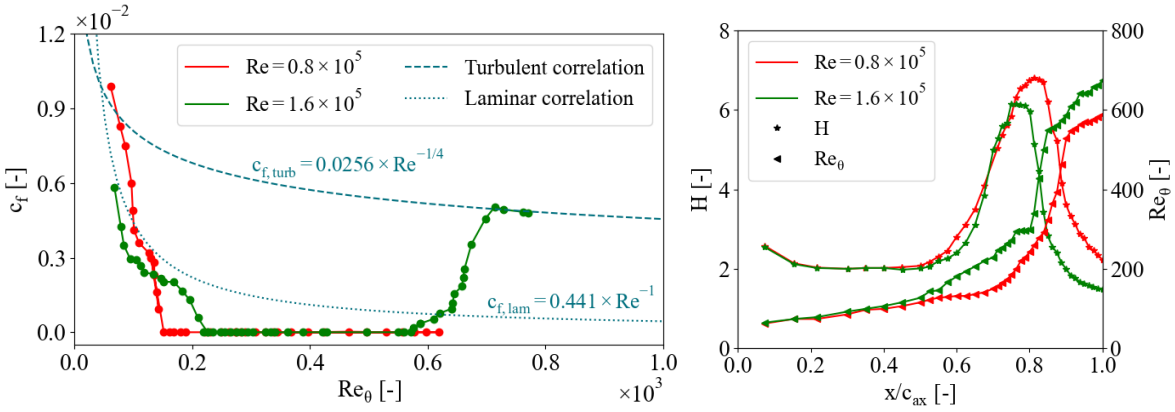

(a) Distribution of the skin friction coefficient with respect to the momentum Reynolds number with corresponding laminar and turbulent correlations as reference (see [8]).

(b) Spatial distribution of the shape factor H and the momentum Reynolds number Re_θ over the SS of the T106C.

Figure 3.16: Boundary layer quantities measured on the suction side of the T106C for two distinct Reynolds numbers (0.8×10^5 & 1.6×10^5) and a TI of 0.5%. Reproduced from [8].

Concerning the compressibility effects encountered when considering transonic flows, Börner and Niehuis investigated these features in [5] for the T108 blade geometry. With a transonic flow set at $M = 0.95$ and a high steady turbulence level (7.7%), they observed the interaction between the shock formed on the SS and the BL. A considerable impact of the shock on the BL transition phenomenon was noticed provoking an acceleration of the transition through the induced perturbations. This interaction between the shock and boundary layer has already been introduced and investigated in more detail previously (see subsection 3.3.3). More profound studies of these interaction phenomena were conducted by Sandham in [52] and Sabnis in [51]. Another study regarding compressibility was conducted by Vazquez et al. in [65]. By varying the Mach number different flow features as well as the global performances were analysed. The blade loading was highlighted as the dominant factor conditioning the generated losses. Overall, the efficiency of the blade can be increased through compressible effects when considering higher Mach numbers combined with adequate parameters. The improvements are typically

due to an increased velocity ratio and lower stage loading but the results obtained are strongly dependent on the shaft speed.

3.6 Review of existing turbulence injection methods

Several strategies exist in order to generate inflow turbulence. Wu [69] introduced them in two main types of flow generation: recycling and synthetic methods. This vision can be further completed and developed, such that one can typically distinguish between four different families of methods as discussed in [23]: transition-inducing, recycling-rescaling, library-based and synthetic methods. In recent years, a new fifth category emerged which is based on Machine Learning and Deep Learning techniques. Hence, the various categories are based on fundamentally different approaches. Some are designed or interesting for specific types of applications while others are usable in a wide range of cases. Those different methods will be presented and detailed in the following.

3.6.1 Transition-inducing methods

This first method is based on the state of the boundary layer and more specifically on the transition phenomenon discussed in subsection 3.3.2. Thus, various approaches exist to trigger the transition of a developing laminar BL. The main idea of the present method relates to the concept of deliberately introducing perturbations in the flow field in order to initiate the transition process to the turbulent regime [23]. Hence, no turbulent structures are directly created or injected. In practice, those methods typically need large development lengths for these perturbations to grow and influence the flow field to transit to a fully developed turbulent regime. Furthermore, they are not very versatile and their range of applications is quite restrictive to specific applications, such as boundary layer simulations. Although this method is very straightforward to implement and use, its restricting characteristics in terms of application possibilities are usually prevailing.

3.6.2 Recycling–rescaling methods

In this approach, the idea of recycling is exploited. The flow which is steadily evolving towards a developed turbulent configuration, is extracted at a downstream position, rescaled and then reinjected at an upstream location. By applying this recycling process continuously, the flow field converges to an asymptotic configuration in which the flow features are fully developed. Hence, direct feedback from the actual domain is taken into account by this method representing one of its main advantages [69]. The recycling and rescaling process needs to be well-designed to generate a physical flow. Furthermore, spurious low-frequency signals can generate important issues due to the finite distance between extraction and injection positions. The fact of targeting a fully developed mean flow in the streamwise direction is a quite restrictive characteristic in terms of application possibilities. The latter are often simple and idealized test cases as channel or pipe flows. The rescaling operation is required especially in the presence of a spatially developing BL in order to adapt the flow from the extraction to the inlet section since the mean flow is evolving streamwise. Thus the main purpose of rescaling is to satisfy the statistics related to the mean flow and the Reynolds stresses. This category of methods is also known as the weak recycling method, while the strong recycling corresponds to the case in which a strict periodic condition is applied and though no rescaling is performed on the extracted data. An important feature is that a strong spatial correlation or periodicity is present in the flow field linked to the distance between the extraction and injection section.

The first real applications of this method were made by Wu et al. [68]. There a zero pressure gradient boundary layer over a smooth flat plate was investigated and a weak recycling method was used to generate the inflow turbulence. The latter was obtained by rescaling the BL from a downstream location knowing the temporal statistics and assuming that the inner region depends on the wall unit y^+ while the outer region relates to y/δ. Later, Lund et al. [38] further developed this approach by formalizing it leading to the LWS method. However, in this approach, a transition region is typically present following the inlet injection plane. Additionally, the method is restricted to simple flow configurations that are based on the assumption of the presence of an equilibrium BL. Xu and Martin [71] further improved the method by proposing a version for compressible flows in which the temperature was linked to the velocity based on Morkovin's hypothesis.

3.6.3 Turbulence library-based methods

Following [23], this method generates a turbulent flow by extracting realistic inflow data from a database of snapshots or an auxiliary simulation. This approach can be seen as part of the strong recycling methods mentioned previously thus regrouping as well the so-called precursor and co-simulations in this category. So either an existing database compliant with the test case is used or an auxiliary simulation needs to be run in order to generate a turbulence field which can be injected afterwards. By performing a complete simulation, the inlet data is generally of high quality and fewer approximations are made like Taylor's frozen turbulence hypothesis. Since the injected data is already describing a physical solution, the transition length in the domain is very short compared to the other approaches. The parameters for this precursor simulation characterized by a simple domain with periodic BC, can be adjusted precisely in order to tune the characteristics of the flow field as the turbulence intensity or the the length scales. The significant drawback lies in the computational cost linked to this additional computation. The higher the Reynolds number of the turbulent flow, the higher the cost of this auxiliary high-fidelity simulation. An additional issue with the precursor methods is related to the injection process during which the flow field is extracted from the precursor output files and then acting as input files for the main simulation. Those files that can have a considerable size need to be stored, read and processed in an effective way to not impact the performance of the whole simulation. When using co-simulation of the auxiliary domain, the storing and reading of the input files is not necessary. On the other hand, the overall cost and complexity of the main simulation are impacted by this approach since the main as well as the auxiliary domains are solved simultaneously. For complex geometries, where mostly no databases exist, the definition of a precursor simulation with adequate periodic BC may be very challenging.

Lee et al. [36] employed this method to generate the turbulent flow approaching a standing normal shock wave. The former was obtained through a precursor simulation of a time-dependent, unforced compressible HIT. Over the following years, this approach has been widely used and applied to different test cases while continuously being developed and improved.

The turbulence injection method implemented in ArgoDG which is used in this work belongs to this category. It uses a precursor simulation to generate the turbulent flow field in a triply periodic box. This turbulence field will be frozen at a target instant and then superimposed to the inlet bulk velocity corresponding to the inlet boundary condition of the main domain. Further details related to the used approach are given in the following section, see section 6.1.

3.6.4 Methods enhanced by machine learning and deep learning techniques

In recent years, the use of machine learning has emerged in the field of turbulence. Those ML techniques are based on neural networks that are trained on a huge database of simulation and experiment results. Starting from the available data, a model is built by optimisation which allows to make predictions of new artificial flow fields. Another approach consists of the creation of a generative technique which will model the overall distribution of information contained in the available data in order to generate coherent images and flow fields. Thus, an interesting application is to take advantage of these possibilities for the generation of inflow turbulence that will be injected into a domain. One should not forget that for most models the generated turbulence is created through the aggregation of synthetic fluctuations deduced from the available database, yielding not a physical flow but one that resembles a real flow. Implementations of this newer approach were made by Fukami et al. [19] for the inflow turbulence generation in the case of a turbulent channel flow. Therefore, a convolutional NN was trained on an extensive database with flow fields obtained from previous turbulent channel flow simulations. Kim and Lee [31] worked on the same problem set and successfully generated turbulent inflows for different Reynolds numbers. To achieve this, they used a generative adversarial network combined with a recurrent NN in order to further improve the performances and obtain higher-quality results which are less sensitive to the input quality.

3.6.5 Synthetic methods

Finally, the synthetic methods as described by Hao in [23] are a widespread approach based on the production of turbulent inflow data through randomly generated sequences. This means that the flow field is obtained by using analytical expressions or statistical techniques [11]. Thus, the synthetic methods will either generate a complete turbulent flow field or accelerate the onset of turbulence at the inlet section. The very flexible characteristics of the approach give the user a lot of freedom in the parametrization and design of the inflow data

which is especially interesting when facing complex geometries. Compared to the library-based methods, not only the computational cost related to a precursor simulation is avoided but also the memory required to store all the gathered data. However, the scope of this approach is much more fundamental than just generating white noise perturbations superimposed on a mean flow. The challenge consists of approaching the closest as possible to physical turbulence. Therefore, the flow and especially the structures need to be spatially and temporally coherent. The fluctuations generated in this purely artificial way are never fully compliant with real turbulent flows [28]. This feature causes the existence of an adaption length, called development fetch, just after the injection location in which the artificial flow morphs into a physical flow field governed by the NSE. The development fetch is usually a good indicator of the quality of the synthetic method because the more realistic the generated flow field is, the shorter the required development length will be. The ideal synthetic method should thus need no development fetch. Furthermore, this entry length needs to be considered in the domain of the main simulation, hence leading to a higher computational cost. In synthetic methods, the stochastic inflow data is generated from some uncorrelated data combined with known properties and statistics. The quantities available are typically the integral length scale, the turbulence intensity, the Reynolds stress tensor, the energy spectra or others. Thus, the generated synthetic turbulence fields can basically be seen as random realizations of an equivalent physical flow. In order to achieve a higher level of statistical description, one can also consider the correlation function R_{ij} which contains additional information compared to the previously mentioned quantities. Synthetic methods usually achieve to match first-order statistics directly but higher-order statistics are often satisfied after passing the development fetch. Furthermore, for the generated fluctuations to endure and not be dissipated rapidly, the spectral contents of the artificial inflow should be similar to those of actual turbulent flow fields [29].

An important issue is that the flow information and statistics required to make proper modelling of the fluctuations are often not available or are difficult to obtain especially in complex configurations. Furthermore, the artificial generation of turbulence can have a more profound impact on the actual mean flow and the phenomena taking place. This is especially true for highly non-linear systems as is the case for the NSE where small perturbations and approximations can lead to considerable changes in the surrounding flow field and the obtained results.

Several methods have been developed in the past which are mainly differentiating in the way spatial and temporal coherence is enforced on the inflow. The most popular methods are very briefly presented in the following [23]. The proper orthogonal decomposition (POD) approach allows the formal mathematical description of spatially and temporally coherent structures with the smallest number of modes for a given accuracy. The digital filter approach is based on explicit filtering. The velocity fluctuations are generated by imposing spatial and temporal correlations on a random field before being superimposed on a mean flow. Spectral-representation-based approaches exploit the fundamental properties of Fourier transforms to impose spanwise and temporal correlations. Additionally, the use of a spectral representation facilitates the generation of a realistic energy spectrum. Other synthetic turbulence injection approaches are the synthetic eddy method, the cell perturbation method, the volumetric-forcing-based approach or the scaling approach.

4 Numerical tools

This chapter will introduce the numerical framework necessary to realize the computations done in this work. The task of doing a Direct numerical simulation (DNS) may seem quite straightforward in the first approach since the Navier-Stokes equations (NSE) are solved directly while the amount of models used is minimal. On the other hand, the complexity from a computational point of view and the resources required are considerable. These factors present one of the main challenges in such applications. As illustrated by Figure 4.1, the modelling required is larger for LES and even more for RANS approaches than for DNS. However, the achieved accuracy, as well as the computational cost, are accordingly higher the less modelling is performed. Typically, the DNS of fluid dynamic problems has a complexity that increases with the Reynolds number. The computational resources necessary for a DNS are of the order of Re_c^3 to $Re_c^{3.5}$ [26]. Meanwhile, over the past decades, the computational power available has increased steadily and allowed the scientific community to tackle more and more complex simulations. In order to handle so large problems it is needed to subdivide them into smaller problems which can be solved separately. This leads us to the parallelization and its importance in terms of computational performance. In fluid simulations, the computational domain is divided into several partitions and each part is solved parallelly by one or several computational cores, known as CPUs. Therefore, different parallelization protocols are used such as MPI and OpenMP. The highly parallel computational resources which are required to perform these tasks are provided by supercomputer clusters. To exploit these resources in the most optimal way an adequate solver is necessary. For this study, the high-order fluid solver ArgoDG which implements the discontinuous Galerkin method (DGM) is used. Due to the discontinuous framework, the DGM employed by the solver facilitates the aforementioned parallelization of the computational problem. These different fundamental elements which are necessary for solving a high-fidelity DNS will be presented in more detail in the following.

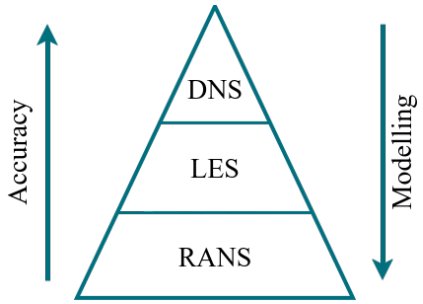

Figure 4.1: Illustration of the fundamental properties of different methods for computational fluid dynamics simulations.

4.1 HPC and Lucia

In Belgium, the *Consortium des Equipements de Calcul Intensif* (CECI) manages the supercomputing resources which are constituted by 6 clusters [6]. Among these 6 high-performance computing centres, five are hosted and maintained by different Belgian universities while the last one, called Lucia, is managed by *Cenaero*. Those supercomputers are funded by the *Fond national de la recherche scientifique*, short FNRS, and have scientific research as purpose. Thus, university members, researchers of the Fédération Wallonie-Bruxelles and research

centres, but also companies having specific agreements with the Walloon region can have access to and benefit from these clusters.

In this work, the tier-1 supercomputer managed by *Cenaero*, named Lucia, will be used [12]. Figure 4.2 shows some cluster rakes and connectivity. In terms of performance, Lucia can reach about 4 PetaFLOPS when combining its CPU and GPU partitions. Overall, it was ranked 245th on the November 2022 Top500 list with its GPU partition. Lucia, which has its name after the Belgian chemist and professor Lucia De Brouckère, was introduced

Figure 4.2: Pictures of the supercomputer Lucia, taken from [6].

in 2023 by replacing the previous tier-1 supercomputer Zenobe. Lucia can be divided into different partitions but the 2 main ones correspond to the CPU and GPU compute nodes. Regarding the CPUs, overall 300 nodes of HPE XL225n model make up this partition while each node is composed of 128 CPU cores. The processors used are *Milan*-type AMD EPYC 7763 64-core working at a standard frequency of 2.45 GHz. Furthermore, each node has 256 GB of RAM associated with it and from this memory, 240 GB are available for the user. The GPU partition on the other hand gathers 50 GPU nodes of HPE XL645d model composed of 32 cores each driven by a *Milan*-type AMD EPYC 7513 32-core processor. The latter operates at a processor frequency of 2.6 GHz while the node again has a memory of 256 GB. Another major difference to the CPU nodes is that each node possesses four Nvidia A100 40GB accelerators. Note that next to these standard CPU and GPU nodes, other more specific nodes exist with other properties, typically having larger memory capacities or designed for other specific tasks such as visualization. Concerning the storage, the system is based on the Spectrum Scale filesystem (previously GPFS) developed by IBM and its standard disk tier contains an overall size of 2.87 PB. This standard disk tier is further composed of home (200TB), projects (1.5PB) and scratch (1PB) spaces and a backup system is implemented for the home and projects filesets based on IBM Spectrum Protect. Furthermore, all the different partitions of Lucia are connected through an HDR Infiniband network and a 10 Gb/s Ethernet network [12].

Furthermore, the scheduling of jobs on Lucia is managed by a Slurm Workload Manager. In order to queue and run the jobs, one needs to submit an adequate Slurm file containing the job characteristics. The latter correspond to the job duration, the number of requested nodes and CPUs, the modules used, the memory requirements as well as the different directories and files needed. The scheduling itself is based on a fairshare concept using priorities computed based on different factors to distribute in the most equitable and optimal way the accessible resources among the many users present.

During this study, mainly the standard CPU nodes were used to perform the simulations while specific visualization nodes were used for postprocessing tasks. For each simulation, 16 nodes were allocated which corresponds

to 2048 CPU cores and around 3840 GB of memory. Note that limitations are present and possibly authorizations are required regarding the usage of the nodes on Lucia depending on their category. For instance, for the standard CPU nodes, a maximum number of 128 nodes can be requested for a single job while a job cannot last longer than 48 hours nor more than 2000 jobs can be run simultaneously.

4.2 Discontinuous Galerkin method

Several numerical methods exist to discretize and approximate the NSE in the framework of a DNS. In fluid simulations, the most widespread method is the Finite volume method (FVM). In a very simplified view, the latter method is characterised by simple elements that take single values as solutions valid over the whole element. Those quantities being constant over each element are computed based on the flux balance evaluated at the boundaries of the element. Thus, the solution in the domain for the FVM is by definition discontinuous between the elements. Next to that, the Finite element method (FEM) uses piecewise polynomial functions to describe the solution in each element. The main idea then is to enforce the matching of the solutions at the element boundaries leading to a continuous solution over the whole domain. The DGM which is implemented in ArgoDG can be seen as a combination of the previous methods in a very simplified way. The DGM is an unstructured high-order accurate method [7]. The solution in each element is represented by a polynomial or any desired continuous shape function. This property enables to have a high order of accuracy at the element level. Additionally, the continuity requirements at the boundaries between elements are relaxed and complemented by the manipulation of fluxes allowing the method to better handle discontinuities as boundary conditions or even shocks in theory (see [13], [25]). These characteristics give the DGM improved stability and accuracy properties compared to the other methods. On the one hand, the FVM is well suited for convection-dominated problems, *i.e.* hyperbolic problems, mainly thanks to the manipulation of fluxes. It has more difficulties handling incompressible flows and lacks accuracy when diffusion effects become important in convection-diffusion problems. On the other hand, FEM has issues handling discontinuities like shocks and is usually unstable when facing convection problems, thus needing a stabilization method in order to work properly. In the meantime, the DGM is constructed by design in such a way that it can handle a larger range of possible cases without adaptations needed. Note that regarding diffusion effects since DGM is based on the evaluation of the fluxes as in the FVM, methods are needed to stabilize the fluxes. Therefore several approaches exist and the one used in this case is the symmetric interior penalty discontinuous Galerkin (SIPDG) which evaluates the discontinuities at the element boundaries and awards penalties to them. Solutions are then obtained by taking into account and iteratively minimizing this penalty, thus corresponding to the most fitted solution in order to avoid too-large discontinuities between elements.

Figure 4.3 describing a general trial space of the DGM provides a qualitative illustration of the basic concepts implemented in the DGM. Thus, the solutions ϕ_{e_i} in neighbouring elements e_i are not necessarily required to match with each other.

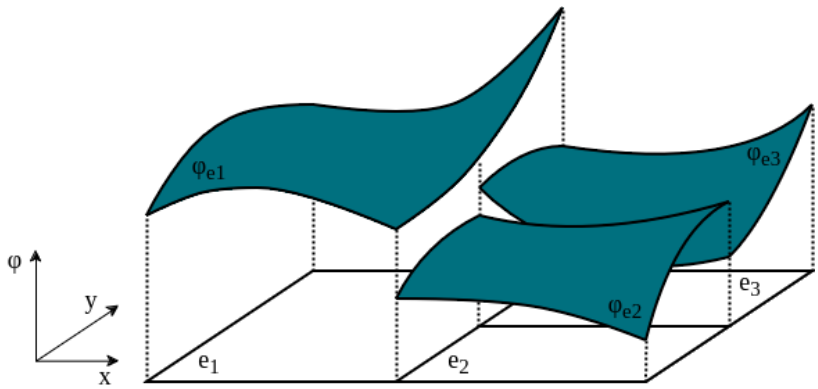

Figure 4.3: Example of the discontinuous trial space related to the DGM, reproduced from [25].

4.3 ArgoDG

The solver ArgoDG, developed at *Cenaero*, implements the DGM. It is a 3-dimensional compressible flow solver which has high scalability capabilities, thus well suited for the HPC context. Over the years it has been used in several programs leading to a steadily filling portfolio of test cases proving the fidelity of the solver but also contributing to its public visibility. Some examples of previous projects are the European programs ADIGMA, IDIHOM, Tilda and HiFiTurb.

The usage of the solver is done in a quite straightforward way, such that a main input file exists in which all parameters of the simulation are specified. In the different sections of this file, a wide range of parameters related to the case and the geometry are set like the mesh, the boundary conditions, the fluid properties, the initial conditions and many others. Note that the GMSH software is typically used for mesh generation. Next to that, all the solver setup is also defined in this same file leaving many degrees of freedom to the user for the parametrization of the solver. So one can adapt for instance the non-linear solver, the order of accuracy, the schemes, the stabilisation method, the Jacobian computations as well as several other variables. Finally, everything related to the outputs is also included in this input file. Different types of data can be extracted such that the solution in the field can be extracted but this can also be done for planes and lines. Also, probes and even probesets can be defined to extract the solution at a given point as a *.dat or *.csv file. Additionally, operations can be performed on the outputs to generate for instance averaged solutions while for the probes the possibilities are even larger such that length scales and correlations can directly be computed. For more extensive postprocessing, software such as Paraview can be used to perform the required postprocessing tasks on the extracted fields typically saved as *.mshi files.

5 Computational framework

In this fifth chapter, the computational domain and related topics will be investigated to set the framework for the numerical study. Firstly, the geometric specifications of the numerical domain are defined and some implications are highlighted. The mesh generation is discussed starting from the procedure to create the mesh over to the mesh characteristics until assessing its quality. The mesh and especially its quality are fundamental in numerical studies since it impacts the precision but also the reliability of the computed solution. In order to assess the validity of the mesh, its properties and statistics as well as the wall resolution at the blade level are studied. Finally, the partitioning of the mesh is considered which is necessary for the parallelization of the problem and thus for an efficient simulation by using HPC. Secondly, the boundary conditions are specified and their effects on the flow are investigated. Especially the shortened inlet region requires some specific attention. Then, the initial conditions are discussed which are typically based on the interpolation of an existing solution. The initial procedure employed to get these first simulations running is explained as well in a brief manner. Thirdly, the setup of the numerical solver is presented by explaining the structure of the solver and by enumerating the different chosen solver parameters. Then, the transitory part of the simulations is considered. On the one hand, the numerical convergence of the flow is discussed while, on the other hand, some attention is dedicated to the usage of the computational resources. Since the scale of the simulations is quite significant, the related resources employed are accordingly considerable. Lastly, the numerical instrumentation of the simulations is explained. From data fields that are directly extracted from the solution, over to probe sets which are defined in strategic regions of the domain to capture particular flow features, different elements are addressed in this section. Note that the probe sets are usually structured grids composed of numerous individual probes each monitoring the flow signal at a specific location in the domain. First of all the inlet region is equipped with a probe set to measure the decay of the injected turbulence. Secondly, in the wake region, two planes are monitored with probes to investigate the losses generated by the blade as well as the turbulent content of the wake. Finally, probes are disposed in a specific way all along the blade to analyze the boundary layer flow.

5.1 Computational domain

The geometry of the domain, shown in Figure 5.1, is based on the experimental setup of the SPLEEN linear turbine cascade presented in chapter 2. The latter is used as a benchmark since the goal is to reproduce as closely as possible the flow field encountered in this context. A first computational domain was generated in [3] which was later reused in [4], [30]. During those studies, the domain itself stayed unchanged but the mesh was refined and adapted successively to match the resolution requirements. The approach is based on the idea of simulating a single turbine blade and applying adequate periodicity conditions. On the one hand, the periodicity is defined in the pitchwise direction, characterized by the pitchwise width g, to simulate an infinite row of blades and to simultaneously capture the self-induced effects. On the other hand, the span is also chosen as a periodic direction. Hereby, the blade is idealized by a theoretical infinite span enabling it to get rid of any tip and endwall flow phenomena. By construction, the span of the domain is limited since its effect on the size of the domain is linear and should thus be kept as small as possible due to limited computational resources. The important hypothesis emitted to validate the use of a small span is that the flow is assumed to be quasi-2-dimensional. Thus, a reduced spanwise thickness is adequate to model the large flow features in the 2-dimensional plane. Nevertheless, the span is kept sufficiently thick to simulate the minor 3-dimensional phenomena characterized by turbulent structures appearing in the free-stream turbulence, the boundary layer or associated with the turbulent energy cascade.

In the frame of the present study, some changes are necessary with respect to the domain introduced in [3] to allow an efficient and realistic turbulence injection procedure. For this purpose, the inlet region of the domain has been reduced considerably such that the turbulent structures which will be injected do not need to travel too large distances before reaching the blade. In terms of distance, the inlet section is now located $0.75 \times c_{ax}$ upstream of the blades LE and the complete inlet region has been oriented horizontally in the x direction. Another adaptation concerns the spanwise thickness of the domain which has been slightly increased with respect to the previous versions. This change is required since the turbulence injection uses a cubic precursor domain which will be duplicated and then plugged to the inlet section. Due to the periodicity conditions, the pitchwise width needs to be a finite multiple of the spanwise thickness. Since the pitch is fixed by design, the wanted finite ratio is achieved by slightly increasing the span such that a multiplication factor 8 is obtained between both side lengths. The spanwise thickness no longer corresponds to 7% of the true chord c but to approximately 8%, more precisely $z_d = 4.119$ mm. The downstream region behind the blade is kept unchanged with the outlet section located at 5 pitchwise widths g from the LE of the blade. This prevents the outlet boundary from being too close to the blade and thus from affecting its flow behaviour. Simultaneously, the wake region behind the blade is large enough to perform accurate flow analyses. The presence of the boundary in direct proximity to the blade would not only lead to direct interactions with the flow field but also to potential reflections of perturbations thus provoking nonphysical phenomena in the upstream flow. As mentioned previously, a top view (in the z-plane) of the layout of the computational domain is shown in Figure 5.1 while the corresponding geometrical parameters are summarized in Table 3.1. Note that in the schematic, the main boundaries are highlighted in different colours while the pitchwise width g is used as the length scale.

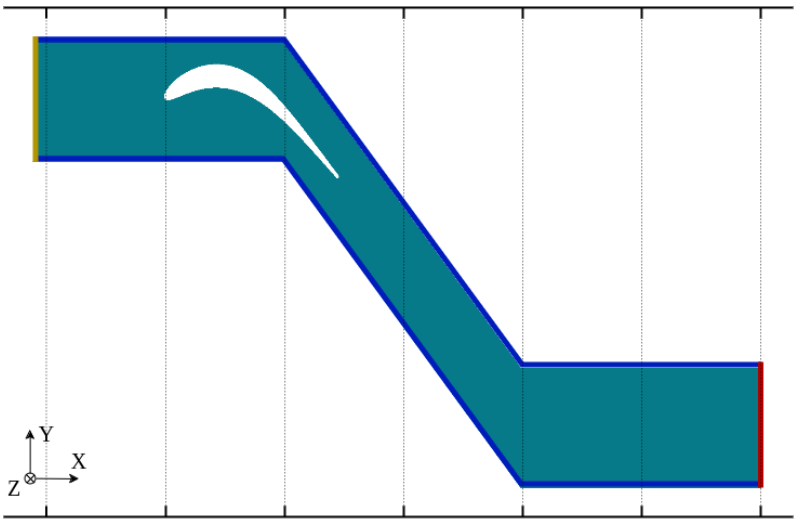

Figure 5.1: Top view of the complete domain with the pitchwise width g used as scaling factor (yellow: inlet, red: outlet, blue: periodic pitchwise boundaries).

After introducing the computational domain, the meshing procedure needs to be discussed. The domain definition as well as the meshing was performed with the GMSH software [22] through the use of suitable Python scripts. The employed mesh, shown in Figure 5.2, is in most aspects based on the mesh designed in [3] and later improved in [30]. It is an unstructured mesh and contains several refinement regions which will be addressed in the following.

First of all, the blade is surrounded by an O-type structured mesh which can be seen in Figure 5.3. The boundary layer mesh adopts perfectly the shape of the blade and is characterized by a thickness of 0.79 mm (1.51% of c) normal to the wall. The size of the elements in direct contact with the surface corresponds to 0.076% of the real chord c in the normal direction while a tangential length of 0.38% of c is chosen. For the elements further away from the surface, an expansion ratio of 1.2 is used such that the elements are sized accordingly in the normal direction. Concerning the TE and LE regions of the blade, specific refinements have been introduced being shown in Figure 5.3. Here, two distinct mesh refinements based on a cylindrical shape are used to accurately match the curvature of both geometric features. The chosen normal resolution is kept the same with respect to the rest of the boundary layer but the tangential resolution is improved being of the order of 0.076% of c as it is the case for

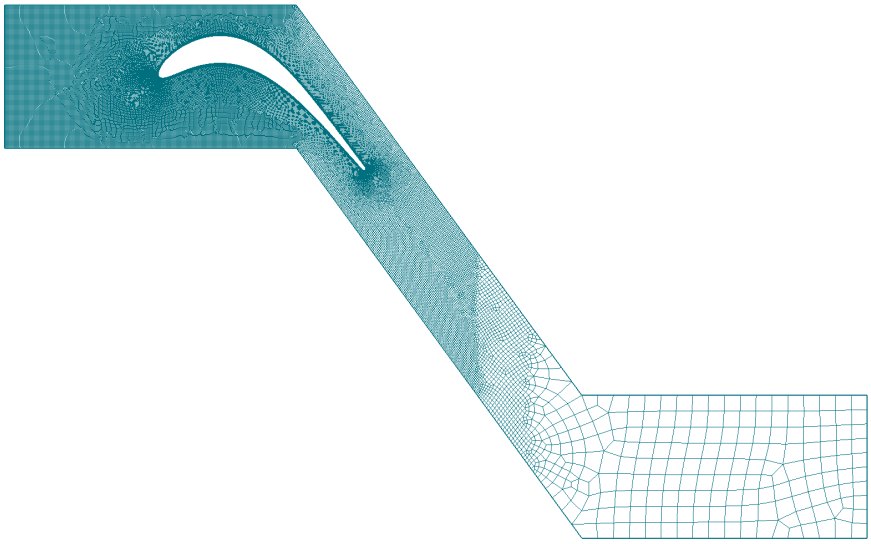

Figure 5.2: Top view of the mesh of the complete domain.

the smallest element length in the normal direction. These specific refinements are required to correctly capture the complex flow phenomena happening at both locations. The second type of mesh improvement concerns the passage between the blades as well as the wake regions. To simplify the task, two box-shaped regions are selected to be refined with a given element size. The finest level is set in a region going from $0.5 \times c_{ax}$ in front of the TE, so approximately the mid-chord, to $0.5 \times c_{ax}$ behind the TE. The element size in this region is set to 0.76% of c. The coarser refinement region occupies a larger region going from $0.8 \times c_{ax}$ in front of the TE to $0.8 \times c_{ax}$ behind the TE. The present refinement level is associated with an element size of 1.52% of c. Finally, the complete inlet region needs to be refined due to the turbulence that will be injected at the inlet section. For this purpose, a reduced element size is imposed from the inlet to approximately the mid-span of the blade, see Figure 5.4. The size of the elements is chosen in accordance with the spatial resolution used in the precursor simulation such that the precision of the flow is kept across both domains and the turbulence can evolve as expected. The imposed cell size corresponds to 0.5% of c and its value is investigated in more detail in chapter 6. The coarsest level in the mesh corresponds to a size of 7.6% of c and is present in the outlet region of the domain typically from $0.8 \times c_{ax}$ behind the TE of the blade onwards. In the spanwise direction, the domain is divided into 34 equivalent layers. The element length corresponds thus to 0.23% of c allowing a precise resolution of the flow features along the span. Note that the boundary shape is matched by the mesh with second-order accuracy resulting in parabolic-shaped mesh edges. This characteristic is important concerning the smoothness of the mesh at the boundary level especially since a 4^{th} order resolution accuracy will be used by the solver. It is important to note that the periodic connections between respective boundaries are already defined during the generation of the mesh. Thus, the spanwise and pitchwise periodicity conditions are implemented at the mesh level by selecting the adequate faces and edges to be connected to each other. Finally, the Frontal-Delaunay algorithm is used the restructure the mesh from a totally unstructured mesh to a much cleaner quad mesh manifesting improved properties in terms of mesh quality.

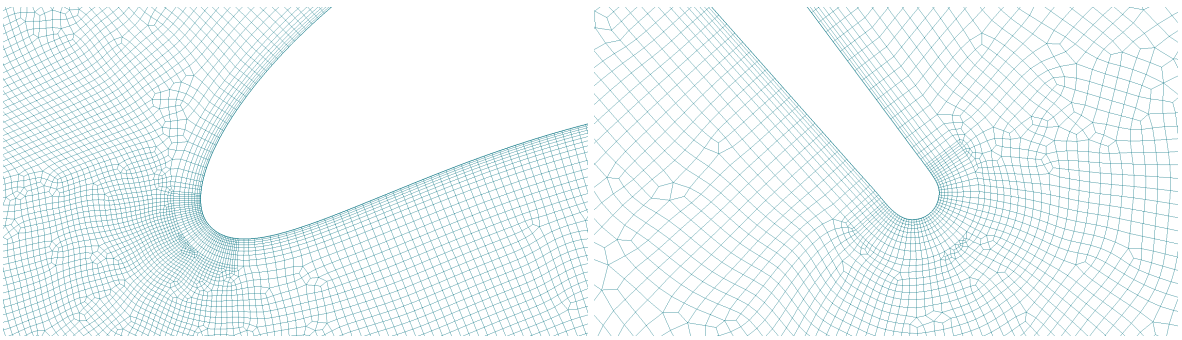

Figure 5.3: Top view of the mesh next to the LE **(left)** and TE **(right)** of the blade.

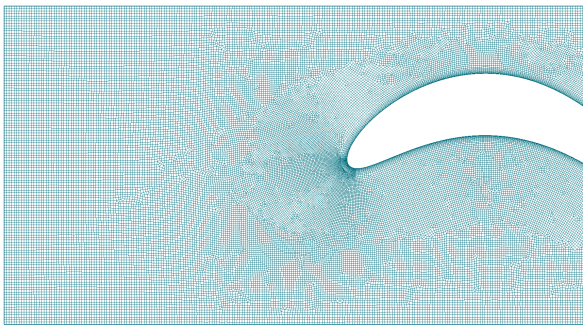

Figure 5.4: Top view of the mesh at the inlet region of the domain.

After generating the computational mesh, its quality needs to be assessed. Most features of the mesh were already checked in [3] and the mesh validity was verified. Since some changes were performed on the mesh, the current mesh needs to be checked before being used. The overall mesh contains $2,020,042$ cells composed nearly completely of hexahedra elements. Nevertheless, a total of 68 prisms are present in the mesh which are exclusively located at the upper corner of the domain (just above the blade). Several properties of the mesh can be extracted from the mesh statistics. The gamma coefficient is defined as the ratio of the inscribed over the circumscribed radius and delivers a measure of the skewness of the cells. For the present mesh, an average gamma of 0.924 is obtained which is a satisfactory value. The Jacobian ratio represents the most important quantity in terms of mesh quality. In our case, it ranges between 0.121 and 1 with an average value of 0.937. These properties are good indicators for the quality of the mesh which is thus well achieved. Combined with the introduced refinement regions, the mesh should be adequate to generate trustful results regarding the flow through the linear turbine cascade. Additionally, a precise resolution level of the flow is expected while keeping a decent computational efficiency.

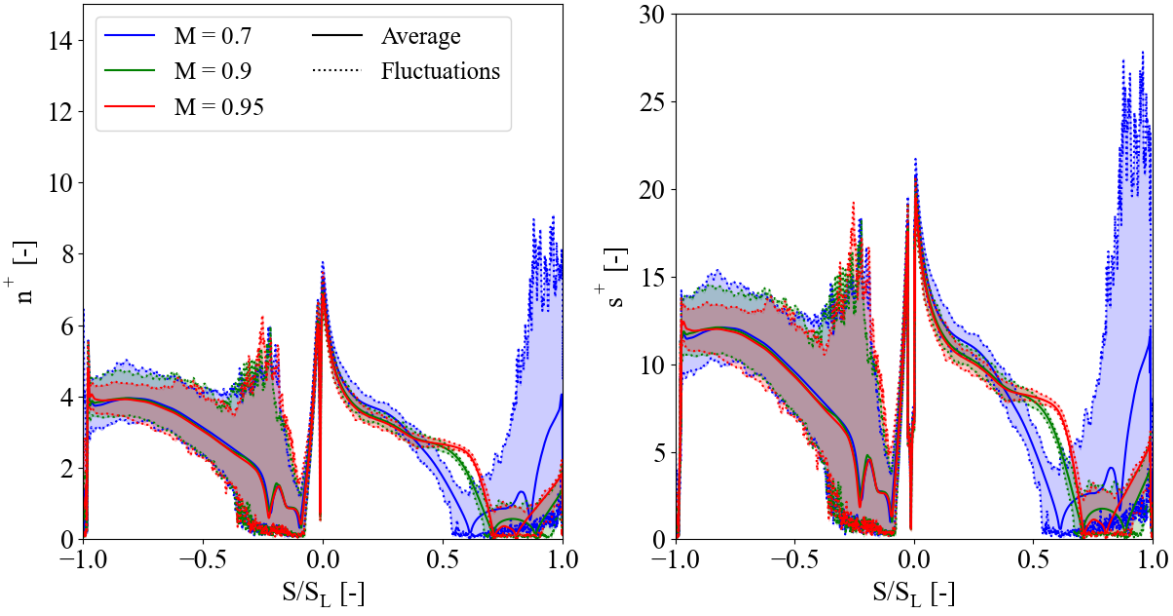

(a) Normal wall resolution.

(b) Tangential wall resolution.

Figure 5.5: Average and extreme values of the wall resolution over the blade surfaces for the different considered cases.

Another verification of the mesh consists of analysing the resolution reached at the surface level of the blade. Indeed, a specific boundary layer refinement has been introduced in direct proximity to the blade to capture the near-wall flow. The nearest mesh point with respect to the wall should lie within the viscous sublayer of the boundary layer (see section 3.3). This approach typically provides good accuracy while limiting the mesh

refinements and thus the required computational resources. The viscous sublayer is associated with wall units typically ranging between 5 and 10. Since in our case a 3^{rd} order interpolation and thus a 4^{th} order resolution is employed, each element can be seen, from a qualitative point of view, as being composed of 3 smaller elements together characterized by 4 distinct interpolation points (in each direction, so overall $4^3 = 64$ points per mesh element as effective resolution). By taking this into account, the valid wall unit range becomes 15-30. In this context, the computed wall resolution around the blade is shown in Figure 5.5. There, the normal and tangential components of the wall resolution are plotted, on the one hand, their average and on the other hand their instantaneous fluctuations. One can notice that the overall trend seems to satisfy the previously discussed condition of the wall resolution. The shape of the different curves is very similar for the three considered configurations while the largest fluctuations are experienced at the end of the suction side for the low Mach number case. The pressure side also manifests considerable instantaneous fluctuations for each case. The magnitude of these variations is nevertheless limited and is still lying in the acceptable range such that one can be confident about the achieved spatial resolution of the boundary layer. The wall units are noticeably smaller in the normal direction than in the tangential one which is linked to the considerably smaller mesh size used in the former direction. After observation of the wall resolution in Figure 5.5, one can deduce that the mesh close to the blade is typically finer than what would be required resulting in a more precise resolution of the BL flow at an accordingly higher computational cost.

The last step in the mesh generation procedure consists of the subdivision of the computational domain into several smaller mesh partitions. This partitioning is necessary to exploit at best the parallelization capabilities of the used super-computer and achieve decent computational efficiencies. By dividing the mesh into smaller sub-parts, the tasks can be distributed to distinct computational instances which are all interconnected but each solves just a small part of the large simulation. The computational cluster used in this study is the Belgian tier 1 super-calculator, Lucia. The high-performance computing (HPC) topic as well as Lucia have been presented in depth in chapter 4. The used cluster is made of several computation nodes which are in turn composed of 128 individual CPUs. To match our needs, the mesh is decomposed in a total number of 512 partitions, each corresponding to approximately $4,000$ mesh elements. The process of handling several distinct partitions simultaneously and in parallel is implemented by using the MPI standard. To further improve the computation time, each of the 512 partitions will in turn be managed by a set of 4 CPUs which will work in parallel by using the OpenMP protocol. Overall, a total of 16 computation nodes will thus be required to run the simulation. The choice of the specific partitioning and parallelization of the case was mainly based on the experience collected in previous computations of the same kind. Considering more partitions and more CPUs per partition would typically increase the computation speed but also considerably impact the computational resources required to run a single simulation. The present segmentation of the simulation in terms of parallelization is thus the result of a trade-off conditioned by the previously mentioned aspects.

5.2 Boundary and initial conditions

After introducing the computational domain as well as the corresponding mesh, the focus is now laid on the numerical conditions applied to generate the flow. In terms of fluid properties considered when solving the compressible flow equations, the ideal gas assumption is made. The equation of state for perfect gas is complemented with a viscosity law given by Sutherland [60]. As mentioned previously, overall 4 different types of conditions are applied at the boundaries of the domain. For each of the three flow configurations considered in this study, the type of condition remains the same but the applied values for these boundary conditions are distinct. Indeed, they are the cause for the intrinsically different flow configurations observed thus having a fundamental influence on the simulation setup. Note that boundary conditions represent an important source of errors in numerical studies and should thus be tuned carefully. The first type is related to the blade body which is considered as a solid wall. This translates into a no-slip condition that is applied at the surface, a synonym of a zero relative velocity at the blade level. Additionally, the blade is assumed to be adiabatic meaning that no heat is exchanged across the surface. Secondly, periodicity is enforced on the upper and lower spanwise faces of the domain. By mirroring both surfaces, an infinite blade span is considered thus neglecting tip effects and other secondary flow phenomena related to a finite span. A periodic condition is also applied on the upper and lower pitchwise boundaries. Indeed not a single blade is thus subjected to the flow in this idealized and simplified view, but a complete linear turbine stage composed of an infinite number of the same blade is simulated. Finally, the inlet and outlet conditions need to be specified. Since dealing with transonic flow conditions, 3 inlet and 1 outlet quantities are required in order

to have a well-defined system of equations to solve. Concerning the inlet section, the three quantities, namely the total pressure, the total temperature and the flow angle are imposed as total conditions. Since turbulence is being injected at the inlet level, specific adaptations are required to include the turbulent fluctuations computed in the precursor simulation within the applied boundary condition. The corresponding procedure as well as the important considerations are presented in chapter 6. Note that the injection of velocity fluctuations will have an effect on the standard total conditions imposed at the inlet resulting in a considerably higher total pressure compared to the applied one. Knowing this issue, adequate adjustments are integrated inside the turbulence injection procedure in order to limit these undesired effects and compensate them directly when applying the boundary condition. For the outlet section, only the static pressure is applied. Additionally, it is assumed that the coarse mesh close to the outlet combined with the considerable distance with respect to the blade is sufficient to prevent any unwanted interactions with the boundary and any undesirable reflections. The boundary conditions applied at the inlet and outlet sections for each considered case are summarized in Table 5.1.

Table 5.1: Considered flow conditions.

Quantity	**Units**	**Case 1**	**Case 2**	**Case 3**
$M_{\text{is,out}}$	[-]	0.70	0.90	0.95
$p_{0,\text{in}}$	[Pa]	10,779.390	9,500.244	9,318.311
p_{out}	[Pa]	7,771.164	5,617.115	5,213.220
$Re_{\text{is,out}}$	[-]		70×10^3	
$T_{0,\text{in}}$	[K]		300	
α_{in}	[°]		36.3	

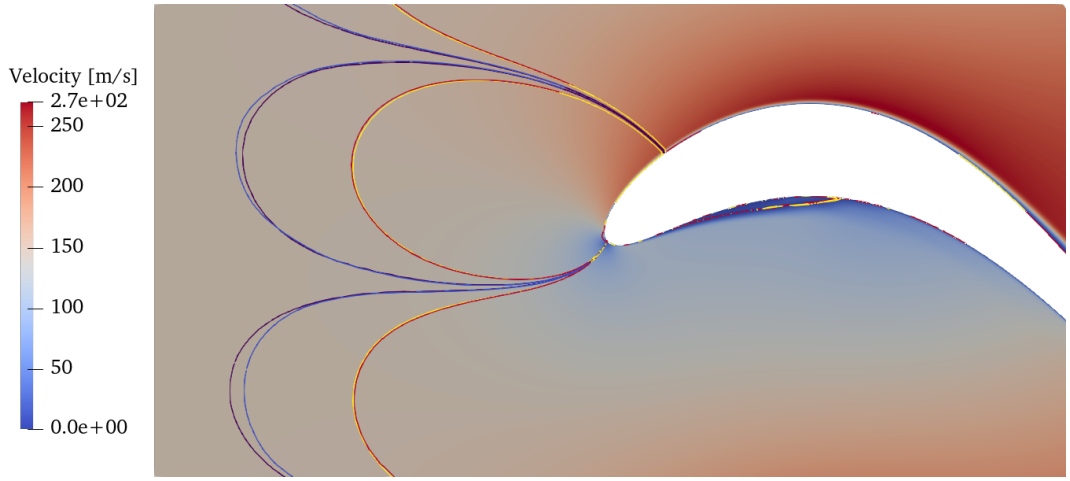

Figure 5.6: Mean velocity field in the shortened domain for the $M = 0.7$ case with isolines plotted for given flow deviations with respect to the inflow angle $\alpha_{\text{in}} = 36.3°$. In red, the line corresponds to a $\pm 0.5°$ deviation from the nominal angle α_{in} and the blue one depicts a $\pm 0.1°$ variation, both for the case of the shortened inlet section without turbulence injection. The yellow and the violet lines correspond respectively to a $\pm 0.5°$ and a $\pm 0.1°$ deviation for the baseline case configuration considered in [4] (with inlet section located further away).

A detailed study of the mesh as well as the boundary locations has been conducted in [3] with a satisfactory outcome. Indeed, the proximity of a given boundary with respect to the blade body shouldn't have a measurable effect on the flow field. In this context, the inlet boundary requires to be further investigated due to its significant rapprochement to the blade. As discussed previously, this geometric feature is essential in order to limit the magnitude of the injected turbulence because of the more intense expected dissipation rate. The effect of the reduced inlet length is illustrated in Figure 5.6. There the baseline case studied in [4] is compared with the configuration

in which a shortened inlet is present but without any injected turbulence. Hereby, the slightly increased deviation in the flow field is observable as can be seen in Figure 5.6. This gap between both cases can be assumed to be negligible since it closes rapidly such that for a flow angle of 0.5° with respect to α_{in} both configurations seem to coincide. More precise observation allowed us to see that the location of the stagnation point did not move thus not feeling any effect of the closer inlet section. Those investigations allow us to deduce that the effect of the smaller inlet region is observable as illustrated by Figure 5.6 but can be assumed to be negligible with respect to the direct flow around the blade.

Another important feature is the spanwise thickness. It should be large enough to allow three-dimensional flow structures to exist while this width is strongly limited by the computational cost that it causes. Regarding the structures in the close wall region, precise contours can be recognized when looking at the instantaneous spanwise skin-friction distribution around the blade surface. The turbulence injected and passing through the inlet region should by design conform with the spanwise thickness since it has been generated in a cubic domain of corresponding size. Finally, the strong turbulent activity generated in the wake region can be affected by the limited spanwise thickness. The wake itself is especially characterized by a vortex street pattern which is typically dominant in a 2-dimensional way. For the locally released or built 3-dimensional vortices and turbulent structures the sufficient span should be verified. This will be done in section 7.5 by assessing the correlation length scales of the flow structures along the spanwise direction.

To initialize the flow field in the domain, an interpolation operation is performed on a complete and statistically converged flow solution developed in [4] corresponding to the standard case without turbulence injection. Even though the domain and the mesh experienced several changes with respect to this standard configuration, it has been observed that the flow was able to rapidly adapt to the updated domain. Therefore, the transitory required for the injected turbulence to reach the blade and establish a converged flow field is assumed to last longer than transient behaviour related to the mesh change. The initial setup of the flow from scratch was performed in [3] where the used approach is detailed. Briefly, the procedure consists of applying the chosen total conditions not only at the given boundaries but simultaneously in the complete flow domain at the beginning. Additionally, the flow in the complete domain is characterized by a small Mach number typically set to 0.01 and oriented in the streamwise direction. By doing so, local perturbations, often of acoustic nature, can convect away thus allowing the flow to establish faster.

5.3 Solver parameters

As discussed in chapter 4, ArgoDG is the software used to solve the flow equations. It implements the DGM resulting in interesting properties characterized by a high resolution combined with a stable behaviour. The flow equations considered are the compressible NSE (continuity, momentum and energy) which are solved at each time step of the simulation. Additionally, a non-dimensionalization operation done with respect to some reference quantities is performed on the solution of the flow equations. The choice of these reference parameters is made for $p_{ref} = 6,000$ Pa and $T_{ref} = 260$ K. To numerically solve the flow problem, adequate discretization of the equations is required. In terms of temporal discretization, the choice is made for the implicit BDF2 which is a second-order backwards difference time-integration scheme. A time step equal to 10^{-7}s is chosen in order to satisfy the CFL condition with respect to the smallest elements contained in the mesh. Even though the solver is implicit and the condition is thus not necessary to satisfy, it usually generates better and more reliable numerical results. To improve the computational performances, it is assumed that the Jacobian matrix does not change significantly between consecutive time steps. The size of the matrix is directly related to the number of DOF thus its computation is expected to cost considerable amounts of resources due to the large size of the mesh. By assuming a slow variation with respect to a single time step, instead of computing the Jacobian matrix every time instance, a delay is chosen over which the matrix is frozen before being recomputed. The delay is set to 5 time steps in this framework allowing to speed up the computations while still having sufficient resolution and stability. The chosen temporal scheme is employed with a 10^{-4} non-linear tolerance. In this context, it is interesting to mention that as a non-linear solver, it has been opted for the Newton method. The latter is extended with the iterative GMRES (generalized minimal residual) solver equipped with matrix preconditioning using the Jacobi method. Regarding the spatial discretization of the equations, the SIPDG (symmetric interior penalty discontinuous Galerkin) scheme is chosen. The scheme integrates a penalty function which is required to stabilize the computation of the diffusive fluxes. The solution computed with the DGM is by construction

of piecewise high-order polynomial type with relaxed continuity constraints at the cell interfaces. Overall, the DGM is thus more suited for problems of convective nature resulting in the necessity of employing a penalty method as the SIPDG to correctly take into account diffusive phenomena.

5.4 Convergence and computational resources

To extract meaningful results from the numerical simulation, the flow needs to be converged to a statistically stable configuration in which the flow phenomena are fully established. Indeed, the considered cases are compressible flows and intrinsically unsteady. In that context, the flow will not converge to one single solution but be characterized by instantaneous fluctuations provoked by highly unsteady phenomena such as the vortex street or other turbulent features. Its overall statistics should nevertheless on average converge to steady quantities describing the macroscopic flow behaviour. The starting point of the simulations are complete and statistically converged flow fields obtained in [4] without free-stream turbulence. By injecting the turbulent fluctuations through the inlet section, a considerable transitory is required to develop the flow and eliminate the transient features. On the one hand, the turbulence needs to be convected to the blade while on the other hand, the flow phenomena induced by the free-stream turbulence need to establish. A first manner to assess the convergence of the flow consists in directly analysing the flow field and observing if the flow structures develop as expected until reaching a coherent behaviour. Secondly, the statistics are investigated to check if the measured quantities fluctuate significantly or if the targeted steadiness of the statistics is reached. Finally, the conservation of the physical quantities as the mass, momentum and energy can be verified. In steady problems, these conservation laws should be strictly verified when reaching numerical convergence. For unsteady compressible problems, these quantities are usually not conserved instantaneously. Nevertheless, especially when reaching statistically converged states the conservation needs to be true at least on average to keep the physical pertinence of the solution. Practically, a balance can be performed for the conserved quantities by monitoring and combining the respective fluxes across the different boundaries of the domain.

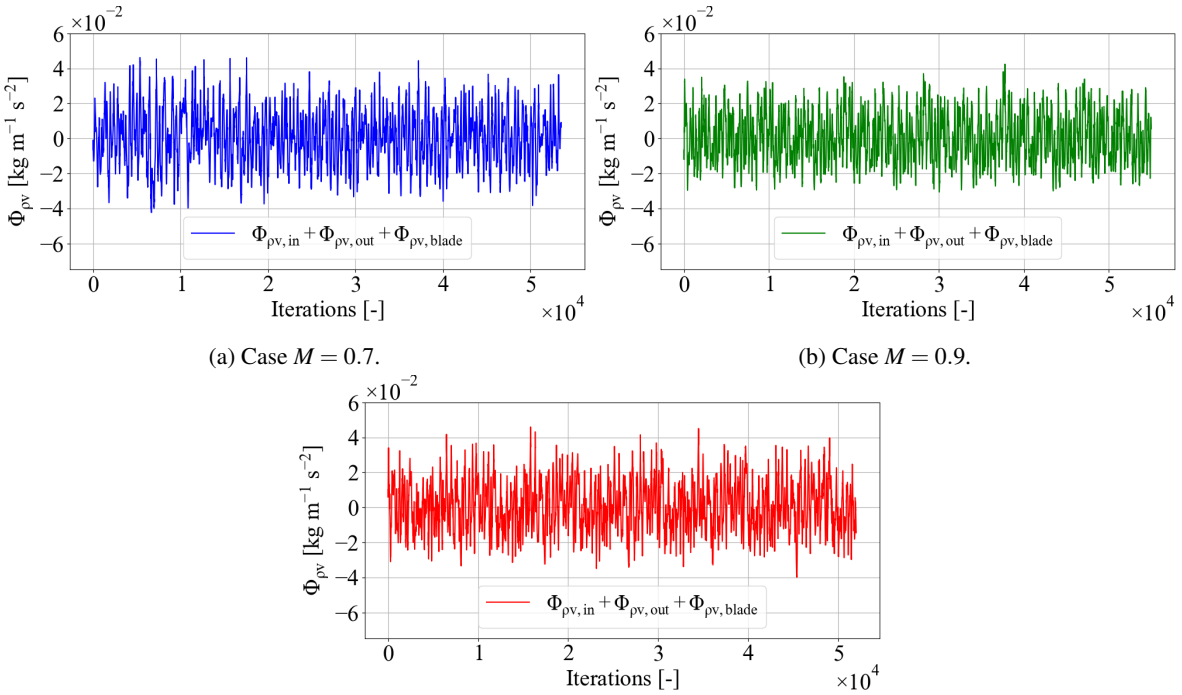

(a) Case $M = 0.7$.

(b) Case $M = 0.9$.

(c) Case $M = 0.95$.

Figure 5.7: Evolution of the momentum fluxes along the pitchwise direction (y) during the numerical transitory for the different considered cases. The conservation of momentum in the computational domain is assessed by summing the inlet, outlet and blade contributions.

Figure 5.7 shows the evolution of the conservation of the momentum along the pitchwise direction with respect to the simulation time steps of the numerical transitory for the different considered cases. Therefore, the momentum

fluxes across the inlet, outlet and blade boundary are combined to assess a force balance. The combined momentum fluxes should be conservative and thus be equal to zero on average when reaching statistical steadiness. Note that the momentum flux along the y-direction is representative of the pitchwise effort applied on the blade. It can be observed in Figure 5.7 that the resultant momentum flux fluctuates significantly all along the transitory simulation. Especially the low Mach number case exhibits strong oscillations due to its stronger unsteadiness. The observed fluctuations are sensibly higher than what has been observed in the previous studies (see [3], [4], [30]). This discrepancy can be linked to the injection of turbulence. By exploiting Taylor's frozen flow assumption as well as the other hypotheses, the injected turbulence does not perfectly verify the NSE leading to small discontinuities observed at the injection location which in turn affect the instantaneous momentum flux balance. Nevertheless, the resultant flux oscillates around 0 which implies that the quantities are conserved on average, being an indicator of the physicality of the numerical result. Especially towards the end of the transitory one can notice that the observed behaviours seem to repeat. This behaviour can be linked to the finite streamwise length of the blended turbulence box leading to a redundancy in the injected free-stream turbulence and thus in the flow itself. Additionally, the conservation of mass and momentum along the streamwise direction has been investigated and manifests similar behaviours. Here, the unsteady fluctuations around 0 are again present and the observed repetitions towards the end of the transitory appear as well. The numerical transitory simulated to converge the initial flow fields towards statistical steadiness were performed on $68,000$, $55,000$ and $61,000$ iterations respectively related to the $M = 0.7$, 0.9 and 0.95 cases. These simulation durations correspond respectively to 16.6, 14.9 and 16.5 convective times based on the axial chord and velocity. The different verifications made to assess the transitory based on instantaneous flow structures, statistics and conservation laws give us good confidence about the convergence of the flow field and the statistical steadiness reached. These considerations are fundamental in the perspective of continuing the simulation and accumulating the flow statistics.

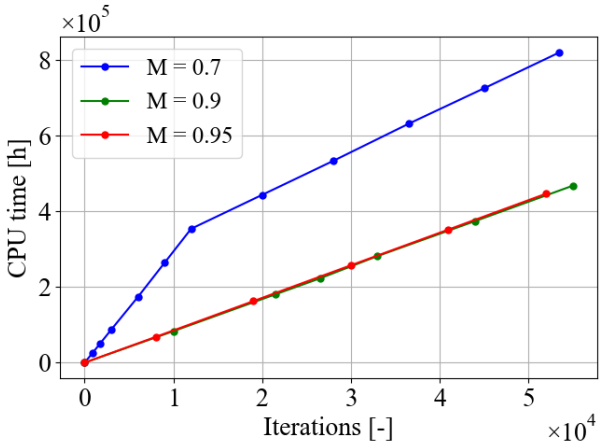

Figure 5.8: Used computational resources in terms of total CPU hours with respect to the transitory of the studied configurations.

In Figure 5.8 are shown the computational resources employed to simulate the transitory of each of the three flow configurations. The scale used for the graph is CPU hours which are obtained by multiplying the real computation duration (in hours) times the total number of CPUs used. By running the computations on 16 nodes and knowing that each node is composed of 128 CPUs, overall 2048 CPUs are used simultaneously for a given simulation. Thus, the amount of resources used is considerable and justifies the use of a cluster combined with an important parallelization of the case to run the simulations. One can observe in Figure 5.8, that typically half a million CPU hours were needed for the computation of a single transitory corresponding to a total of $50,000$ iterations with a 10^{-7} time step. Furthermore, the evolution of the resources used behaves the same way for each considered case by following a nearly constant slope which seems to be just slightly different from one case to another. A striking feature is contained in the computational resources usage related to the $M = 0.7$ case. Indeed, a considerable slope change can be observed around iteration $12,000$. The phenomenon can be traced back to the computation of the Jacobian matrix by the numerical solver which represents a very costly operation. The topic has already been introduced in more detail in the previous subsection. For the iterations before $12,000$, the Jacobian matrix, whose size is of the order of the computational domain, was computed at every single time step. Afterwards, the assumption was made that the variation of the matrix from one time step to the next one was of

negligible extent. In this context, the Jacobian matrix was then frozen during 5 consecutive time steps before being recomputed. This change allowed us to observe a drastic improvement in terms of computation time. For the other configurations, this assumption was made from the very beginning such that constant slopes can be observed for these cases.

5.5 Data extraction

Due to the large size of the computational domain, data extraction represents a fundamental challenge. Saving the complete flow field would lead to immense usage in terms of storage resources and would not be feasible. Next to that, the post-processing functions used to treat this data would be confronted with a very large amount of data impacting the memory and computation time of these procedures. One way to limit memory usage is to store data on selected reference planes and surfaces instead of outputting the solution in the complete domain. Additionally, approaches such as co-processing which are performed simultaneously with the simulation have much potential and allow the user to strongly reduce the amount of stored data. Another benefit of this approach is that the number of manipulations required in terms of post-processing is considerably reduced.

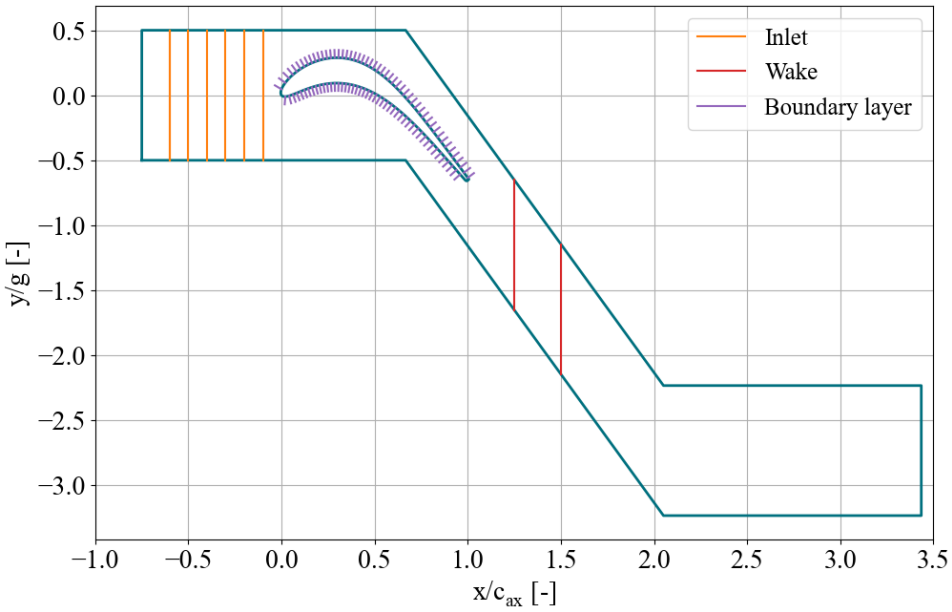

Figure 5.9: Disposition of the probes in the computational domain.

In the frame of this study, the outputs stored during the simulation are specifically individualised to match the needs in terms of wanted post-processing data. On the one hand, field data are extracted using the *.msh* format on significant surfaces such as the blade surface, the inlet section or a single spanwise plane. Besides storing instantaneous data, co-processing tasks are performed in order to extract temporal and/or spanwise averages on the planes of interest which are accumulated all along the simulation. A single flow field is also extracted on the complete domain in order to visualize the instantaneous turbulent structures present in flow by using for instance the Q-criterion. On the other hand, specific probe sets are defined in the domain to extract the data at precise locations. The two-dimensional layout of these probe sets is shown in Figure 5.9, where it should be mentioned that all probe sets are extruded along the spanwise direction with 50 individual probes. To fulfil the needs, overall 3 regions are equipped with such probe sets. Firstly, the inlet region counts 6 probe grids covering the whole pitch and span. These grids are placed equidistantly from each other and located between $0.6 \times c_{ax}$ to $0.1 \times c_{ax}$ from the LE in the streamwise direction. The inlet probes are introduced in order to analyse more precisely the evolution of the injected turbulence before interacting with the blade. Secondly, the wake is fitted with two probe grids located at the planes 0.25 and $0.5 \times c_{ax}$ downstream of the TE. They allow us to investigate the turbulent content of the wake as well as the losses observed in the wake. Both grid locations correspond to the specific measurement planes used in the experimental study. In the experimental framework, they are referred to as planes 5 and 6, as can be seen in Figure 2.2. Thirdly, a more complex probe set is defined regarding the

boundary layer analysis. Indeed, as depicted in Figure 5.9, their disposition matches exactly the shape of the blade. By distributing probes all around the blade, the tangential evolution of the BL quantities can be examined all around the blade. Appropriate extrusions of the probes are performed in the normal direction to the blade surface, such that velocity profiles as well as other quantities can be studied adequately in the region close to the surface. The probe sets are not used to extract the evolution of an instantaneous flow signal but to compute meaningful statistical variables of the monitored quantities during the computation. Indeed, averages, deviations, autocorrelations and spectra are accumulated all along the simulation for each probe before performing spanwise averaging. Next to that, the extrusion of the probe sets along the span as well as the corresponding periodicity can further be exploited to compute spanwise correlations and length scales. Note that in addition to the previously mentioned outputs, a small number of monitors are extracted. The latter contain the complete temporal flow signal of a chosen quantity at a given location. A handful of such points are chosen in the wake and in the base flow region. Additionally, the same approach is used to extract the evolution of the fluxes on significant surfaces. This is the case for inlet and outlet sections where especially the density and momentum fluxes are of interest to monitor the flow rates as well as the conservation of the physical quantities. The evolution of the fluxes on the blade surface is also extracted since it provides a measure of the instantaneous effort applied to the blade through its momentum fluxes.

6 Turbulence injection

This chapter focuses on the generation of turbulent inflow data which is required to produce a given free stream turbulence level in the flow. After being injected at the inlet section, these turbulent fluctuations will then travel downstream until reaching the blade with which they will interact. Firstly, the turbulence injection method used for this study will be presented in more detail. The employed approach consists of a precursor method solved in a simplified triply periodic cubic domain. The computed turbulent flow field is obtained by simulating the decay of homogeneous and isotropic turbulence, short DHIT. A sharper look is then taken at the solver setup of the auxiliary simulation. It follows the analysis of the computed results which are characterized by the decay of the initially imposed turbulence spectrum. Afterwards, the approach to extract the flow field at the targeted instant corresponding to a specific turbulence level is detailed. Then, the post-processing of the extracted turbulent flow is explained. This final step is required to generate the appropriate inflow data that can later directly be injected into the main domain. Finally, the evolution of the injected free-stream turbulence inside the main domain is investigated. The turbulent decay is quantified by using the statistics accumulated with the probe set located over the inlet region.

6.1 Precursor simulation

In this study, a turbulence library-based method consisting of a precursor simulation has been selected. The auxiliary simulation solving the decay of homogeneous and isotropic turbulence (DHIT) is performed on a triply periodic cubic domain with the in-house flow solver ArgoDG, developed at Cenaero. The precursor method is directly implemented inside of the solver ArgoDG. The procedure is presented by Rasquin et al. [47].

After running the precursor simulation, a flow field is obtained corresponding to a realization of a turbulent free-stream flow. This flow field is the result of the DHIT computed in a cubic domain characterized by three homogeneous and periodic directions. The mean velocity of this flow is by definition equal to zero such that the flow field itself can be seen as a combination of velocity fluctuations u''. These fluctuations will then be superimposed with the mean inlet velocity $\overline{u}_{\text{in}}$ of the main domain before being injected. The term injection is a simplified description of the procedure since the computed turbulent fluctuations are in fact successively applied as instantaneous boundary conditions on the inlet section. The solution from the precursor simulation is extracted at a specific time step for which the targeted turbulence level is reached. Therefore, the turbulence is typically quantified and monitored by the TKE and the length scale. For the injection process, the inlet of the main domain is then swept through the precursor solution at the velocity $\overline{u}_{\text{in}}$. The imposed turbulent fluctuations are obtained by interpolating the precursor flow field on the inlet plane. To be compliant with the existing inlet conditions, the applied conservative variables, the total temperature and total pressure, are evaluated based on the injected velocity field $u'' + \overline{u}_{\text{in}}$. Note that the imposed total temperature should not be strongly affected by the turbulent flow field while the total pressure will typically decrease more rapidly due to higher dissipation. The aforementioned procedure is valid under some circumstances, themselves related to two main hypotheses:

- Taylor's frozen turbulence hypothesis presented in section 3.2 needs to be satisfied, allowing to neglect the non-linear interaction between the mean flow and the turbulence. The turbulent fluctuations should thus just be convected by the mean flow without any major interaction requiring that the convection time scales are much smaller than the turbulence time scales.

- The second hypothesis concerns the homogeneity of the flow field which requires the flow to be homogeneous in each direction consequently even in the streamwise one.

The various performed tasks related to the turbulence injection procedure are explained in more detail in the following subsections.

6.1.1 Decay of homogeneous isotropic turbulence

To compute the turbulent flow field, the precursor simulation is based on a decaying homogeneous isotropic turbulence inside of a triply periodic and homogeneous cubic domain. This case corresponds to a known configuration in turbulence which has been studied in depth in the past (see [9], [45]). The periodicity conditions applied at all faces of the box combined with the homogeneity property cause the generated flow field to be isotropic hence the statistical quantities as the length scales satisfy this property. Although compressibility effects play a major role in the flow around the blade, the assumption is made that the turbulent fluctuations at the inlet are incompressible. Next to a uniform initial total temperature and pressure, an initial incompressible velocity field is imposed in the precursor domain followed by the decay of the homogeneous isotropic turbulence until the target time step. The latter is reached when the statistical flow properties in the precursor simulation match the targeted turbulence level which is often specified in terms of the TKE and the correlation length. In the present study, especially the TKE will be the dictating parameter since the integral length scales are limited due to the reduced span of the main domain. The initially imposed velocity field has a zero mean velocity and is defined following the method proposed by Rogallo [50]. The energy content of this field is given by a spectrum defined by Passot and Pouquet [44]. The initial TKE and turbulent length scales can be tuned with respect to the precursor domain size by adapting the width and amplitude of the spectrum. The former is defined by the number of modes used for the discretization of the spectrum. The latter concerns the choice of the peak wavenumber of the Passot-Pouquet spectrum as well as its related numerical value. This parameter is very important since it strongly influences the flow behaviour. Larger peak wavenumbers lead to a higher number of turbulent structures present in the domain but simultaneously require a finer mesh for a given spectral resolution width of the turbulent energy cascade. The integral length scale which describes the largest turbulent structures is mostly dependent on the overall size of the precursor domain and less on the precise input parameters.

6.1.2 Setup

In order to limit the computational cost as well as the memory usage, the size of the precursor domain should be chosen adequately. Knowing that the auxiliary domain corresponds to a triply periodic cube, the computation can be performed on a small box which is then replicated in the pitchwise directions to fill the whole inlet section. In this case, the size of the cube is set to the spanwise thickness of the main domain equal to 4.119 mm corresponding to approximately 9% of c_{ax}. Thus, only one box is needed in the spanwise direction while 8 copies of the box will be placed next to each other along the pitchwise direction. Note that this process can introduce spurious spatial correlations in the inflow turbulence. As discussed previously, the turbulence length scales possible to represent are strongly linked to the size of the computational domain thus a smaller cube will considerably constrain this flow property.

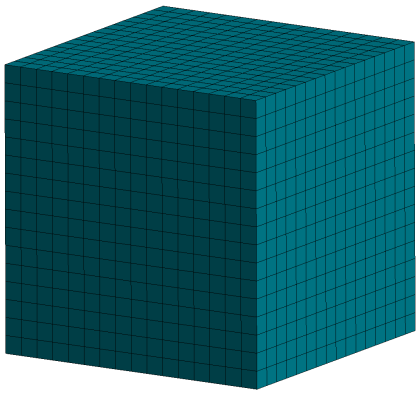

Figure 6.1: Mesh of the precursor domain.

The computational domain and the corresponding mesh are generated with the open-source mesh generator Gmsh [22]. The obtained mesh is composed of 16 elements in each direction and is shown in Figure 6.1. The mesh refinement level is chosen to be the coarsest possible while preserving the sufficient resolution required for the DNS of the DHIT. An important aspect is that the mesh of the precursor domain needs to be in accordance with the mesh at the inlet region of the main simulation. Otherwise, a suboptimal use of the available resources is happening. Either the precursor mesh is more refined and the smallest scales of the injected turbulence are too small to be captured by the main mesh thus yielding to a rapid dissipation of these flow structures. Or the main mesh is more refined allowing it to capture smaller structures than what is injected through the inlet thus making this refinement unnecessary, a synonym of a waste of resources.

The imposed initial condition is mainly deduced from the total temperature and total pressure set at the inlet of the main domain summarized for the different cases in Table 5.1. From these quantities combined with the ideal gas hypothesis and the Sutherland law, the flow properties are computed such as the viscosity, density, thermal conductivity, etc. Next to that, a small Mach number, typically set to 0.1, is chosen to characterize the flow which is basically representing turbulent fluctuations. A corresponding characteristic velocity and TKE is then further deduced from the imposed Mach number. Although the case is solved for a compressible flow, the flow behaviour should behave in a nearly incompressible manner due to the low Mach number. Concerning the parametrization of the imposed Passot-Pouquet spectrum, the characteristic length is defined by the size of the precursor domain. The second wavenumber is chosen to be the peak wavenumber due to beneficial properties producing a smoother decay of the turbulence. A total of 48 modes are included defining the width of the spectrum. This number is chosen with respect to the effective resolution of the mesh and thus corresponds to the number of DOFs present in each direction. Finally, the amplitude of the spectrum is related to the previously computed TKE.

Concerning the numerics, the implicit time integrator BDF2 based on Jacobian-free Newton-GMRES preconditioned with block-Jacobi is used. An interpolation order equal to 3 with lagrangian projection is chosen as in the principal simulation. Furthermore, the same time step equal to 10^{-7} s is adopted to be as close as possible to the main simulation. Satisfying the CFL condition is not strictly necessary when using an implicit solver but it is a good practice. For the precursor simulation, since adopting the time step of the main simulation and handling significantly smaller flow velocities, this condition is generously satisfied by having a CFL number of 0.04.

6.1.3 Computation

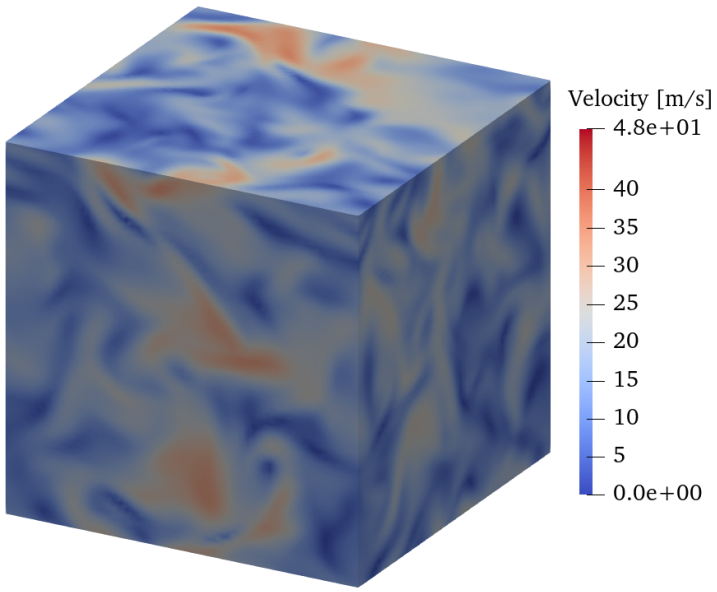

Figure 6.2: Velocity field in the turbulence box at the extraction iteration for the $M = 0.95$ case.

After taking into account the developments made in the previous sections, the precursor simulations for the 3 considered cases can be run. Each simulation is performed on 7000 iterations which thus corresponds to 0.7 ms. As will be discussed later, this time span seems to be sufficient for the flow field to establish a realistic HIT cascade. Additionally, it is made sure that the duration is long enough to cover the convection time needed for the turbulent flow to travel from the injection location to the blade's LE. This second condition needs to be satisfied in order to adjust the level of turbulence that will be injected in the main domain. In the following, the results obtained for the $M = 0.95$ case are analysed in more detail. Note that the procedure applied as well as the results obtained for the other cases are very similar and thus not explained in further detail in this section for redundancy reasons. Nevertheless, their respective simulation results and graphs are included in section A.1. The computational resources used to perform the precursor simulations are approximately 320 CPU hours for each of the cases. This resource usage represents only a minor contribution to the overall computational cost of the study discussed in section 5.4.

In Figure 6.2, the velocity field in the precursor domain at the extraction instant is shown for the $M = 0.95$ case. The velocity fluctuations can clearly be seen representing the turbulent structures that have been generated inside the box. The evolution of the turbulence intensity inside of the precursor domain for $M = 0.95$ is plotted in Figure 6.3. The TI which is directly derived from the TKE describes the magnitude of the turbulence contained in the flow. It can be seen that the TI smoothly decreases exponentially over time. At the very beginning, a slower decay combined with few strong fluctuations can be observed which is probably due to the initial establishment of the flow structures and the turbulence cascade. Indeed, the initially imposed Passot-Pouquet spectrum does not necessarily represent a physical flow solution such that a transition process takes place to generate a real HIT flow. Quite large turbulence levels of approximately 22% in terms of TI can be observed at the very beginning which corresponds to a TKE of 1880 m^2/s^2. Note that the major hypothesis for injecting realistic turbulence through the precursor simulation approach is the Taylor hypothesis of frozen turbulence detailed in section 3.2.

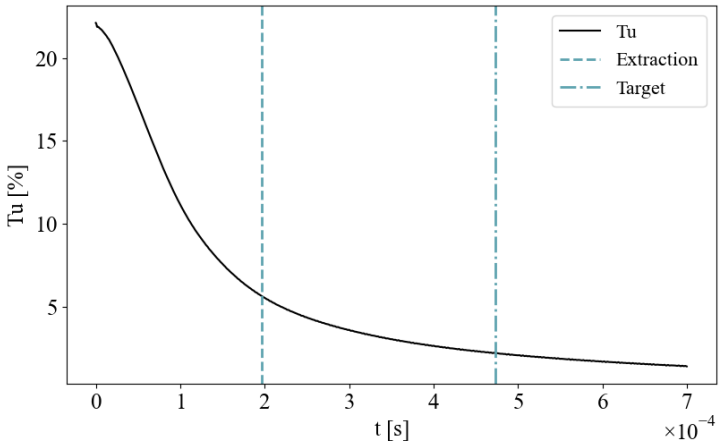

Figure 6.3: Temporal evolution of the turbulence intensity Tu in the turbulence box for the $M = 0.95$ case.

The extraction instant corresponds to the iteration at which the precursor flow field is frozen and exported to be injected into the main domain. This is done by extracting the flow field on a structured grid of probes of sufficient precision. The specific instant at which this procedure is performed is dictated by the measured turbulence level. Therefore, the previously discussed TI is of specific interest whose evolution is shown in Figure 6.3. Knowing that the TI measured experimentally at $0.5 \times c_{ax}$ upstream of the blade is equal to 2.34% (see Table 2.1), the idea is to match these conditions to reproduce as accurately as possible the flow around the blade. From the injection location, the turbulence level decays significantly over the inlet region due to dissipation phenomena. The strength of this decay is closely linked to the characteristics of the turbulent flow. A higher TKE will typically lead to a more important decay. The integral length scale plays another essential role in the behaviour of the decay. Experimentally, it is measured to be 12.34 mm but in the numerical approach with the limited domain dimensions such large lengths can not be obtained. Indeed, the turbulence box size is of approximately 4 mm such that integral length scales of approximately 1 mm are obtained during the precursor simulation as can be seen in Figure 6.4. Note that initially strong variations of the measured length scales are visible which are again linked to the set-up of the physical turbulent flow. Afterwards, the evolution takes place more smoothly

with their common mean value varying around lengths slightly larger than 1 mm ($\approx 25\%$ of z_d). From a statistical view, the three length scales measured in each direction should be equal to each other when dealing with HIT. The discrepancy observed in the isotropy is thus due to local and unsteady turbulent structures in the flow that in a statistical view do not have any preferred direction. The match of the length scales with respect to the experimental approach is by design not possible due to the reduced span of the main domain. The option to enlarge the span is not feasible in the frame of this study since the span has a strong impact on the overall size of the numerical domain and thus on the computational resources required to run the simulations. This limiting feature concerning the turbulent length scales will have a considerable impact on the evolution of the flow with respect to the experiments. Indeed, a much more pronounced decay will be experienced over the inlet section in the numerical simulation due to these properties. Thus, trying to match perfectly the experimentally measured TI at the plane located half a chord upstream of the LE of the blade does not seem to be the best choice. Indeed, the turbulence level that really matters is the one directly encountered by the blade and not the one measured at some point upstream. The turbulence grid in the experimental setup is designed to produce a TI of more or less 2.5% at the blade. Knowing that the 2.34% TI measured at the half-chord plane will further decay from the sensor location until reaching the LE of the blade, a corresponding TI needs to be chosen that will represent the target quantity. After taking into account these different factors, the choice is made for a 2.2% turbulence intensity which should be obtained at the LE of the blade. This targeted TI corresponds to a TKE of 18.57 m^2/s^2.

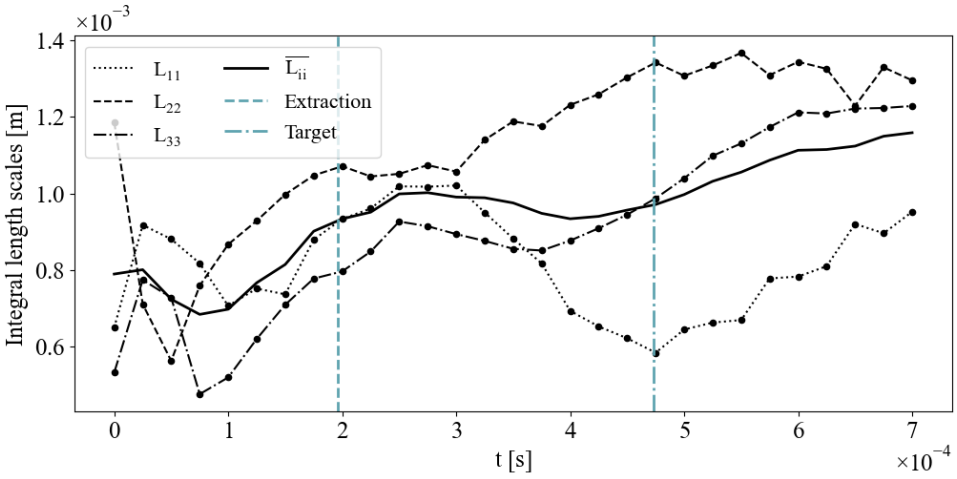

Figure 6.4: Temporal evolution of the integral length scales in the turbulence box for the $M = 0.95$ case.

The turbulence is injected at the inlet of the computational domain from where it will further evolve until reaching the LE. The choice of the extraction instant is thus crucial for obtaining the previously discussed target condition at the blade level. The approach to determine this instant is based on the Taylor hypothesis (see section 3.2). This approximation implies that the turbulent structures have a much larger time scale than the convective mean flow and thus that both phenomena coexist without interfering with each other. Following this idea, it is assumed that the injected turbulence will evolve in the same way it has decayed in the triply periodic precursor domain independently of the main flow. The latter will only convect the turbulent fluctuations with it in the streamwise direction. Assuming the evolution matches the one observed during the precursor simulation, the precise extraction instant can be defined by knowing the time needed to convect a given velocity fluctuation from the injection location to the LE of the blade. This time span is characterized by the mean convection velocity present in the inlet region of the domain. The mean inlet velocity can be extracted from the computations performed without turbulence injection in [4]. For the $M = 0.95$ case, the mean convective velocity over the inlet $\overline{U}_{in}$ corresponds to 166.01 m/s. By considering the length of the inlet section as well as the flow angle, the time delay between extraction and target moment is given by

$$\Delta t_{in} = t_{LE} - t_{in} = t_{target} - t_{extract} = \frac{L_{in}}{\overline{U}_{in}} = \frac{0.75 c_{ax}}{\overline{U}_{in}\cos(\alpha_{in})}. \tag{6.1}$$

By plugging in the values, one obtains a time span of 0.2767 ms. The iteration at which the flow is extracted from the precursor simulation is then deduced with respect to the target iteration at which a 2.2% TI is reached. Thus, as depicted in Figure 6.3, the TI corresponding to the extraction instant is equal to 5.647% while the equivalent

TKE is equal to 122.64 m^2/s^2. The extraction and target conditions for the different cases are summarized in Table A.1.

Figure 6.5a shows the evolution of the normalized TKE using a logarithmic scale. It contains similar information as the TI evolution shown in Figure 6.3 but the logarithmic representation allows to highlight some specific features. Thus, after an initial period over which the HIT establishes being described by a transient plateau, the decay of the TKE takes place by following a constant slope. The slope itself is characterized by an exponential factor n which typically lies between 1.15 and 1.45 as discussed in the literature [9], [45]. The evolution of the ratio of the TKE over the dissipation is shown in Figure 6.5b. It can again be seen that the canonical decay of HIT establishes after passing a transitional beginning. The initial evolution is described by a first plateau followed by an exponential decrease until reaching a minimum. After this extremum, k/ε follows the typical slope of $1/n$ describing the turbulent decay. Note that the two figures show that both target and extraction moments lie within the region where the turbulent cascade is well established. More precisely the canonical DHIT is reached describing a physical turbulent flow which will then be frozen and extracted at the selected time step before being injected into the main simulation.

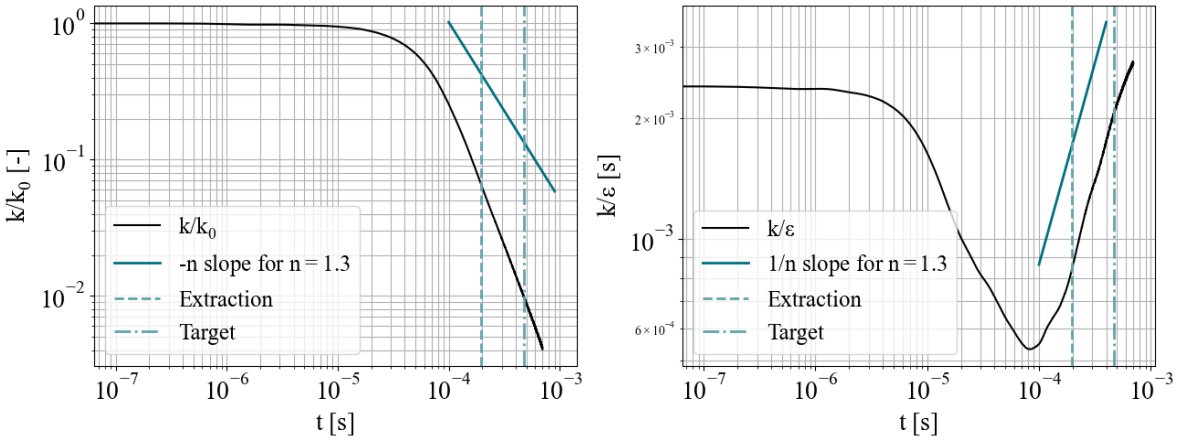

(a) (b)

Figure 6.5: Temporal evolution of the normalized TKE **(left)** and the ratio of the TKE over dissipation rate **(right)** in the turbulence box for the $M = 0.95$ case.

In Figure 6.6 is shown the evolution of the dissipation during the precursor simulation. Firstly, the total dissipation rate $\overline{\varepsilon}$ is represented by a solid line and is obtained by taking the temporal derivative of the spatially averaged TKE. Its evolution is described by a significant initial growth followed by an exponential decrease after reaching a first maximum value. Additionally, it is characterized by pronounced short-time oscillations. Secondly, W_d describes the work performed through viscous dissipation. The dash-dotted curve follows the same overall evolution as $\overline{\varepsilon}$ but does it in a completely smooth manner. The general shape of these two curves is thus described by a very strong initial dissipation increase due to a high turbulence level at the beginning. Another factor is the non-physicality of the initially imposed flow field which leads to a high dissipation rate, especially for non-coherent fluctuations. After the development towards a canonical DHIT, the dissipation follows an exponential decrease which is mainly dictated by the simultaneous exponential decrease of the TKE. Note that different criteria exist to evaluate the state of the turbulence cascade but the DHIT is typically said to be established after the mathematical inflexion point of $\overline{\varepsilon}$. The specific point provided by this rule of thumb is located in the decay region after the maximum and changes the concavity of the curve during the decay. Thirdly, W_p (can be considered. The dotted line corresponds to the work carried out by pressure dilatation. Its shape is strongly characterized by the previously mentioned short-time oscillations. After an initial part with very striking variations followed by a small overall increase, its shape is exclusively affected by these small and fast oscillations. By combining both works W_d and W_p one can obtain the overall work performed which is denoted by W (dashed line). Ideally, these two curves, total dissipation $\overline{\varepsilon}$ and total work W, should match perfectly. Initially, large discrepancies are visible between both curves. Those differences are due to numerical dissipation happening when solving the flow equations. The gap between both lines steadily becomes smaller and seems to be closed before reaching the extraction instant, as can be seen in the zoom in Figure 6.6. This characteristic is important in our case since numerical dissipation

is not a physical phenomenon and the main goal consists of injecting fluctuations describing a realistic turbulent flow. Additionally, the closure of the gap is an indicator of the sufficient resolution achieved during the precursor simulation of the turbulent flow. Note that the oscillatory behaviour of the dissipation rate can directly be related to the pressure dilatation effects which are precisely resolved during the simulation due to a small enough time step.

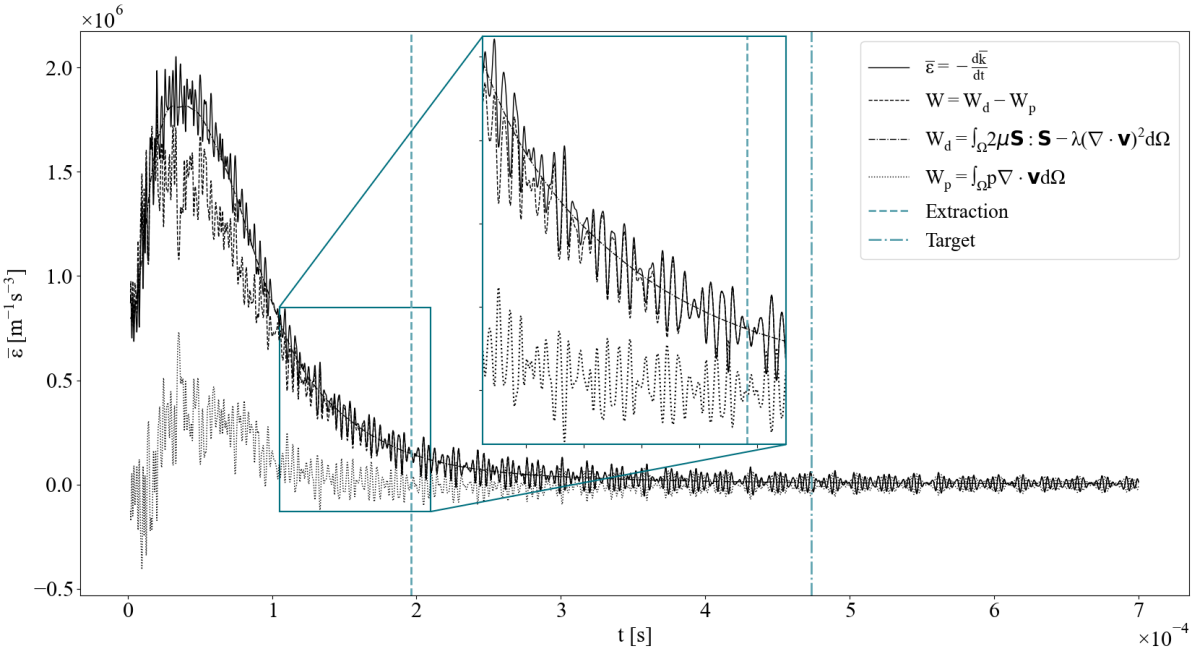

Figure 6.6: Temporal evolution of the dissipation rate in the turbulence box for the $M = 0.95$ case.

Figure 6.7 shows the energy spectra at the extraction and target instants of the precursor simulation. They provide a quantitative illustration of the Kolmogorov cascade which describes the energy distribution phenomenon in a turbulent flow. In a simplified manner, the large scales contain large amounts of energy which are then passed to smaller scales. This process goes on until reaching the smallest scale in which the energy is dissipated through viscous effects. In the intermediate region, also called the inertial subrange, the energy is conserved and just passed down in an inviscid manner to the smaller scales. This subrange is traditionally described by a $-5/3$ slope. Even though the presence of a reduced integral length scale is strengthening the turbulent decay phenomenon, a small intermediate region characterized by a constant $-5/3$ slope is present in both spectra. Additionally, one can notice that the overall energy content is much smaller at the target than at the extraction moment. This is well in line with the decay of the turbulence happening all along the simulation.

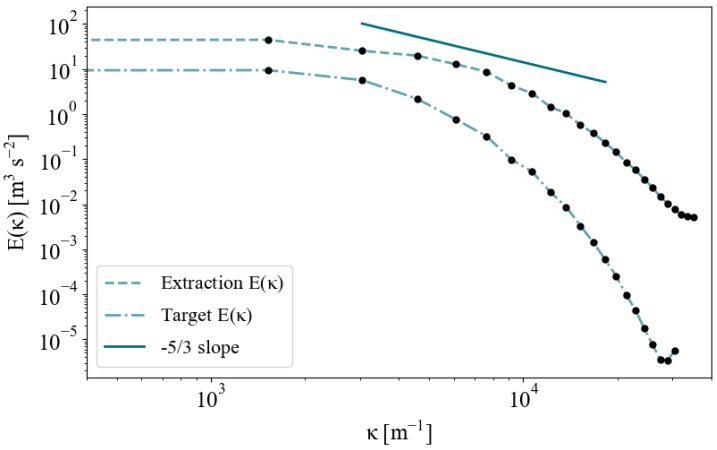

Figure 6.7: Energy density spectrum at the extraction and target instant for the $M = 0.95$ case.

6.1.4 Blended turbulence box

The last step before injecting the free stream turbulence consists of a blending process [47]. The periodicity and geometrical properties of the problem are exploited to form a blended domain composed of the concatenations of a series of generated pseudo-realizations. Herefore, random rotation, permutation and translation operations are applied to the extracted flow field which are then merged together. By concatenating the different pseudo-realizations back together a long blended box is obtained. This process is used to avoid the strong correlation of the flow in the streamwise direction which is considered to be more detrimental than in the span- and pitchwise directions. If only a single computed box was used for the injection, the flow structures and characteristics would be very repetitive since the identical flow would be injected all over again. This strong streamwise correlation is not in accordance with the fundamental properties of actual chaotic turbulence in which such striking correlations are not observed. The approach of using permutations to take advantage of the periodicity of the cubic domain was first introduced by Xiong et al. [70] and later developed by Larsson [34]. The direct concatenation of the permuted flow fields would produce discontinuities at the interfaces. To correct this issue, a blending process is applied ensuring that no discontinuities remain present in the turbulent flow field. The blending operation which is applied over a chosen blending length will typically generate unwanted compressibility effects in the flow. Those generated irregularities correspond to spurious dilatation effects which can be corrected by solving a Poisson equation. This operation basically consists of performing a projection of the velocity field on a divergence-free space.

The implementation of this method allows to perform a total of 24 distinct permutations of the initially extracted flow field. This maximum value is chosen here as well such that the streamwise correlations can be limited as much as possible. By merging the 24 pseudo-realizations back together using the discussed blending process, the long turbulence box shown in Figure 6.8 is obtained. Note that for the blending operation, a stencil of 9 probeset points per pseudo-realization was chosen thus corresponding to a blending length of nearly 20% of the total size of the box.

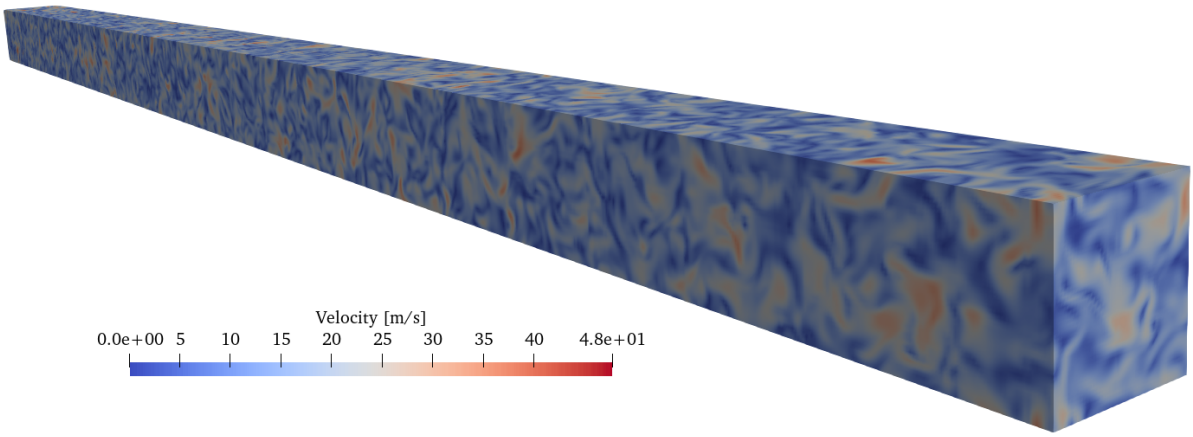

Figure 6.8: Blended turbulence box for $M = 0.95$ case.

6.2 Free-stream turbulence in the main simulation

For injecting the turbulence from the precursor domain into the main simulation, the blended box shown in Figure 6.8 is swept through at the convective inlet velocity. The velocity fluctuations are then superimposed at the inlet section with the mean flow. The convective flow at the inlet boundary is dictated by the applied total condition which is characterized by an imposed total pressure, total temperature and flow direction. The velocity distribution over the section as well as the remaining quantities are computed from these imposed conditions. After being injected, the turbulence continually decays by travelling downstream until reaching the area of interest, the blade. Finally, flow fields as shown in Figure 6.9 are obtained for the different Mach number cases. It has to be mentioned that the vorticity is presented with a logarithmic scale, which can lead to wrong interpretations. The scaling is only used to better visualize the free-stream turbulence and it should not be forgotten that the turbulent content of the wake is considerably higher. Both types of turbulent features are thus not of comparable magnitude.

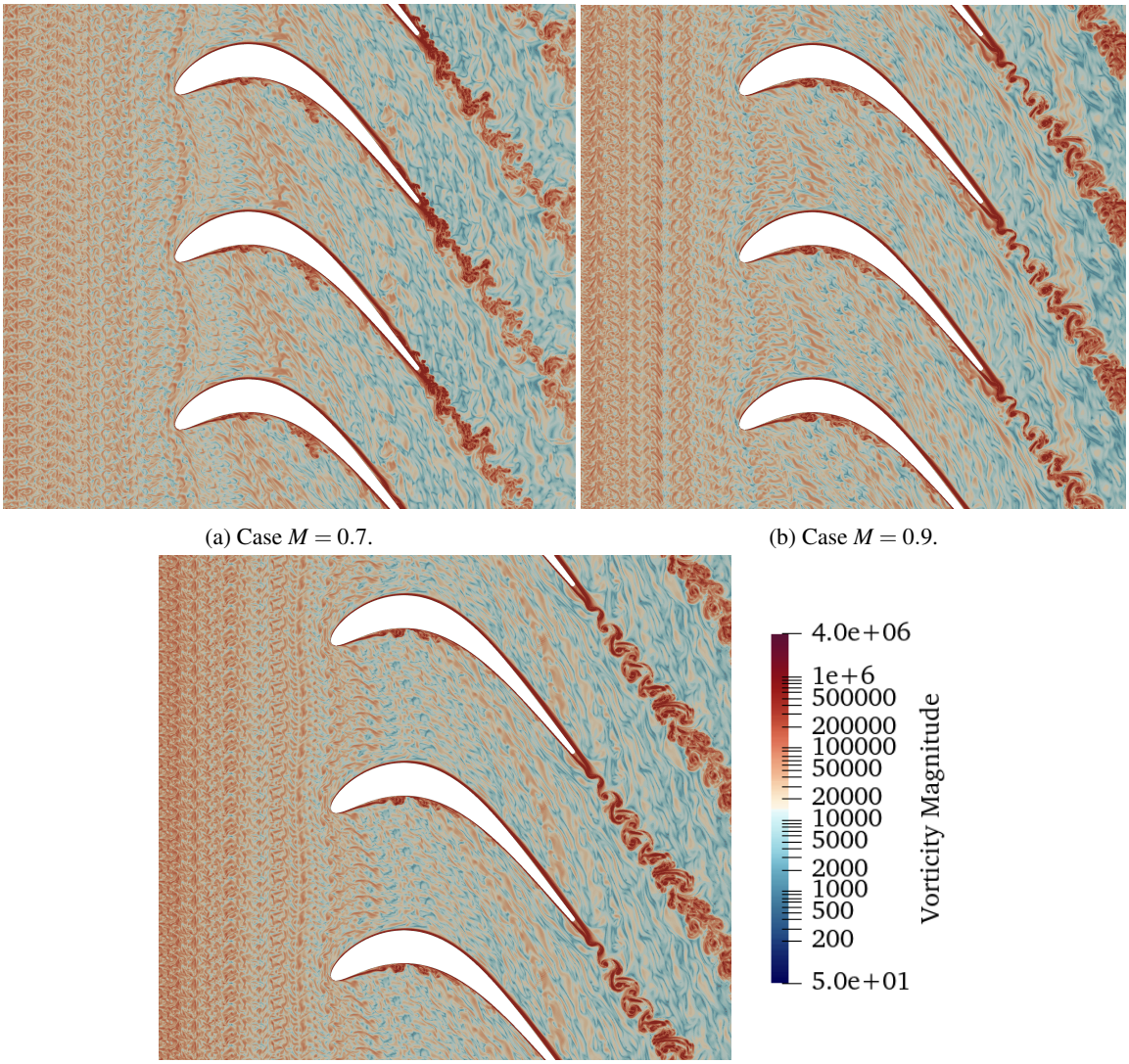

(a) Case $M = 0.7$.

(b) Case $M = 0.9$.

(c) Case $M = 0.95$.

Figure 6.9: Instantaneous vorticity field in the spanwise plane $z = 0$ for the different M cases. Note that a logarithmic scale is used to enhance the visualization of the injected free-stream turbulence. Several copies of the flow field are repeated in the periodic pitchwise direction for aesthetic reasons.

In Figure 6.9 can be observed that the turbulence seems to continually decrease in intensity over the inlet region, as expected. A striking feature is the strong redundancy of the free stream turbulent structures in the pitchwise direction. Indeed, the same blended turbulence box is replicated 8 times along the pitch such that according repetitions can be observed in the flow field. Until reaching the level of the blade, the injected turbulence is steadily convected downstream with the pitchwise coherence persisting. The turbulent structures travelling through the flow passage are elongated and deformed due to the induced accelerations. The structures directly impacting the blade are strongly deviated and are expected to interfere with the boundary layer and the transition phenomenon. These flow interactions are only present if the turbulence level is sufficient and if the accelerations experienced at the LE of the blade are not too important such that the turbulent fluctuations are directly diminished. In the wake region, one can see that the elongated turbulent structures are travelling downstream and potentially interfering with the wake generated by the blade. The pitchwise coherence of the turbulence can typically lead to issues and unphysical behaviours in the flow if too dominant. Nevertheless, the large majority of the observed structures repeated along the pitch are convected through the flow passage and only a minor subset directly interacts with the

blade. This reduced portion typically corresponds to 1 or a maximum of 2 turbulence box lengths such that the fluctuations interacting with the blade should be distinct enough. Indeed, the structures should be uncorrelated enough to provide a sufficient level of randomness which represents a fundamental property of turbulent flows. Additionally, the turbulent structures are strongly distorted and deformed in direct proximity to the blade partially breaking the striking pitchwise coherence. Also, the phenomena occurring on the pressure and suction side of the blade are sufficiently separated and independent from each other which limits the potential effects related to the redundancy in the flow. Note that ideally an additional blending process should have been performed along the pitchwise direction as was done in the streamwise direction in order to break the strong coherence. However, the streamwise coherence effects of the injected turbulence were considered to be more important. The blending effort was thus focused exclusively on the limitation of the redundancy along the streamwise direction to the detriment of the pitchwise one.

In Figure 6.10 are shown the evolution of the TKE over the inlet region for the different considered cases. As a reference, the TKE decay predicted by the precursor simulation (see Figure 6.3) is added to the graph by converting the temporal evolution into a spatial one using the inlet convection velocity. For each of the considered cases, a considerable shift can be observed in the evolution of the TKE such that the decay is slower than expected. This behaviour in turn leads to stronger turbulence levels reaching the blade. Following the trend of the decay monitored in the main simulation, the initial TKE is first slightly smaller than predicted when being injected at the inlet. This can be related to the fact that the turbulence does not perfectly satisfy the NSE initially leading to observable discontinuities across the first few cells following the inlet. This abrupt variation in the flow linked to the slight non-physicality of the solution will provoke a considerable dissipation and thus a noticeable decrease in TKE just after the injection. Afterwards, the slower decay of turbulence in the main domain catches up with the predicted precursor TKE evolution until surpassing it. The origin of this shift with respect to the predicted decay will be investigated in the following.

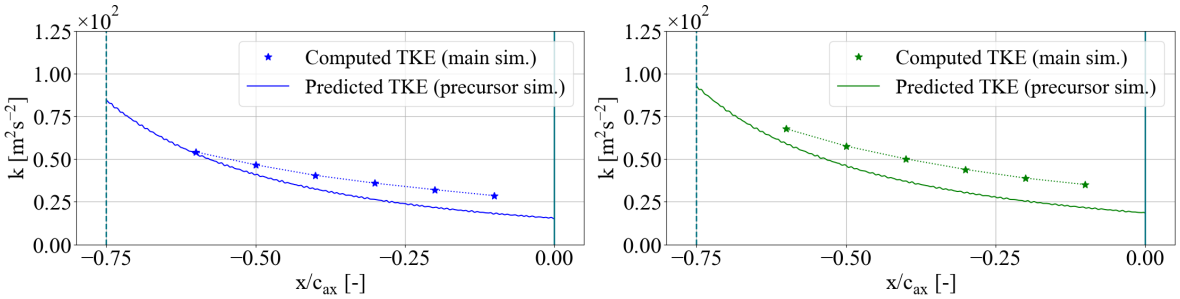

(a) Case $M = 0.7$.

(b) Case $M = 0.9$.

(c) Case $M = 0.95$.

Figure 6.10: Streamwise evolution of the temporal, spanwise and pitchwise averaged TKE characterizing the turbulent decay. The quantities are measured at 6 reference planes over the inlet region of the domain for the different considered cases. Note that only the configurations with turbulence injection are presented. The predicted TKE decays in the precursor simulations are included for comparison. The vertical lines represent the inlet section as well as the LE locations.

In Table 6.1 are summarized the most important turbulence intensity values related to the different cases and approaches. It is noticeable that the numerical TI levels at the plane $0.5 \times c_{ax}$ are much higher than the experimental ones. This can be linked to the smaller integral length scales and thus the stronger dissipation of turbulence pro-

voking a faster decay. To obtain comparable TI at the blade level, the turbulence needs to be accordingly higher at the mentioned upstream plane. The precursor simulation predicted a decay leading to a TI of 2.2% close to the blade. In the main domain, these values are not observed even though the overall evolution trend is similar. Due to the considerably slower turbulence decay, the TIs obtained at the LE of the blade are in the range of 2.8-3.0% depending on the case. Hence, the numerically measured quantities are accordingly higher than the corresponding experimental values. Since the fundamental free-stream TI range for the flow in high-speed LPT lays between 1.5-3.5%, as discussed in chapter 2, the turbulence levels obtained in the numerical study still satisfy this TI range.

Table 6.1: Experimentally predicted and measured as well as numerically predicted and computed free-stream turbulent intensity [%] at reference locations in the flow domain.

Streamwise location (x)	$-0.5 \times c_{ax}$	0 (LE)

	Case 1	**Case 2**	**Case 3**	**Case 1**	**Case 2**	**Case 3**
Exp. predicted (corr.)	2.59			2.42		
Exp. measured	2.34			-		
Num. predicted (precursor sim.)	3.62	3.49	3.74	2.20		
Num. computed (main sim.)	3.87	3.89	4.20	2.83	2.93	2.97

After analysing the evolution of the TKE and equivalently the TI decay, one can study in more detail the evolution of the Reynolds stresses $\overline{u_i' u_j'}$. With the TKE being computed using the trace of the Reynolds stress tensor, the direct analysis of the Reynolds stresses allows us to evaluate the directional information as well as the off-diagonal cross-product terms. Figure 6.11 shows the evolution of the spanwise and pitchwise averaged Reynolds stresses over the inlet region. A striking anisotropy is observable among those quantities. Indeed, one would expect the diagonal terms to have more or less the same values in the context of homogeneous and isotropic turbulence. As can be observed, the pitchwise fluctuations seem to be much more dominant over the spanwise and streamwise ones. Even though the Reynolds stresses decay over the inlet region, the anisotropy between the three directions seems to persist. Concerning the off-diagonal terms, they take on average values close to zero but one can see that the $\overline{u'v'}$ component differs slightly from the other two by taking non-zero negative values which are decaying over time. These observations indicate that a significant anisotropy is present in the free-stream turbulence injected in the flow.

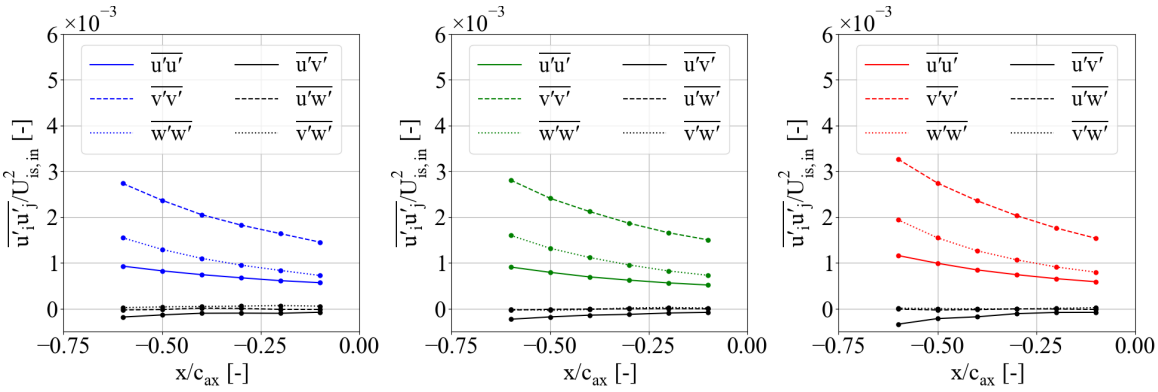

(a) Case $M = 0.7$. (b) Case $M = 0.9$. (c) Case $M = 0.95$.

Figure 6.11: Streamwise evolution of the temporal, spanwise and pitchwise averaged Reynolds stresses. The quantities are measured at 6 reference planes over the inlet region of the domain for the different considered cases. Note that only the configurations with turbulence injection are presented.

Further investigations can be performed by considering the integral length scales which are based on the spatial correlations. In Figure 6.12 are shown the integral length scales evaluated in the spanwise direction for velocity fluctuations in the three distinct spatial directions. The length scales typically grow over the inlet region but at a very small rate such that they can be seen as quasi-constant. It can be observed that the L_{ij} computed for velocity fluctuations in the streamwise direction is significantly smaller than the quantities in the two other directions. For homogeneous and isotropic turbulence, the integral length scale computed along a given direction with velocity fluctuations considered along the same direction should be twice the size of the length scales computed for velocity fluctuations in the two other reference directions (see [46]). In the present case, this would translate by the fact that L_{zz} should be twice as large as L_{xz} and L_{yz} which both should be of the same size. Practically, this is not what can be observed in our case. Indeed, L_{zz} is more or less twice as large as L_{xz} but L_{yz} does not satisfy this isotropy condition. L_{yz} is approximately of the same size as L_{zz} thus highlighting an observable anisotropy in the free-stream turbulence.

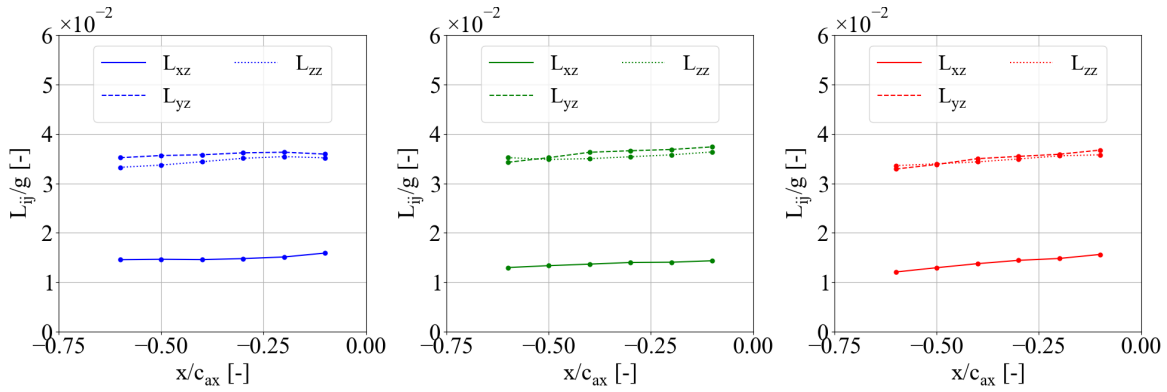

(a) Case $M = 0.7$. (b) Case $M = 0.9$. (c) Case $M = 0.95$.

Figure 6.12: Streamwise evolution of the average normalized integral length scales computed along the spanwise direction (z) for velocity fluctuations monitored in the existing spatial directions. The spatial correlations are measured at 6 reference planes over the inlet region of the domain for the different considered cases. Note that only the configurations with turbulence injection are presented.

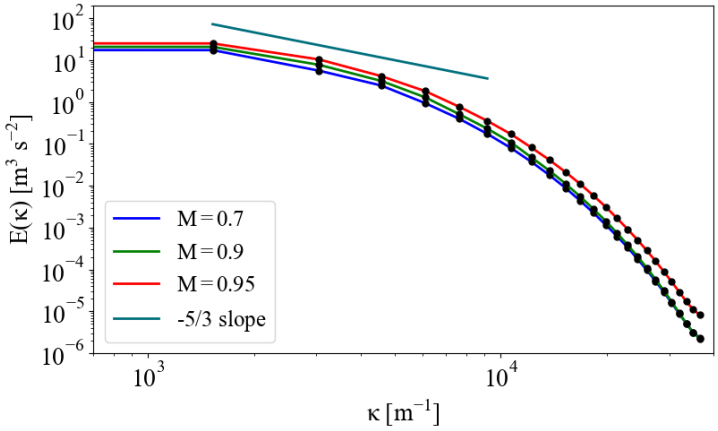

Figure 6.13: Space-averaged energy density spectrum extracted at the reference plane located at $0.5 \times c_{ax}$ in front of the LE, for the different considered cases. Note that only the configurations with turbulence injection are presented.

Finally, the spectral content can be analysed in Figure 6.13. The graph contains the spanwise and pitchwise average of the energy density spectrum at the streamwise plane located at $0.5 \times c_{ax}$ in front of the LE. The averaged behaviour is similar between the three configurations even though a higher turbulent content can be observed for the higher Mach number cases. Also, a steeper slope can be observed for the $M = 0.9$ case when taking a look at the smaller scales. The $-5/3$ slope is plotted as a reference line to mark the inertial subrange of the turbulence

cascade. This intermediate region is well defined in the averaged spectra such that the predicted slope is followed over a considerable range of length scales described by κ. Note that the energy density spectrum is a quantity which possesses no directional information such that the anisotropy observed for the previous quantities cannot be assessed here.

To conclude this chapter, the free-stream turbulence decay experienced over the inlet region of the main domain is overall slower than what has been predicted by the precursor simulation. The TI reaching the blade is thus proportionally higher than what was targeted and thus what was measured in the experimental approach. Parallely, a considerable anisotropy has been observed in the injected turbulence which should by design be statistically isotropic and homogeneous. These deviations from the expected turbulence evolution can be led back to different potential origins. First of all, a factor can be the resolution of the turbulence. In the context of the precursor simulation, the resolution of the turbulence was nevertheless checked and a sufficient level of accuracy has been achieved. In the main domain, the same element size as in the precursor domain was attributed to the elements located in the inlet region. A small difference consists in the spanwise resolution which was dictated by the blade physics. In the spanwise direction, an element size of approximately half with respect to the pitch- and streamwise element lengths is used. Secondly, the geometrical specifications can play a role in the observed discrepancies. The flow accelerations and deviations induced by the blade or even just the domain dimensions can have an impact on the convected turbulence. Also, acoustic disturbances emitted from the blade can potentially travel upstream and interfere with the turbulence injection procedure. Thirdly, the strong pitchwise coherence generated by replicating 8 times the same blended turbulence box can provoke some undesired effects. Fourthly, the Taylor hypothesis on which the whole turbulence injection approach is based can be a considerable source of errors. If too large turbulence intensities are handled, the turbulent flow can not be divided any more into a convective mean flow and linearly superimposed fluctuations. Indeed, the non-linear interactions between both features become then more important and can no longer be neglected. When injecting the turbulence, the spatial gradient is not taken into account leading to some non-physical fluctuations and potential discontinuities at the injection location. Finally, a possible problem source can consist of the type of boundary condition used and its implementation in terms of the turbulence injection process. In the present case, a total condition is applied at the inlet section such that the velocity is not imposed directly. The velocity distribution is in fact computed with respect to the flow conditions at the inlet as well as the imposed total quantities. This operation can provoke significant issues in terms of turbulence injection if for instance the superimposing of the fluctuations, the flow direction or the corrections performed in terms of total pressure are not handled correctly. These different potential error sources can have more or less severe implications on the free-stream turbulence. At the current state of the study, the precise reasons why these discrepancies are observed in terms of turbulent decay and anisotropy were not yet found but the previously mentioned elements can play their part in this context. Nevertheless, the turbulence intensity level obtained at the blade is in an acceptable range with respect to what has been targeted in the experimental campaign. The flow phenomena induced by the free-stream turbulence should thus correctly develop and appear in the flow field even though some differences in terms of intensity and isotropy have been observed. The obtained results should however be treated with caution due to the previously discussed discrepancies in terms of injected turbulence. Potentially, these mismatches in terms of turbulent content could have an impact on the overall flow behaviour leading to spurious features and thus incorrect measurements and performances.

7 Results and discussion

This last chapter will be dedicated to the numerical results accumulated during the simulations. Overall three flow configurations characterized by their outlet isentropic Mach numbers are considered: $M = 0.7$, 0.9 and 0.95. This wide range of Mach numbers allows us to consider the LPT flow in on- and off-design conditions. Especially for the high Mach numbers, the compressible effects will play an important role and give rise to interesting observations. The configurations considered in this present study are simulated with free-stream turbulence injected at the inlet boundary. As summarized in Table 6.1, the turbulence intensity levels obtained at the LE of the blade are in the range of 2.8-3.0%. As discussed in chapter 6, the evolution of the injected turbulence over the inlet region is characterized by a slower decay as well as a certain anisotropy present in the turbulence statistics. Thus, larger TI values than expected are obtained. This issue should nevertheless not have a dramatic impact in the context of the present study but is an element that should be kept in mind. The isentropic outlet Reynolds number considered across the different cases is of 70×10^3 hence corresponding to a quite low Re condition. The procedures to extract significant results in the form of complete flow fields as well as through the computation of the flow statistic are presented in section 5.5. The data acquisition is done in $21,000$, $18,000$ and $21,000$ iterations respectively for the three Mach number cases $M = 0.7$, 0.9 and 0.95 corresponding to approximately 5 axial convective times. During the discussion of the results, several comparisons are made with the numerical data obtained by Borbouse in [4]. In that study, the same flow configurations as developed in the present work were considered without turbulence injection and thus with a free-stream turbulence intensity of approximately 0%. Hence allowing us to discuss in detail the fundamental differences in the flow behaviour provoked by the presence of free-stream turbulence. Parallely, the experimental data collected by the VKI in [35] are used for comparison purposes. The experimental approach, briefly introduced in chapter 2, considers a wide range of Re and M with a free-stream turbulence of approximately 2.3%. In the following discussion, only the experimental configurations related to the numerically considered cases are taken into account. The results discussion is categorised into different sections depending on the flow features and regions. Firstly, the overall flow fields will be considered for the different cases in order to develop a first understanding of the flow. The observed flow phenomena will be highlighted and already briefly discussed. Next to the Mach number field also the vorticity, the entropy creation as well as the numerical Schlieren are presented. Each of the fields allows the observation of fundamentally distinct flow features. Secondly, the blade loading is investigated using the isentropic Mach number distribution around the blade. Then, in the continuity of the blade loading, the skin friction is studied in more detail. On the one hand, the average distributions around the blade and, on the other hand, the space-time graphs to analyse the temporal evolution and behaviour are considered. Fourthly, the boundary layer region is investigated. Next to the velocity profiles and fields in direct proximity to the blade surface, the BL integral parameters are analysed. Hereby, the complex separation and transition phenomena for the different Mach number cases will be understood in a further sense. Finally, the wake region is considered. After assessing the generated losses by studying the total pressure and temperature distributions in the wake, the flow deviation induced by the blade is quantified. Then the turbulent content of the wake is investigated. The wake behaviour is typically dictated by the vortex street phenomenon leading to a coherent vortex shedding, especially for the high Mach numbers. The turbulent activity related to this feature is studied with the Reynolds stress tensor, the integral length scales as well as the energy spectra.

7.1 Flow field

Firstly, the general flow field is investigated while the main flow phenomena will be highlighted. These discussions are done for the three considered flow configurations $M = 0.7$, 0.9 & 0.95 with a corresponding Reynolds number of 0.7×10^5. For this purpose, the instantaneous flow fields of the turbine passage are shown for typical physical quantities. Note that an instantaneous snapshot of the flow does not necessarily contain all the flow information and features related to the complex flow through the turbine cascade. Nevertheless, it is representative from a statistical point of view of the overall flow field and can be used to understand the physics of the flow. To better visualize the flow field in the turbine passage the pitchwise periodicity of the flow is exploited and several copies of the domain are placed next to each other.

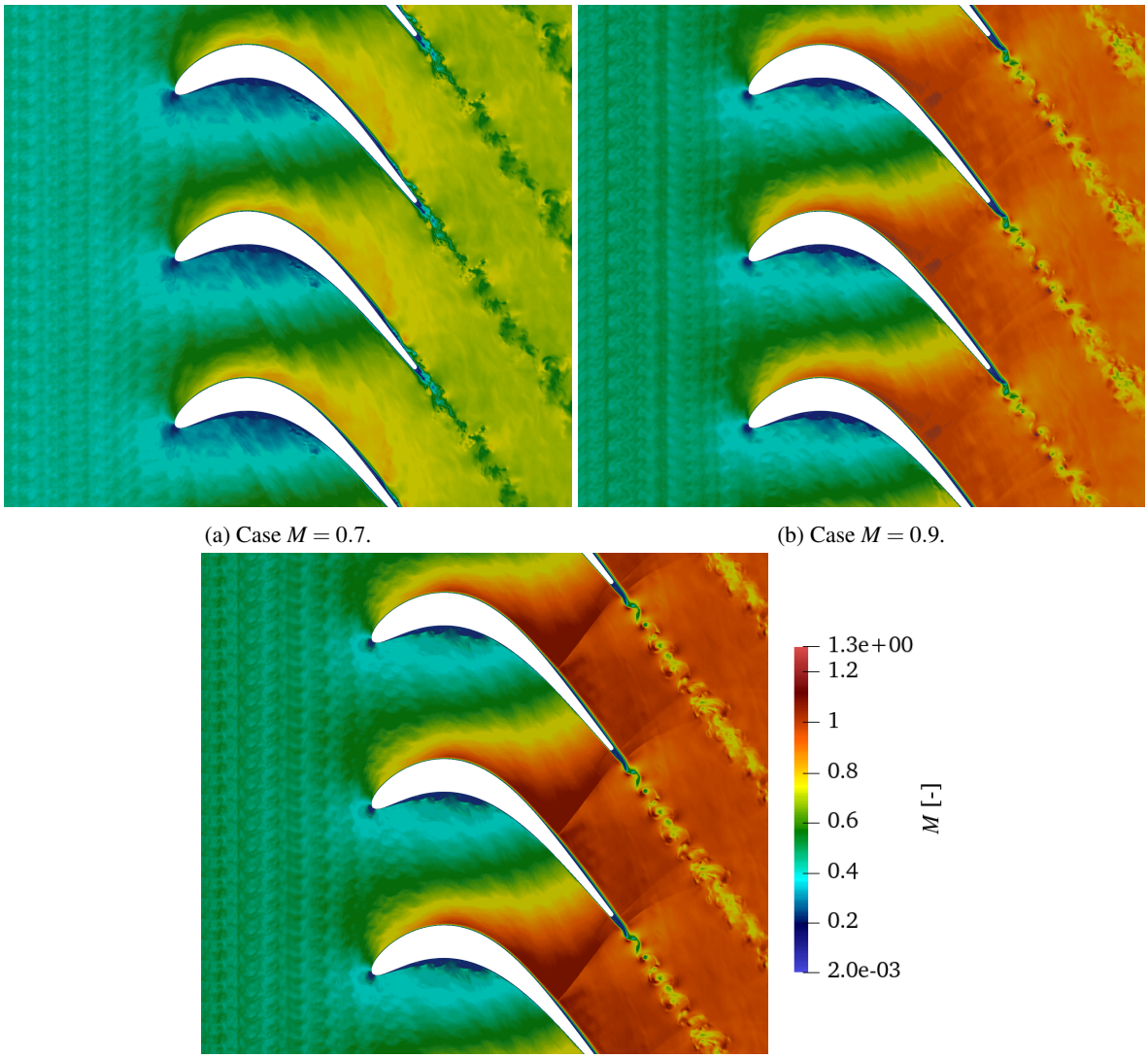

(a) Case $M = 0.7$.

(b) Case $M = 0.9$.

(c) Case $M = 0.95$.

Figure 7.1: Local Mach number M extracted instantaneously in the spanwise plane $z = 0$ m for the different considered cases. Note that several copies of the flow field are repeated in the periodic pitchwise direction for aesthetic reasons.

Figure 7.1 shows the Mach number in the flow passage for the different considered configurations. The injected free-stream turbulence is well-observable over the inlet region of the domain. Next to the striking pitchwise

coherence of the structures, the turbulent fluctuations are characterized by a TI ranging between 2.8-3.0% depending on the case. In the flow passage as well as downstream of the blade, the turbulent structures are in turn elongated and deformed due to the experienced accelerations.

For each of the Mach numbers depicted in Figure 7.1, a small separation region seems to be present on the pressure side of the blade. Indeed, after a first strong acceleration, the flow experiences a strong adverse pressure gradient representing favourable conditions for separation to occur. Due to the local turbulent structures travelling downstream along the PS, one can deduce that the flow evolved to the turbulent regime. This transition is linked to interactions happening with the separation region and allowing, in a wider sense, the separation bubble to be rapidly closed. During this procedure, turbulent structures are continually ejected and then convected downstream towards the TE of the blade. There the flow experiences reacceleration such that the generated turbulent fluctuations seem to be attenuated. Concerning the suction side different phenomena can be observed among the studied cases. For the low Mach number, the boundary layer grows steadily from the LE towards the rear of the blade. At some point, a strong increase in BL thickness is observed which is linked to the separation of the flow. After a transition region, the boundary layer achieves to reattach to the surface through turbulent mechanisms. This phenomenon is enhanced by the presence of free-stream turbulence increasing the perturbation level in the flow and thus the proneness of the BL to transition. The thickness of the now turbulent boundary layer appears to be strongly reduced over the last part of the SS. Indeed, the velocity profiles of turbulent BL are typically fuller than the laminar ones due to increased momentum exchange. When considering the higher Mach number cases, similar behaviours can be observed between both configurations. Indeed, the boundary layer seems to develop steadily over the SS by steadily increasing its thickness through continuous momentum exchange. No turbulent activities can be observed during this evolution. An important feature interacting with the BL is a shock present in the flow passage. Especially for the highest Mach number case, the shock has a well-defined shape and is located towards the rear part of the suction side. In terms of Mach number, values up to $M = 1.3$ are reached in the supersonic region upstream of the shock. In the near-wall region at the SS, the shock seems to interact with the BL and induce a noticeable thickness growth. From its SS location, the shock reaches towards to TE of the neighbouring blade. Two lighter shocks can be observed in the continuity of the first shock on the other side of the wake region at the TE. These two shocks originating from a downstream TE location reach into the wake of the neighbouring blade potentially interacting with it. For the moderate Mach number case, similar observations can be made. Mach numbers ranging up to 1.1 are noticed in the flow field such that several shocks are formed as well but in a reduced manner. The first shock which can barely be seen has a typical 'v' shape and is associated with a more upstream position on the SS compared to the $M = 0.95$ case. The shock seems to again affect the BL since a slight thickness increase can be observed downstream of its location. The two smaller shocks, forming the continuity with the first shock in the high Mach number case, are located far more upstream at positions considerably before the TE. Note that for the low Mach number case, no sonic conditions are reached in the flow passage and the highest encountered Mach numbers provoked by the acceleration over the SS are of the order of 0.9. In this typically subsonic flow field, no shock appear in the passage. Note that for the high Mach numbers, the free-stream turbulence level of the flow does not seem to greatly affect the flow field except concerning the separation bubble on the PS of the blade.

Another region of interest in Figure 7.1 consists of the wake of the blade. For the low Mach number, a strongly disturbed vortex street can be seen. Due to the reattachment of the flow on the suction side, the base flow region downstream of the TE is the size of the TE itself. In the streamwise direction, this region is also reduced and the vortex shedding happens relatively early. As already mentioned, the vortical structures in the von Karman street are not well defined. This unsteadiness and instability is most probably linked to the incoming turbulent fluctuations from the PS and SS which are interfering with the vortex shedding phenomenon. Nevertheless, a coherent shedding pattern is observable. For $M = 0.9$, the base flow region is much wider and longer than for the low Mach number case. This behaviour is related to the BL on the SS which does not transit to turbulence thus not allowing a significant reattachment of the flow associated with fuller velocity profiles. Hence, the vortex shedding happens further downstream at the end of the base flow region. The vortex street is much cleaner in the present case and the evolution follows a more stable and coherent pattern. The highest Mach number case follows a close behaviour compared to the moderate Mach number configuration. The stagnation region in direct proximity to the TE seems to be of the same width but slightly longer than for $M = 0.9$. This may be linked to the tails of the shocks potentially interfering with the base flow on both sides. Due to these possible interactions with an elongated base flow region, the overall vortex shedding process may be impacted leading to much cleaner and stable successive ejections of vortices. An effect of the shocks could consist in blocking perturbations travelling

upstream thus potentially interfering with the base flow and the boundary layer on the suction side. Due to the less important shocks and their more upstream positions, these blockage phenomena would be less present in the moderate Mach number case, thus supporting the observed differences and corresponding explanations. For the low Mach number case, this phenomenon could also be of great importance since perturbations typically of acoustic nature can travel upstream and accelerate the flow transition. Note that the coherence of the von Karman vortex street is also related to its fundamental stability dictated by the flow conditions and the geometric specifications (see subsection 3.4.1).

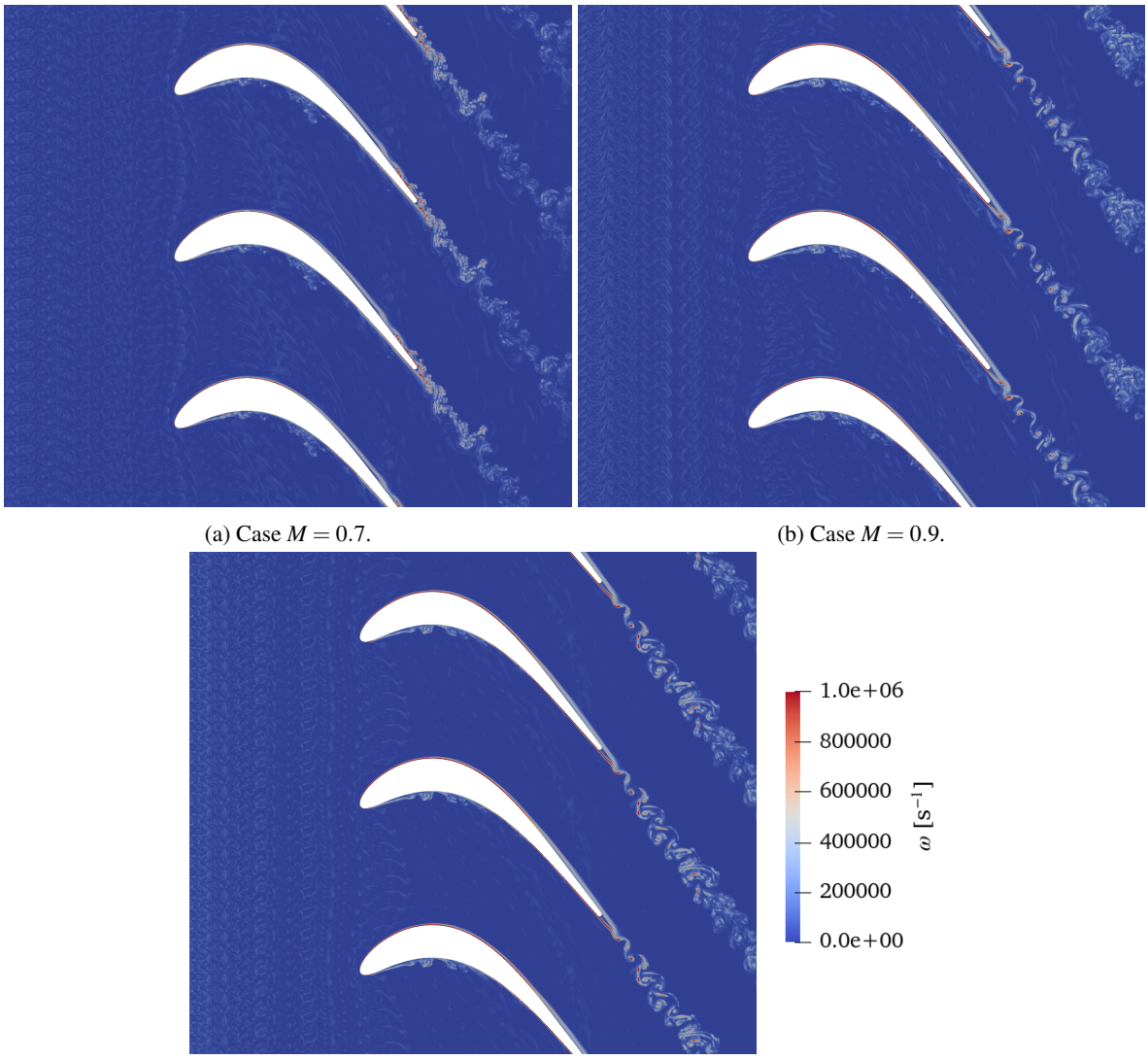

(a) Case $M = 0.7$.

(b) Case $M = 0.9$.

(c) Case $M = 0.95$.

Figure 7.2: Vorticity magnitude ω extracted instantaneously in the spanwise plane $z = 0$ m for the different considered cases. Note that several copies of the flow field are repeated in the periodic pitchwise direction for aesthetic reasons.

Figure 7.2 shows the instantaneous distribution of vorticity in the flow passage. The free-stream turbulence is associated with significant vorticity which continually decays when traveling downstream. However, the main vorticity regions are directly linked to two flow features: boundary layers and turbulent structures. Inside of the BL, large amounts of vorticity are generated as can be seen along the complete SS as well as the rear part of the PS. As discussed in section 3.3, the maximum production of vorticity is linked to the buffer layer while the

log layer also plays a considerable role. Along the rear part of the SS, the vorticity content is quite reduced for the high Mach number cases. This behaviour is typically linked to less pronounced velocity gradients close to the wall ascribed to the adverse PG, a synonym of flow deceleration. On the PS, the vorticity creation related to the separation can be noticed. Hence, the vorticity is generated by the free shear layer present between the main flow and the recirculation region. The turbulent structures on the other hand represent the other type of vorticity accumulations. Due to the separation of the flow on the PS, vortices associated with considerable vorticity are ejected from this flow region. For $M = 0.7$, a similar observation can be made on the rear part of the SS. Indeed, the turbulent behaviour of the flow leads to the presence of turbulent structures associated with high vorticity. Lastly, the wake region characterized by the vortex street is linked to large local vorticities. Especially the high Mach number cases with their stable vortex shedding exhibit coherent structures with important vorticity values.

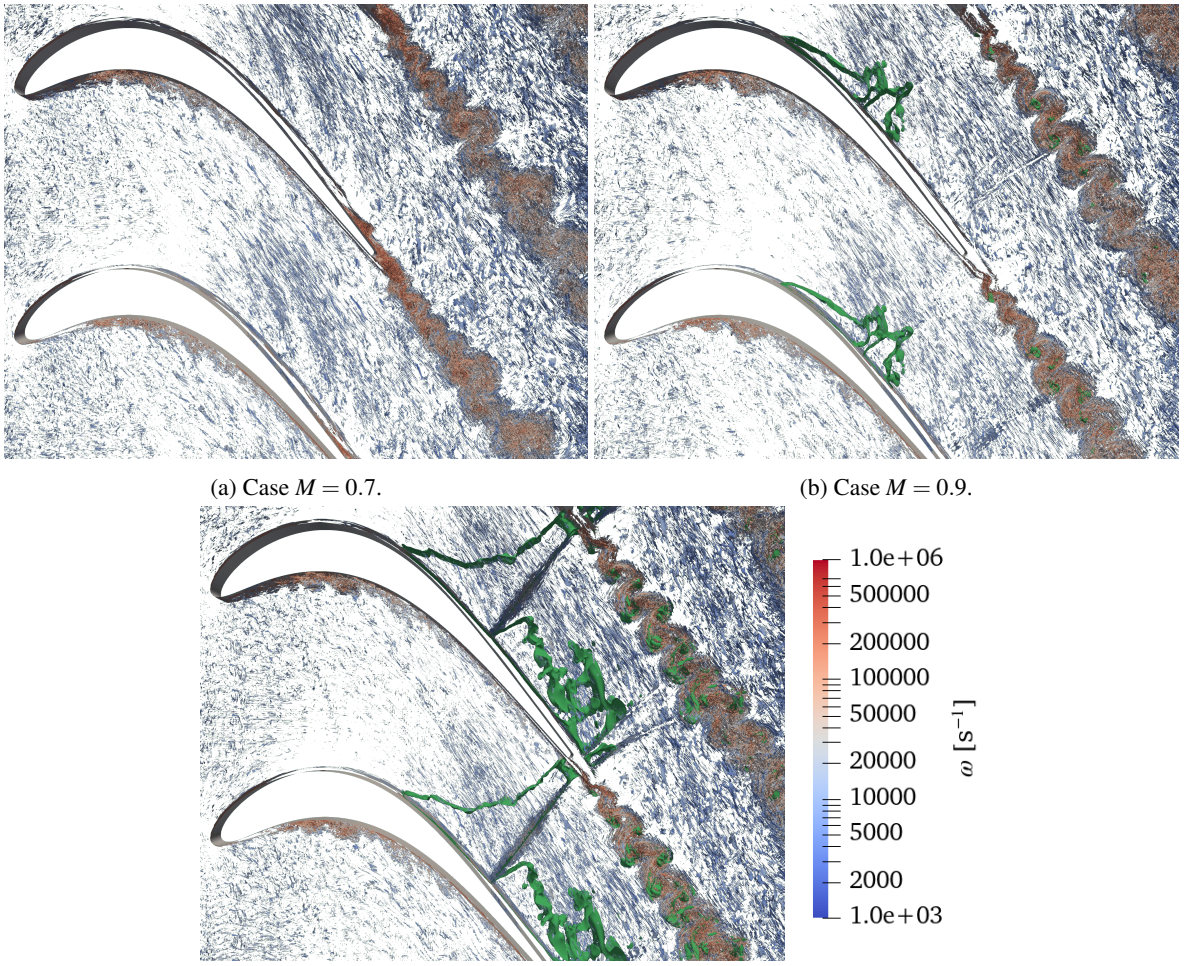

(a) Case $M = 0.7$.

(b) Case $M = 0.9$.

(c) Case $M = 0.95$.

Figure 7.3: Iso-surfaces of the Q-criterion in the complete domain with $Q = 1000$ and coloured by vorticity magnitude in logarithmic axis for the different considered cases. The iso-surface related to sonic flow conditions ($M = 1$) is illustrated in green. Note that several copies of the flow field are repeated in the periodic pitchwise direction for aesthetic reasons.

Closely related to the vorticity field shown in Figure 7.2, the three-dimensional properties of the turbulent flow structures can be investigated. Therefore, the Q-criterion coloured by vorticity is shown in Figure 7.3. The criterion is based on the difference between the symmetric and asymmetric parts of the velocity gradient tensor. On the one hand, positive values of Q are related to larger rotational rates while, on the other hand, negative values of Q are associated with larger shear rates. In our case, the Q-criterion is evaluated in the positive range and thus especially characterizes the vortical structures present in the flow. A striking feature is the strong elongation of

the free-stream turbulence structures in the rear part of the flow passage. Another observation can be made on the PS. There the turbulent regime of the flow which developed after the separation region can clearly be seen. This induced turbulent activity then travels downstream along the PS. The boundary layer over the SS does not manifest turbulent structures within itself. Indeed, the BL flow seems to stay laminar as well as attached all along the SS. An exception for this is the low Mach number case where significant turbulence is developed over the rear part of the SS after the separation and the following transition of the flow. The compressibility effects as shocks can also be seen in Figure 7.3. The sonic conditions which are intrinsically linked to the shocks themselves are illustrated by the green surface corresponding to $M = 1$. It can be observed that the shocks typically create clean aisles through the flow field by locally separating the turbulent structures. Also, small interactions between the shocks and the BL can be noticed. For the $M = 0.95$ case, it can be seen that the sonic condition spans the complete flow passage implying that this flow configuration corresponds to a choked passage. For the moderate Mach number case, on the other hand, the $M = 1$ curves do not cover the complete pitchwise flow section even though the shock seems to do so. For this configuration, the passage is thus not choked. Finally, the wake of the blade and thus the vortex street is composed of a large number of smaller-scale turbulent structures. Furthermore, it is associated with high vorticity as has been discussed previously.

In Figure 7.4 are shown the normalized density gradient fields for the different considered cases. The plot is made with a logarithmic scale such that a wide range of phenomena of different natures is illustrated. By doing so not only the strong density variations related to the turbulent structures and vortices are represented. The latter are typically present in the wake, in the separation regions of the BL and in a reduced extent in the injected free-stream turbulence. Indeed, also phenomena of reduced magnitude are considered using this approach such as acoustic waves. The acoustic perturbations are typically generated through the unsteady highly energetic behaviour of the wake. These perturbations then travel in the different spatial directions at an absolute velocity corresponding to the speed of sound a. If the flow is subsonic, the acoustic waves can not only travel downstream with the flow but also move upstream with a relative velocity $U - a$. This propagation phenomenon is illustrated particularly in low Mach number case. The acoustic perturbations originating from the wake saturate the free stream by steadily travelling upstream, especially along the suction side of the blade. Additionally, these waves are reflected on the blade surface as well as on large flow structures such that typical "V" intersections are formed by encountering waves. One can also observe that the LE of the blade reflects acoustic perturbations following the pattern of its geometrical shape. Both the upstream travelling acoustic waves and the LE reflections seem to rapidly attenuate in the flow such that no effect on boundaries or other implications should be induced.

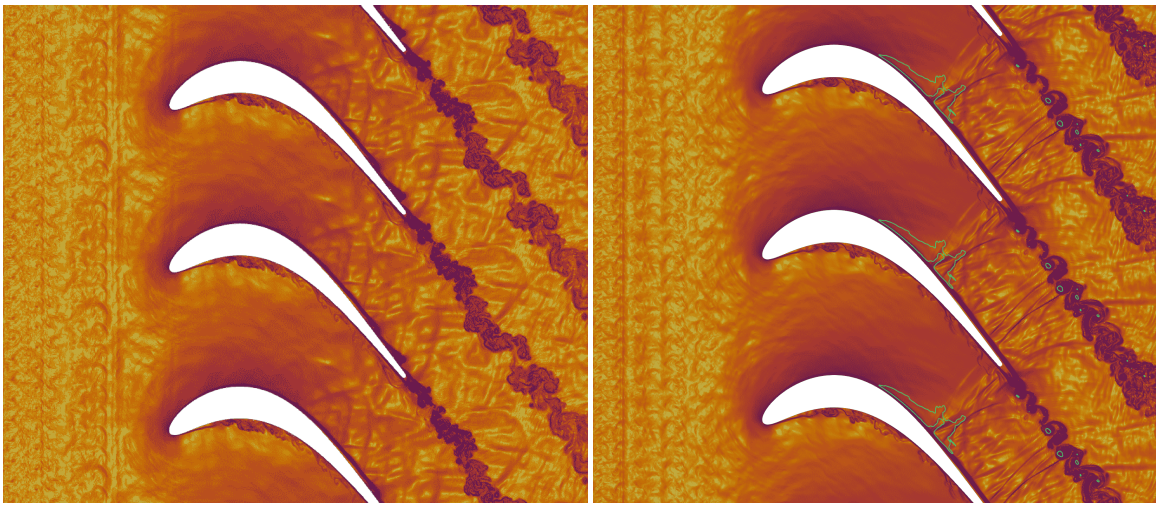

(a) Case $M = 0.7$. (b) Case $M = 0.9$.

Figure 7.4: Normalized density gradient $\nabla\rho/\rho$, also known as numerical Schlieren, extracted instantaneously in the spanwise plane $z = 0$ m for the different considered cases. The iso-curve related to sonic flow conditions ($M = 1$) is illustrated in green. Note that several copies of the flow field are repeated in the periodic pitchwise direction for aesthetic reasons.

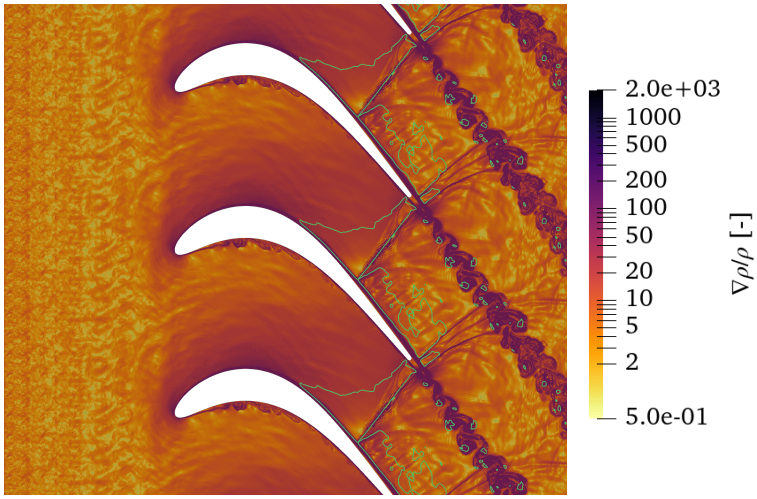

(c) Case $M = 0.95$.

Figure 7.4: Normalized density gradient $\nabla\rho/\rho$, also known as numerical Schlieren, extracted instantaneously in the spanwise plane $z = 0$ m for the different considered cases. The iso-curve related to sonic flow conditions ($M = 1$) is illustrated in green. Note that several copies of the flow field are repeated in the periodic pitchwise direction for aesthetic reasons.

For the high Mach number cases, the sonic conditions reached in the flow passage lead to fundamental differences in the flow field. As can be seen in Figure 7.4, the presence of a shock in between the blades blocks the upstream travelling acoustic information. Hence, the acoustic perturbations emitted from the wake region only saturate the downstream region with respect to the shock. This flow region is strongly characterized by the shock system as well as the numerous acoustic waves accompanied by their reflections. Thus, the upstream flow region to the shock remains free of these perturbations due to this blockage effect.

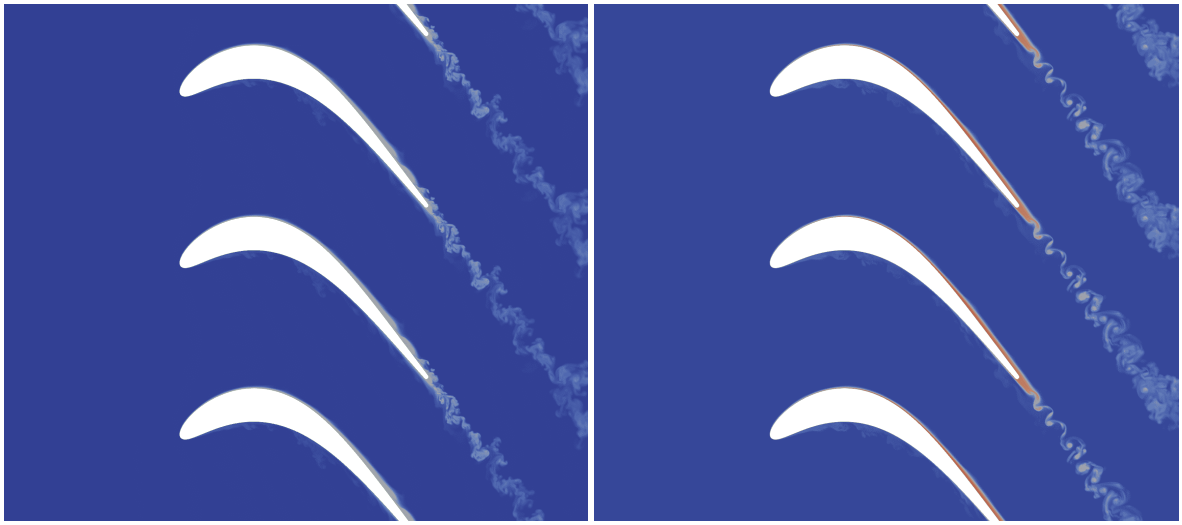

(a) Case $M = 0.7$. (b) Case $M = 0.9$.

Figure 7.5: Entropy generation Δs extracted instantaneously in the spanwise plane $z = 0$ m for the different considered cases. Note that several copies of the flow field are repeated in the periodic pitchwise direction for aesthetic reasons.

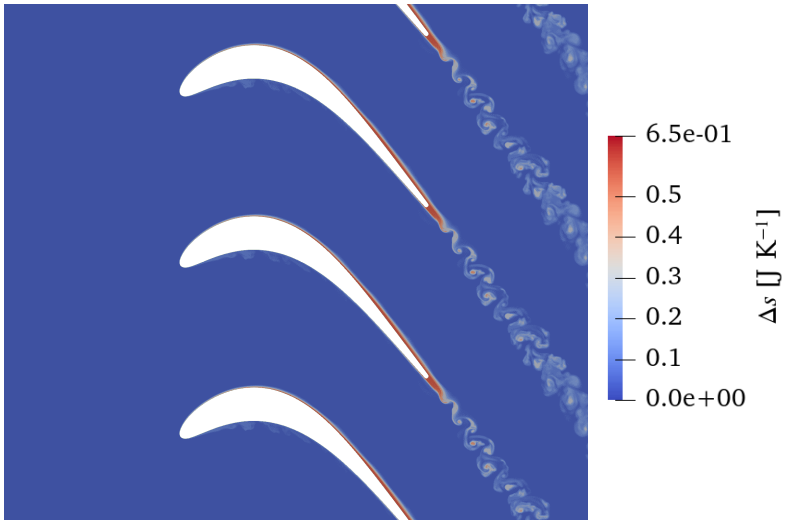

(c) Case $M = 0.95$.

Figure 7.5: Entropy generation Δs extracted instantaneously in the spanwise plane $z = 0$ m for the different considered cases. Note that several copies of the flow field are repeated in the periodic pitchwise direction for aesthetic reasons. (cont.)

Finally, the instantaneous entropy creation in the flow fields is shown by Figure 7.5. As discussed in subsection 3.1.3, the entropy generation indicates the losses in the flow field. It can be noticed that the magnitude of entropy difference increases with Mach number such that the $M = 0.95$ is associated with the highest losses. As developed in [10], an important contribution consists of entropy created in the boundary layer. Especially the BL on the SS of the blade gives rise to large entropy creation until reaching the TE. There, the stagnation region related to the base flow behind the TE is another region where a considerable amount of entropy is generated. A further contribution to the losses is played by the turbulent mixing processes. Indeed, the turbulent flow features developing on the PS or at the rear part of the SS for the low Mach number case are associated with significant entropy creations. In the same optic, the vortex shedding characterized by the periodic ejection of vortical structures is also a source of entropy as can be observed in Figure 7.5. The compressible effects such as the shocks observed at high Mach numbers do not give birth to major entropy creations as opposed to what could be expected.

7.2 Blade loading

The aerodynamic loading acting on the blade can be studied by using the isentropic Mach number distribution around the blade (see Equation (3.7)). Its extracted temporal and spanwise average is shown in Figure 7.6 where the three considered cases are compared with their respective counterparts in terms of experimental approach and numerical approach without free stream turbulence. The M_{is} distribution is given with respect to the normalized streamwise coordinate such that the lower curve is associated with the pressure side and the upper curve to the suction side.

As can be observed in Figure 7.6, the blade loading along the suction side is very similar between the different approaches for the high Mach number cases. Especially both numerical approaches match very well while the experimental measurements are slightly shifted upwards over the complete SS. The small difference can most probably be led back to a slight difference in the actual Mach number present leading to this vertical shift. For the low Mach number case, the effect of free-stream turbulence is more apparent. On the one hand, the overall distribution matches way better the experimental curve while the clean case has a significantly lower blade loading due to its laminar separation region reaching the TE and impacting the upstream pressure distribution. On the other hand, the pressure recovery phenomenon towards the end of the SS is captured with turbulence

injection. The latter consists of the reattachment of the flow by transition but is however occurring earlier than in the experimental approach. The discrepancy can be related to the slightly higher turbulence level present numerically with respect to the experimental setup. This typically leads to a more rapid transition phenomenon and consequently to a larger pressure recovery region. Over the pressure side, interesting observations can be made related to the first part where the flow is typically subjected to large adverse pressure gradients and is characterized by the transition to turbulence. Indeed, the plateau observed in the numerical approach without free stream turbulence related to a considerable separation bubble is strongly reduced when injecting turbulence. Hence, the experimental measurements compare well with the simulation results obtained in the present study. Both approaches predict no or a very reduced laminar separation with a flow characterized by its turbulent content and mixing allowing it to stay attached or rapidly reattach to the surface by increased momentum exchange. The presence of free-stream turbulence allows to boost the transition of the flow by introducing turbulent spots generated through the interaction with the boundary layer. Nevertheless, as already observed over the suction side, a noticeable shift can be seen with respect to the experimental blade loading. In terms of varying Mach numbers, the velocity peak at the blade level typically shifts backwards, towards the rear of the blade, for higher M [2]. This is well in line with what can be observed since the maxima of the isentropic Mach number, related to the lowest pressure values, move towards the TE for increasing Mach numbers. An induced effect is that the deceleration of the flow occurs later such that the region over which an adverse pressure gradient acts is reduced as well. Nevertheless, the associated pressure gradients are usually locally stronger for the high Mach number cases even though the region where they apply is reduced. A direct implication of this feature is that the pressure recovery between the suction peak and the TE is typically smaller for higher Mach numbers. Another indirect effect of the Mach number is linked to the free stream turbulence. The latter gain in importance at lower Mach numbers [40]. Especially for the $M = 0.7$ case, the induced effects can clearly be observed over the SS and PS, while its effects are reduced for the higher Mach numbers.

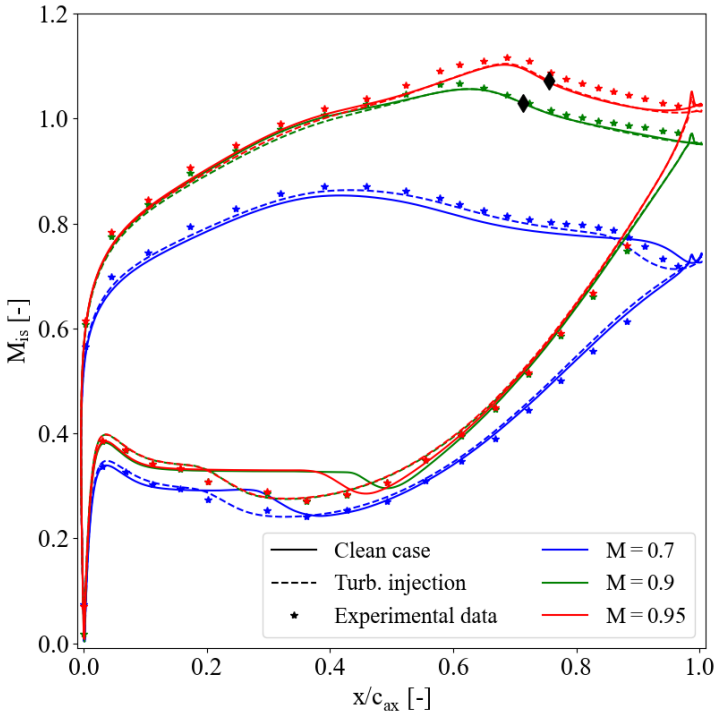

Figure 7.6: Isentropic Mach number distribution around the blade for the different considered cases. The configurations with turbulence injection are presented and the numerical data related to the setup without free stream turbulence [4] as well as the experimental data [35] are included for comparison. The black rhombuses are characterizing the average shock location.

7.3 Skin friction

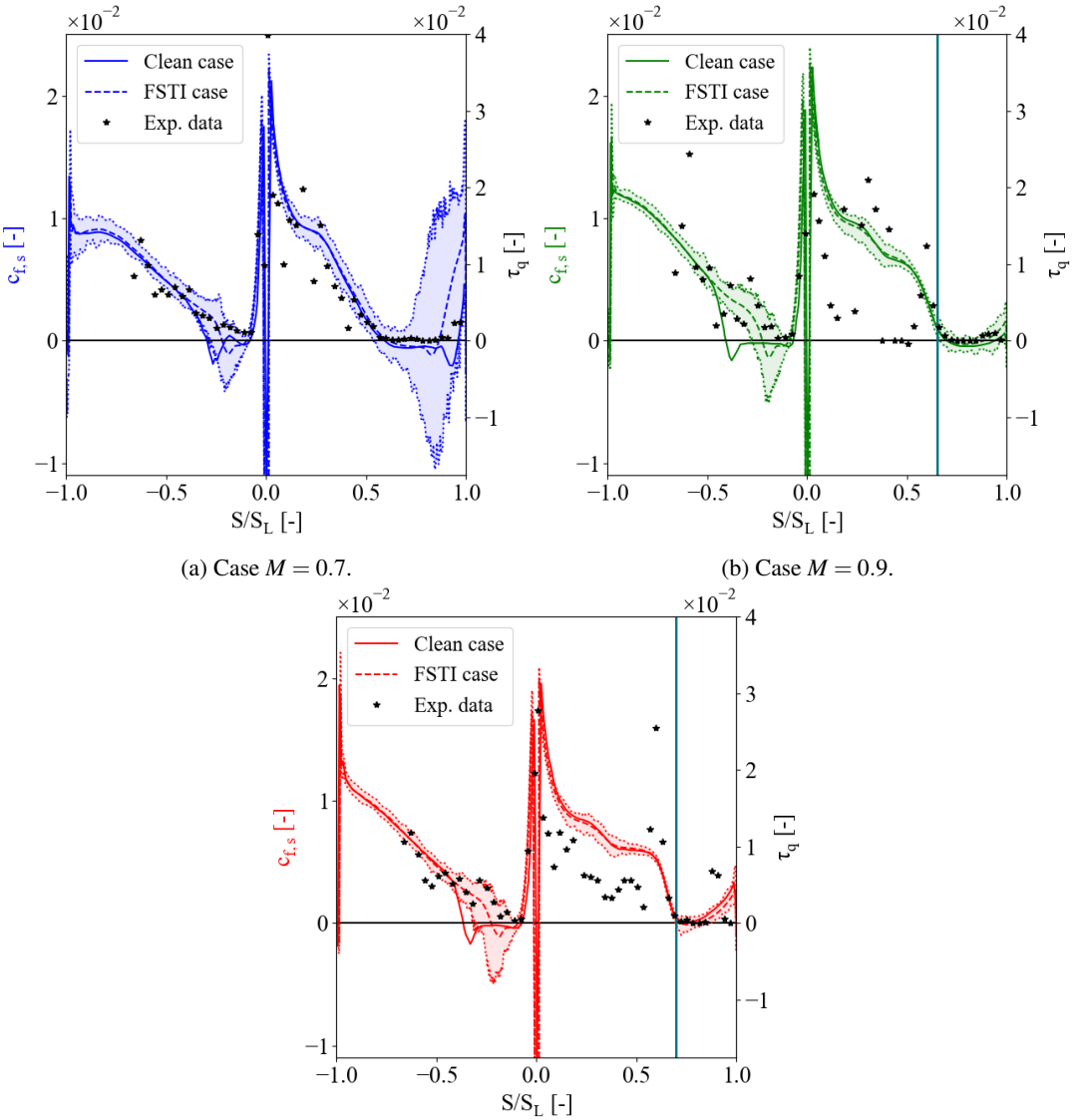

(a) Case $M = 0.7$.

(b) Case $M = 0.9$.

(c) Case $M = 0.95$.

Figure 7.7: Time and spanwise average of the skin friction coefficient distribution around the blade for the different considered cases. The configurations with turbulence injection are presented and the numerical data related to the setup without free stream turbulence [4] as well as the experimental data [35] are included for comparison. The experimental quantities represent the quasi-wall-shear stress measured on the blade. The average shock location is marked by the vertical line.

In order to start the discussion of the phenomena happening close to the blade surface and thus related to the boundary layer, a closer look is taken at the skin friction distribution. The latter is investigated by considering the skin-friction coefficient (see Equation (3.9)) which is an non-dimensionalized form of the wall shear stress τ_w. In Figure 7.7 are shown the temporal and spanwise averaged skin-friction coefficient ($c_{f,s}$) distributions over the blades SS and PS for the three considered Mach number cases. Additionally, the results from [4] obtained for the clean numerical case are illustrated. The experimental measurements in terms of quasi-wall shear stress are included as well but are plotted along a separate axis. Indeed, their absolute values are not the important aspect here but way more their relative variations. Therefore, a resize of the axes is made to adequately present both types of results with respect to each other. For the present study, the respective fluctuations are illustrated by showing the maximum and minimum values taken at each blade location thus giving a brief idea of the unsteadi-

ness and deviations of the measured skin friction. Note that the distributions are presented using the curvilinear coordinates of the blade such that the positive values correspond to the SS, the negative ones to the PS and the 0 to the LE of the blade. As discussed in subsection 3.3.1, zero skin-friction values are typically associated with separation or reattachment points.

As can be seen in Figure 7.7, the behaviours between the different cases and approaches are similar. Over the suction side, a very large $c_{\mathrm{f,s}}$ is observed close to the LE which then decreases continually by passing through several inflexion points. This decay continues until reaching values close to zero, typically associated with separation, where the values stabilize before growing again till the TE of the blade. For the low Mach number case, the decrease occurs earlier due to its sooner velocity peak over the SS. Then, a considerable separation region can be spotted whose size has been reduced through the presence of injected turbulence thus better matching the experimental measurements. The separation region which is characterized by the onset of turbulence is associated with large fluctuations in terms of $c_{\mathrm{f,s}}$. After reattaching the flow, the skin friction experiences a strong increase which overcomes the experimental predictions. This observation is most probably linked to the earlier onset of transition and the sooner reattachment of the flow linked to a slightly higher free stream turbulence level with respect to the experimental approach. The higher Mach number cases demonstrate a quite similar evolution. Due to the later velocity peak, the decrease of skin-friction coefficient is retarded thus occurring later but with a much steeper slope because of the larger adverse pressure gradient experienced. Then in both cases, small separation regions can be observed which are located further downstream for increasing Mach numbers. The separation bubble is quickly reattached to the surface, especially for the highest M, before the $c_{\mathrm{f,s}}$ increases again. Note that for the $M = 0.95$ case without free-stream turbulence no separation has been observed on average. In this context of separation, the presence of the shock may play a fundamental role. The fluctuations associated with the high Mach number cases are minimal inducing the presence of a quasi-laminar flow with a slight onset of transition in the blades BL. These observations at high M are the consequence of a smaller region dictated by an APG, the shock effects as well as the clear reduction in the effect of the free-stream turbulence. The experimental measurements related to the first part of the SS are strongly oscillating especially for the $M = 0.9$ case. Hence, no clear observation can be deduced even though the trend seems to be common among the approaches. Over the rear part of the SS, a much better match between experiments and numerical approach specifically with turbulence injection is achieved. Additionally, two outliers in the experimental data can be seen close to the numerically determined shock location for both high M. These points should correspond to the experimental shock position.

Concerning the PS, the behaviour is characterized by very high initial skin friction which quickly decreases towards negative values until experiencing laminar separation of the flow followed by a more or less rapid reattachment by transition of the flow. Afterwards, the skin friction increases steadily through the presence of a favourable pressure gradient, a synonym of a reacceleration of the flow. In this context, relaminarization can even be achieved before reaching the TE if the acceleration is consequent enough. With respect to the clean numerical simulation, a considerable reduction in the separation region size can be seen. This behaviour matches the observation made experimentally. Next to that large fluctuations are present in the region associated with the separation and thus the transition to turbulence of the flow. These fluctuations typically become smaller when advancing to the rear end of the PS due to the negative pressure gradient effect.

In Figure 7.8 are shown the space-time diagrams describing the temporal evolution of the spanwise averaged skin-friction coefficient distribution around the blade. Note that an evolution over a time span of 10^{-3}s is considered and that the locations where zero values are reached are visualized by black lines. It can be observed in an alternative way what has been discussed in Figure 7.7. For the low Mach number case, the strong fluctuations observed towards the end of the suction side can be linked to the illustrated oscillatory separation and reattachment behaviour. At any time step, the flow achieves to close the bubble before the TE thus preventing open separation regions which provoke high losses and reduced performances. The fluctuating behaviour can be related to periodic bubble bursting with reattachment before the TE. The region just behind the separation bubble is highly blurred which can be related to the turbulent state of the flow. This turbulence developed upstream due to the separation of the flow and more precisely in the free shear layer. In [4] without the external effect of the free-stream turbulence, the BL did not systematically achieve to reattach before the TE. On the PS, the laminar separation and the rapid reattachment by flow transitioning can be seen. The reattachment location seems also to move in a fluctuating manner. Overall, the skin-friction behaviour on the PS is very similar among all the Mach number cases. Nevertheless at the SS, some differences can be observed for the high Mach number configurations. As discussed previously based on Figure 7.7, the evolution of $c_{f,s}$ is first characterized by a slow decrease

before a steep decay occurs. The separation bubble formed just behind the shock location is very reduced for $M = 0.95$ such that at some point no separation is present at all along the blade. For the moderate Mach number, the separation region is more considerable but is closed ore than quickly enough to prevent open separations. For these higher M cases, the location of the separation is more constant while for the low Mach number, the position fluctuates significantly. The distribution of $c_{f,s}$ appears to be very smooth after the small separation bubble on the suction side thus supporting the idea of a quasi-laminar flow stacked with local turbulent perturbations linked to the transition phenomena. Additionally, blurred lines can be observed in the skin friction field on the upstream part of the SS. These lines correspond to vortices and turbulent structures belonging to the free stream which achieve to interact with the boundary layer of the blade. The induced fluctuations are then convected downstream with the BL forming these blurred lines. A similar phenomenon can be observed along the rear part of the PS. In this case, the turbulent structures do not belong to the free stream but are vortices generated and ejected by the separation region on the PS. The structures are then convected downstream by drawing these lines into the evolution of $c_{f,s}$. For the low Mach number case, some blurred lines can be seen that possess a slope perpendicular to the ones discussed previously. Indeed, the subsonic regime allows information and especially acoustic perturbations to travel upstream and generate these kinds of lines. For the high Mach numbers, the presence of the shock blocks all the information such that nothing can travel upstream and no such lines are observable.

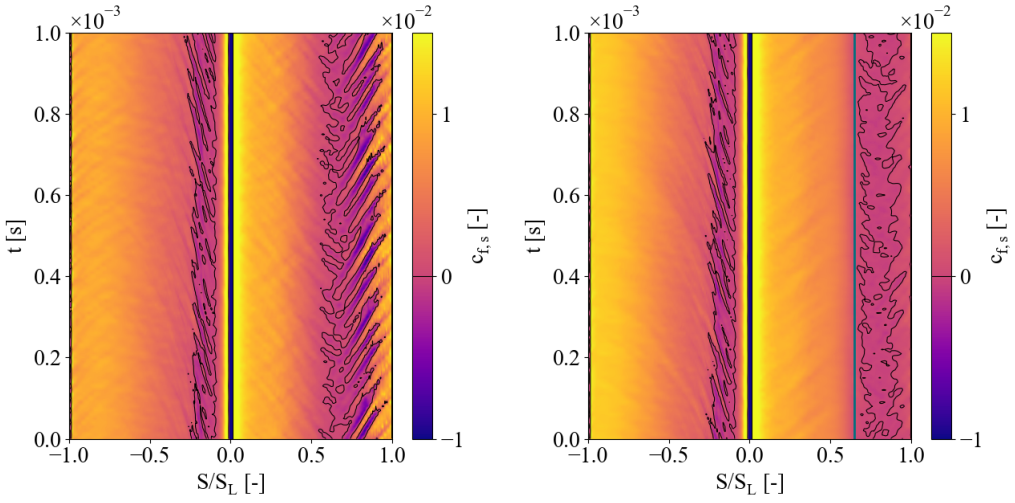

(a) Case $M = 0.7$.

(b) Case $M = 0.9$.

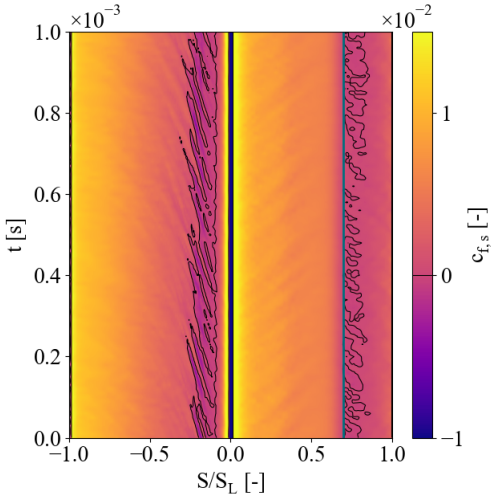

(c) Case $M = 0.95$.

Figure 7.8: Space-time graph of the temporal evolution of the spanwise averaged skin friction coefficient distribution around the blade for the different considered cases. Note that only the configurations with turbulence injection are presented. The average shock location is marked by the vertical line.

7.4 Boundary layer

In this section, the focus is laid on the near-wall flow phenomena occurring in the boundary layer. Before analysing the boundary layer integral parameters, a closer look at the profiles and distributions at the blade level is taken. Thus, in the first approach, the temporal and spanwise averaged velocity field around the blade as well as the corresponding turbulent fluctuations are investigated. Therefore, a selected set of velocity profiles, the velocity field as well as the TKE field are shown in Figure 7.9, Figure 7.10 and Figure 7.11 for the different Mach numbers considered. Note that the quantities presented are all normalized for the isentropic outlet velocity. Furthermore, the information contained in the velocity profiles and the velocity field visualizations is fundamentally the same being based on the local tangential velocity defined with respect to the blade surface. Nevertheless, both ways of presentation allow to put forward different flow characteristics. It is important to note that the BL measurements do not span the complete contour of the blade. Indeed, the data is based on the probe set introduced in section 5.5 which is composed of a finite ensemble of probe rakes specifically distributed around the blade. In terms of axes, the abscissa is represented by the normalized blade curvilinear coordinates where PS and SS are respectively associated with negative and positive values. The vertical axis is described by the local normal distance to the blade surface.

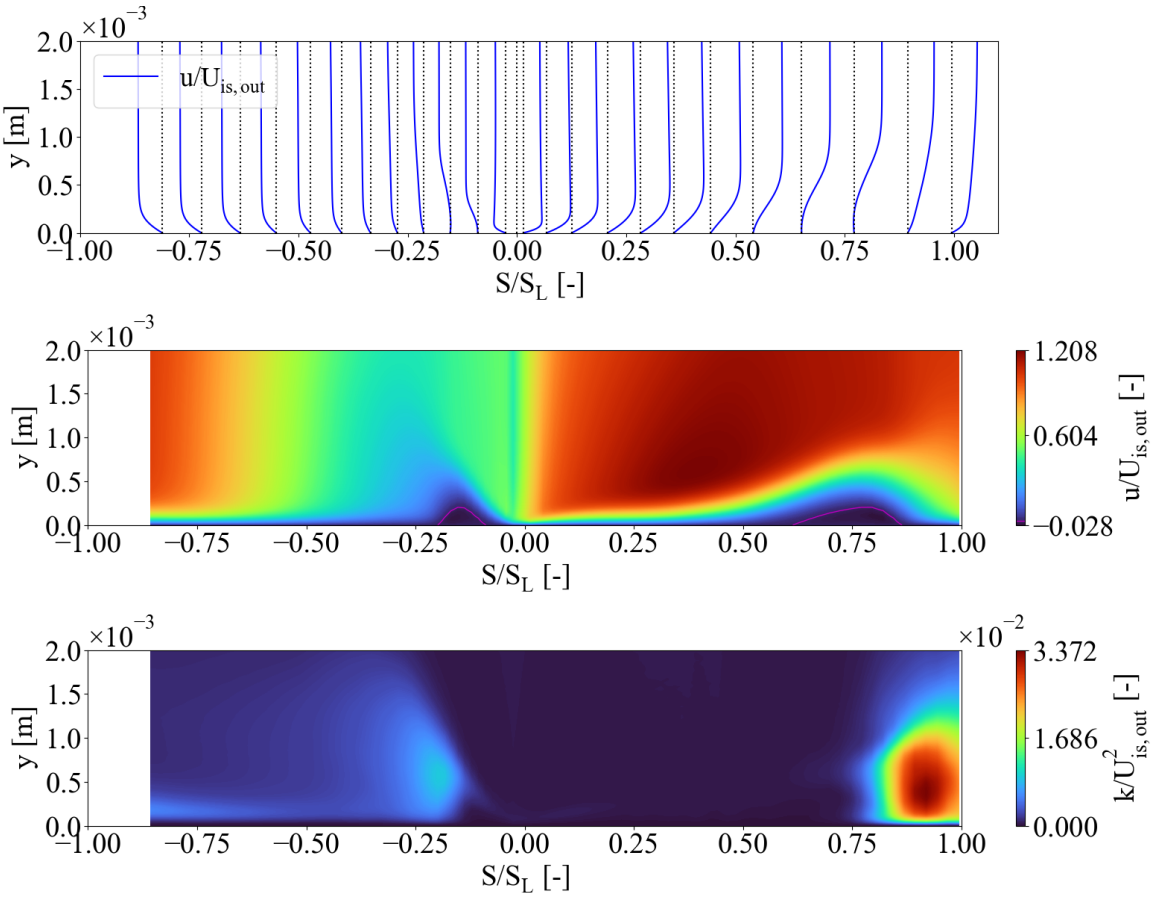

Figure 7.9: Temporal and spanwise average of the velocity distribution and its turbulent fluctuations associated with the BL around the blade surface. The distribution of normalized velocity profiles **(top)**, the normalized velocity field **(centre)** and the normalized TKE field **(bottom)** are shown for the $M = 0.7$ case.

For the low Mach number case shown in Figure 7.9, the velocity distribution seems to be well in line with the observations made in the previous sections. On the pressure side, a significant laminar separation bubble is present after a brief acceleration of the flow. This bubble can be noticed in the velocity profiles where an inflexion point appears and negative velocities are then observed on average linked to the recirculation of the flow. In the velocity field, the contour line of zero tangential velocity is highlighted in magenta. This line approximates in a wider sense the separation region. Indeed, a zero parallel velocity is encountered at the precise separation and

reattachment points of the separation bubble. However, the curve joining these two points does not correspond to the average contour of the bubble. It describes a kind of median line contained inside of the bubble for which the tangential velocity cancels while the normal velocity component may be non-zero. Thus, the drawn curves do not correspond to the exact bubble geometry but are nevertheless representative of the bubble shape and size. After separation, the flow is able to rapidly reattach to the surface as is illustrated by the velocity distribution. The reattachment of the flow happens by the transition of the flow such that an increased TKE level can be observed following the separation. As can be seen, the turbulence is first generated in the free shear layer of the separation bubble before the turbulent fluctuations develop in the complete region. The TKE then seems to decay slowly while a steady acceleration of the flow can be observed in the velocity profiles when advancing towards the TE of the PS. The observed laminar separation followed by reattachment through transition mechanisms is well in line with the concepts discussed by Mayle in [39]. On the SS, a significant acceleration is observed along the front part until the emergence of the adverse PG which leads to the appearance of an inflexion point in the velocity profiles. Then, a considerable laminar separation region is experienced whose shape is approximated by the curve in the tangential velocity field. The average separation point is located at $S/S_L = 0.614$. By shear layer interaction, transition onsets until turbulence develops, as can be seen in the TKE field. Hereby, the flow is able to reattach and the bubble can be closed. As illustrated in the velocity field, the first part of the bubble is elongated due to the presence of a moderate adverse PG. The rear part of the bubble has a shorter length describing a rapid reattachment provoked through transition after having passed the location of maximum displacement of the main flow. A region of high Reynolds stresses is generated downstream of the separation bubble as a result of the onset of the turbulent flow regime. Due to the increased momentum exchange, the velocity profile develops again towards fuller distributions at this point. The typical separation bubble shape and behaviour observed on the SS corresponds to the laminar long bubble mode introduced by Hatman and Wang in [24].

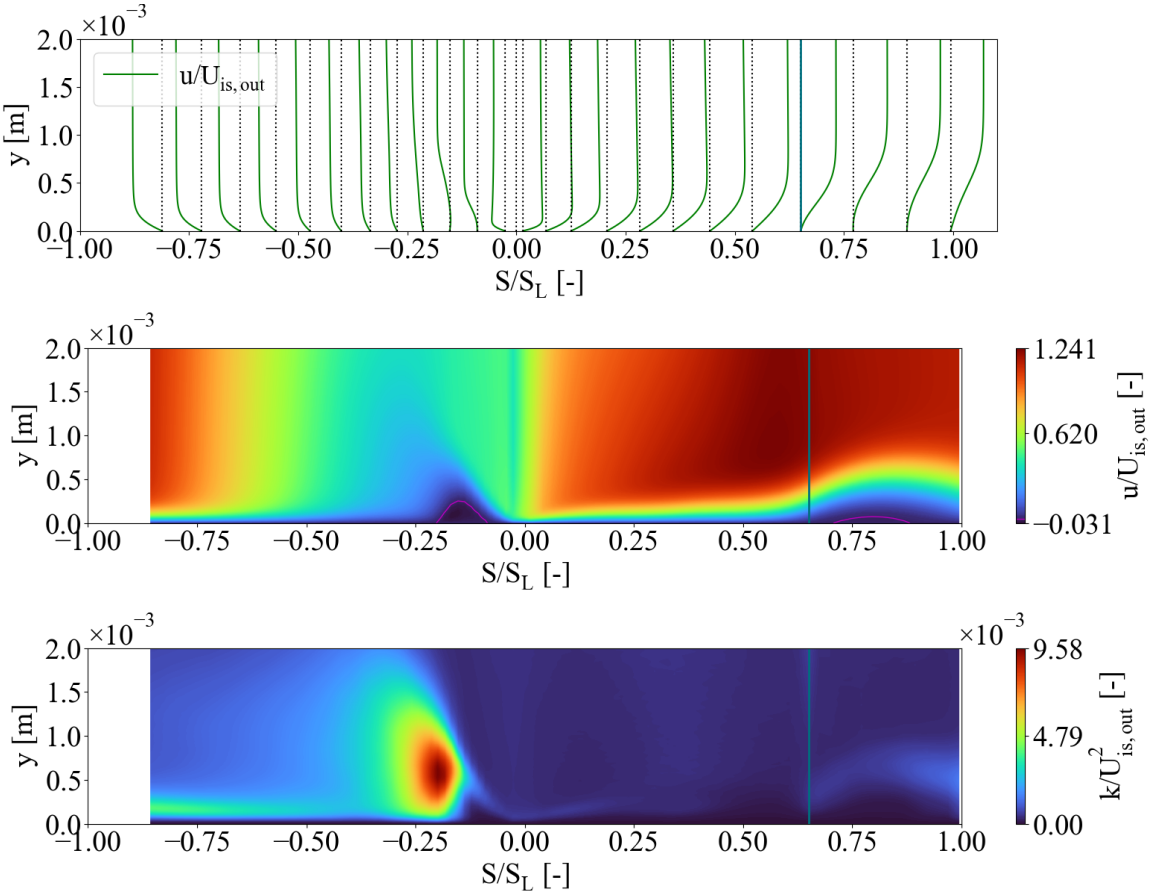

Figure 7.10: Temporal and spanwise average of the velocity distribution and its turbulent fluctuations associated with the BL around the blade surface. The distribution of normalized velocity profiles **(top)**, the normalized velocity field **(centre)** and the normalized TKE field **(bottom)** are shown for the $M = 0.9$ case.

Figure 7.10 shows the distributions within the boundary layer of the blade for the moderate Mach number case. Note that for the higher Mach numbers, the average shock position is illustrated by a line. On the one hand, the observations made about the BL evolution on the PS for $M = 0.7$ are applicable in the considered case since the profiles and fields follow the very same pattern. On the other hand, the flow over the suction side presents some fundamental differences. Again an initial acceleration of the flow near the wall is observed in the velocity profiles before the appearance of an inflexion point due to the adverse pressure gradient. Then, the shock located approximately around $S/S_L = 0.65$ will interact with the BL and thus affect the separation and transition phenomena. Indeed, a small recirculation region can be seen downstream of the shock in the velocity field. This behaviour can be related to the topics discussed in subsection 3.3.3 for BL-shock interactions. The presence of the shock leads to a fundamental change in flow properties which also impacts the pressure within the flow. The pressure experiences a considerable increase through the shock leading to an increased adverse pressure gradient provoking a premature separation of the flow at $S/S_L = 0.707$. Due to a pressure recovery effect, the flow then reattaches smoothly to the surface. As can be seen in the velocity profiles after the separation thus close to the TE, the velocity distributions fill up again but an inflexion point still exists due to the presence of a moderate adverse PG. In the TKE field, one can observe that the onset of transition was made parallel to the separation of the flow such that turbulent activity slowly developed within the free shear layer of the bubble. The turbulent fluctuations then steadily increase but do not reach a fully turbulent pattern until the blade TE. One can thus deduce that the BL close to the TE corresponds to an attached quasi-laminar flow which is characterized by an, in the wall-normal direction, elongated low-velocity region close to the surface. Nevertheless, the transition is in progress such that local turbulent perturbations start to affect the BL flow by steadily increasing in turbulent magnitude. The behaviour observed of the occurring shock-BL interaction is well in line with the concepts and phenomena discussed by Sabnis in [51].

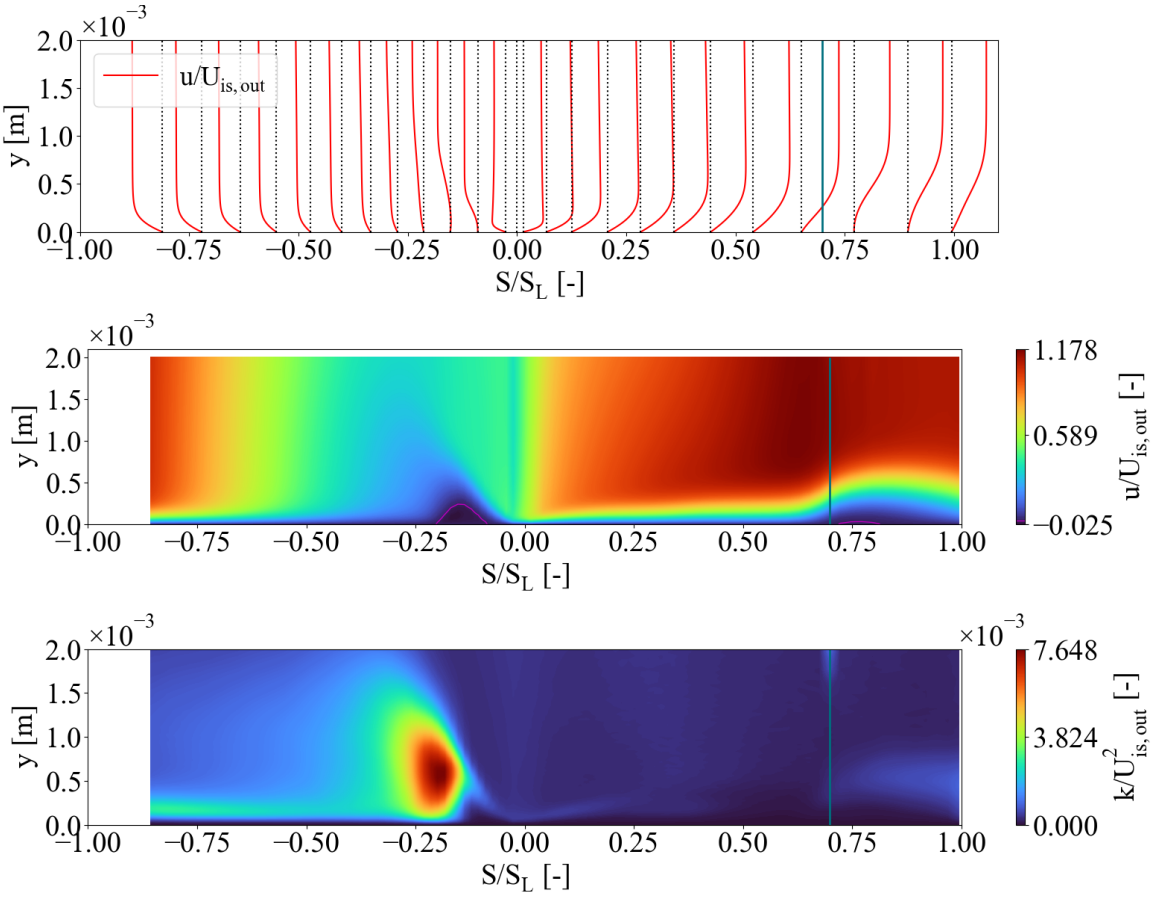

Figure 7.11: Temporal and spanwise average of the tangential velocity distribution and its turbulent fluctuations associated with the BL around the blade surface. The distribution of normalized tangential velocity profiles **(top)**, the normalized tangential velocity field **(centre)** and the normalized TKE field **(bottom)** are shown for the $M = 0.95$ case.

The velocity and turbulent fluctuation distributions for the $M = 0.95$ case are shown in Figure 7.11. The overall flow behaviour is very similar to the moderate Mach number configuration described previously. The BL evolution on the PS is thus comparable for the three Mach number configurations, all characterized by the same flow features. However, on the suction side, some differences can be highlighted with respect to the $M = 0.9$ case. The shock location slightly moved downstream such that it is now located around $S/S_L = 0.7$. Also, the size of the separation bubble is considerably smaller while the separation point slightly moved downstream at $S/S_L = 0.718$. The reduced extent of the recirculation region can be led back to the higher Mach number reached in the passage and thus the more powerful shock developed. The presence of a stronger shock leads to a more important abrupt change in the flow field as well as an increased pressure recovery phenomenon afterwards. Thanks to this pressure recovery following the shock compression, the flow rapidly achieves to reattach. Then the elongated quasi-laminar BL steadily develops a fuller profile as can be seen in Figure 7.11. The profile still contains the inflexion point related to the presence of the adverse PG. As for the moderate Mach number, the turbulent fluctuations slowly emerge due to the separation region followed by a continual growth of the turbulent activity. The latter is however only present in a reduced manner since the flow is in the early phase of transition and not in a fully developed turbulent regime.

In the continuity of the previous discussions, the BL integral parameters can be considered. Figure 7.12 shows their temporal and spanwise average along the blade for the three studied configurations. More precisely, the displacement thickness δ^*, the momentum thickness ω and the shape factor H are illustrated on respective axes.

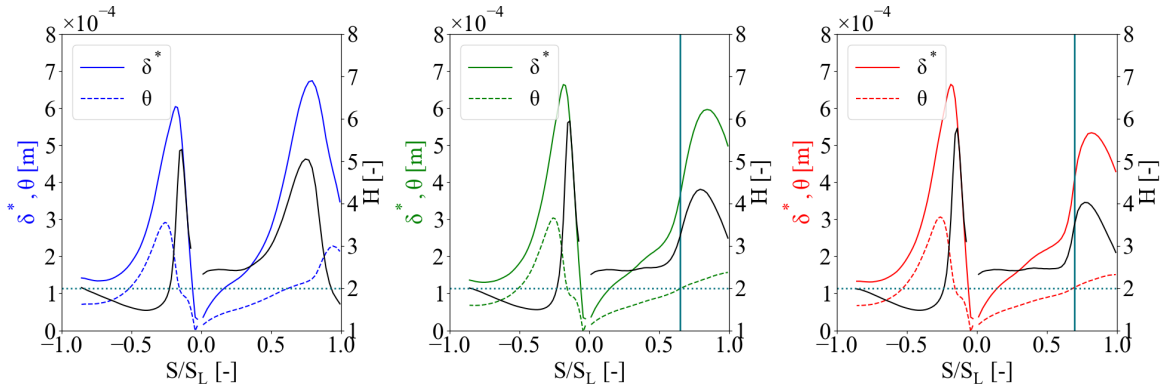

(a) Case $M = 0.7$. (b) Case $M = 0.9$. (c) Case $M = 0.95$.

Figure 7.12: Time average of the boundary layer integral parameters for the different considered cases. The displacement thickness δ^*, the momentum thickness θ and the shape factor H are presented on respective axes. Note that only the configurations with turbulence injection are presented.

Along the PS of Figure 7.12, the evolutions of the curves are very similar among the different cases. This behaviour is well in line with the previous discussions where quasi-the-same separation, transition and acceleration phenomena were observed on the PS. Indeed, the displacement thickness grows significantly over the beginning of the PS due to the early separation region. Parallely, the momentum thickness grows slowly with the laminar separation region during a first phase. θ then experiences a large increase in a second phase simultaneous to the maximum of δ^* as well as its following decay. This behaviour relates to the transition of the flow to turbulence. Initially, the laminar separation leads to a strong deviation of the flow combined with a comparably small momentum exchange. By transition of the flow, the turbulent content of the flow provokes an increased momentum exchange allowing the reattachment of the flow to the surface. The closure of the bubble then leads to the decrease of both θ and δ^*. The shape factor is first slightly increasing in the laminar range (above 2) before following a strong decrease. In the region of strongly increased momentum thickness, H then reaches values smaller than 2 (close to 1.4) typically associated with the turbulent flow regime. Afterwards, the shape factor steadily increases towards laminar values. This evolution relates to the acceleration of the flow associated with a favourable pressure gradient in the flow field. After an exponential decay of the displacement and the momentum thickness, θ stabilizes while δ^* slightly increases over the rear part of the SS. The BL flow thus experiences a relaminarization process provoked by the strong PG such that the turbulent nature of the flow steadily develops towards a laminar again.

On the suction side, differences in the BL integral parameters are noticeable in Figure 7.12, especially between the $M = 0.7$ and the two high Mach number cases. For the low Mach number, the laminar evolution of the BL over the front part of the SS is characterized by a steady increase in θ and δ^*. Then, a strong rise in displacement thickness is observed related to the laminar separation. The momentum thickness experiences a strong increase in the region when δ^* is already decreasing. This is related to the transition of the flow and the onset of turbulence associated with an increased momentum transfer. The shape factor follows this evolution. It first lays over 2 and experiences an increase before rapidly decaying into the turbulent flow range at the end of the SS. Thus, after closing the separation bubble and the onset of the turbulent regime both quantities, δ^* and θ, decrease simultaneously towards the TE of the blade. For the higher Mach number cases, the evolution is similar in the beginning but the abrupt increase in displacement thickness occurs later. Hence, the separation of the flow happens just after the shock location. After reaching a maximum, δ^* decreases again due to the reattachment of the separation region by pressure recovery phenomena. Simultaneously, the momentum thickness experiences a nearly steady increase all along the suction side with a small local increase due to the separation. Nevertheless, no strong rise in θ is observed as was the case for the previously discussed BL evolutions related to the turbulence onset. Even though the flow starts to transition, the transition is in its early phase such that the turbulent regime is not yet sufficiently developed. The shape factor stays accordingly in the laminar range well above 2. The same observation can be made for the $M = 0.95$ case which is typically associated with slightly smaller thicknesses but the overall pattern is the same. Also, the shock location seems to be closer to the separation region than for the moderate Mach number configuration.

7.5 Wake

Finally, the wake region of the flow is studied more closely. On the one hand, the losses generated will be discussed by considering the total pressures and temperatures and, on the other hand, the turbulent behaviour of the wake as well as its unsteadiness will be investigated. Therefore, most measurements were extracted using probe sets distributed on two reference planes in the wake. These planes are located at $0.25 \times c_{ax}$ and $0.5 \times c_{ax}$ behind the TE of the blade and correspond to the experimental reference planes 05 and 06 (see Figure 2.2).

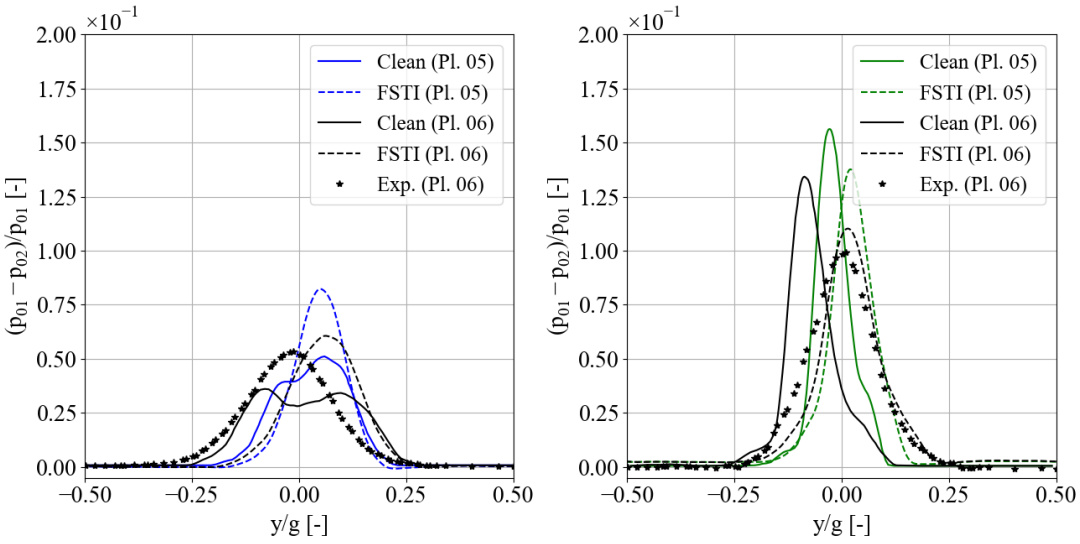

(a) Case $M = 0.7$.

(b) Case $M = 0.9$.

Figure 7.13: Temporal and spanwise average of the pressure defect in the wake quantifying the generated losses. The distributions are measured at the reference planes 05 & 06 for the different considered cases. The configurations with turbulence injection are presented and the numerical data related to the setup without free stream turbulence [4] as well as the experimental data [35] are included for comparison.

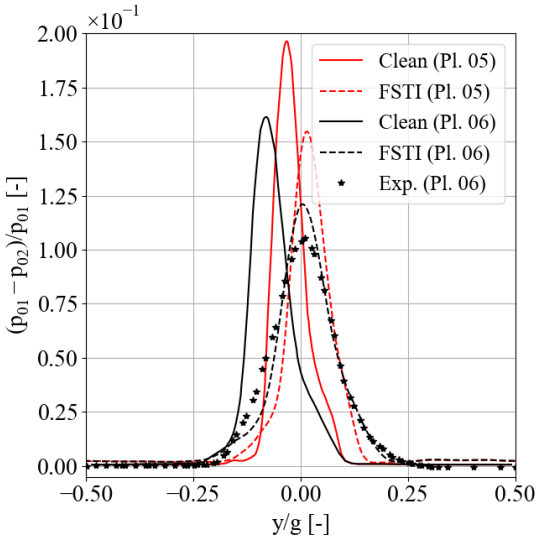

(c) Case $M = 0.95$.

Figure 7.13: Temporal and spanwise average of the pressure defect in the wake quantifying the generated losses. The distributions are measured at the reference planes 05 & 06 for the different considered cases. The configurations with turbulence injection are presented and the numerical data related to the setup without free stream turbulence [4] as well as the experimental data [35] are included for comparison.

In Figure 7.13 are shown the respective total pressure defects measured experimentally and numerically. Due to sensor constraints, the experimental data is only available at plane 06 whereas the numerical data for both approaches, with and without free-stream turbulence, is presented. As discussed in subsection 3.1.3, the pressure defect can be used as a measure for the generated losses under certain assumptions [10]. It can be observed that with increasing Mach number the generated losses increase as well [56], [65]. This trend is present for all the different approaches. Next to that, the width of the distribution is comparable between the different Mach number cases with the higher Mach numbers just being more elongated and thus reaching larger values. The streamwise decay of the total pressure is present in all the configurations. Additionally, the decreases observed seem to behave proportionally with respect to the magnitude of the total pressure defect. In terms of visualisation, one can see in Figure 7.2, that the wake of the blade dictated by the vortex street phenomenon is much cleaner and more energetic for the high Mach number cases. In Figure 7.13, the experimental data seems to be much better matched by the statistics collected for the case with turbulence injection. Indeed, the respective curves are much closer and their evolutions are very similar. However, the numerical approach slightly overpredicts the experimental values for each of the configurations. Considerable differences are observed with respect to the numerical case without free-stream turbulence. The clean case is considerably smaller than predicted for the low Mach number case and significantly larger for the higher Mach number cases. Some discrepancies can also be seen in the spatial shifts of the peaks with respect to mid-pitch. Next to that the distributions for the $M = 0.7$ case are characterized by more varying profiles than the common smooth distribution. As investigated by several studies, the loss typically decreases with increasing Reynolds number and the presence of higher free-stream turbulence [2], [40], [43]. The low Mach number case does not follow this behaviour which can be related to the fact that the flow features observed are considerably different in both numerical approaches for this case. Indeed, the clean case experiences on average an open separation region on the SS whereas the free-stream turbulence case achieves to close the bubble thus strongly impacting the wake phenomenon. It can be noticed that the various distributions related to the case with turbulence injection are all decentralised in the same manner with respect to the mid-pitch. Hereby, slightly larger shifts can be observed for the lower Mach numbers. Another important observation concerns the tails of the distributions. Indeed, one can notice that for the high Mach number cases, the distribution does not converge towards 0 in the upper and lower pitch regions. In comparison, the experimental measurements and numerical data without free-stream turbulence both tend to 0 at their tails. This unexpected behaviour can be linked to the turbulence injection procedure. Hence, through the injection of turbulent structures consisting of superimposed velocity fluctuations, the total pressure applied at the inlet boundary is artificially increased. A compensation operation is nevertheless implemented within the injection procedure to adapt the imposed total pressure of the flow and obtain the targeted conditions. However,

due to the previous discrepancies observed in the injected turbulence field, this compensation may also have been affected thus provoking a slight impact on the overall flow conditions.

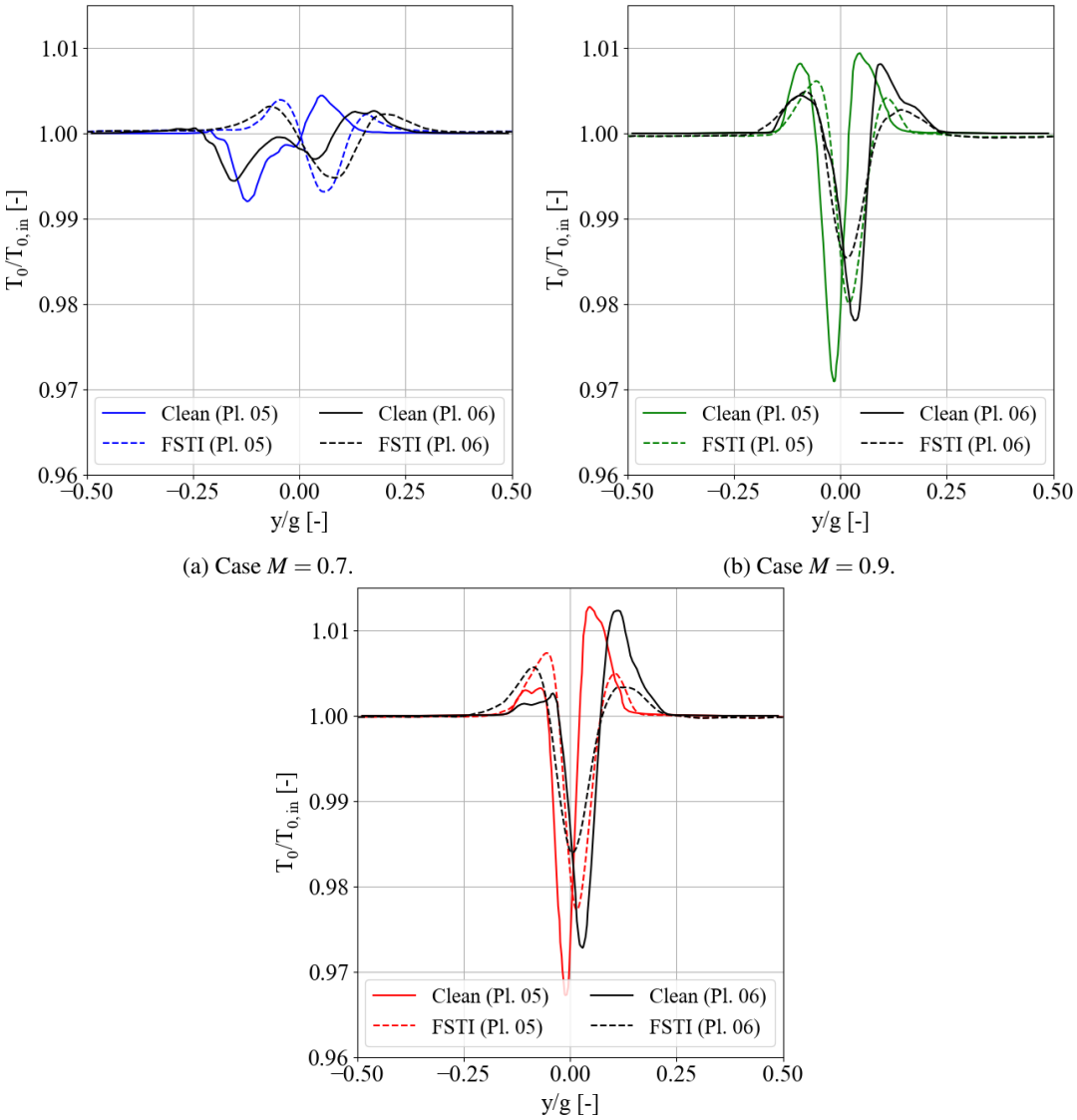

(a) Case $M = 0.7$.

(b) Case $M = 0.9$.

(c) Case $M = 0.95$.

Figure 7.14: Temporal and spanwise average of the normalized total temperature in the wake. The distributions are measured at the reference planes 05 & 06 for the different considered cases. The configurations with turbulence injection are presented and the numerical data related to the setup without free stream turbulence [4] is included for comparison.

Complementary to the total pressure defect, the total temperature distribution across the wake region is illustrated in Figure 7.14. In the context of the loss study, the total temperature describes in a larger sense the entropy generated and thus the losses created in the flow. As mentioned previously, the magnitude of generated losses increases the higher the Mach numbers. This statement is confirmed in the present case since the extents and variations of the curves for higher M are significantly larger compared to the smaller Mach numbers. In terms of streamwise evolution, the distribution of T_0 seems to reduce and spread out thus losing its amplitude when travelling from plane 05 to plane 06. When comparing both numerical approaches with and without free-stream turbulence, similar patterns can be observed. Nevertheless, the amplitudes and local deviations of the curves without turbulence injection are considerably larger which is in accordance with [40]. As for the pressure defect, one can notice that the tails of the distributions do not converge to their expected value which in occurrence corresponds to 1. This observation, especially made for the high Mach number cases, can directly be related to

a similar issue encountered for the total pressure distribution. As discussed in that context, the problem results from an issue concerning the turbulence injection procedure and more precisely the imposed total conditions at the inlet boundary.

Figure 7.15 shows the spanwise and temporal averaged flow angle distribution at the reference planes in the wake. The outlet metal angle of the blade, equal to 53.8°, is added to illustrate the relative deviation of the flow. One can notice that the shape of the distribution is very similar between the three considered cases, especially at plane 05. The curves associated with this plane are directly shaped by the vortex street developing in the wake and provoking the observed striking pattern. By passing downstream to plane 06, the distribution typically experiences an inversion as well as an overall smoothing of the variations such that a flatter curve is observed. As expected the mean flow angle α_{out} at both plane locations coincide such that the flow follows on average a constant angle when travelling downstream in the wake region. The average flow angle matches very well the outlet metal angle of the blade for the $M = 0.95$ case as can be seen in Figure 7.15. For lower Mach numbers, reduced flow angles are observed. In the $M = 0.7$ case, a flow deviation d of approximately $-0.5°$ is measured with respect to β_m. For the moderate Mach number, a deviation of $0.17°$ is observed on average. These increased deviations for lower Mach number can also be recognized in the pitchwise shifts of the curve peaks contained in Figure 7.13.

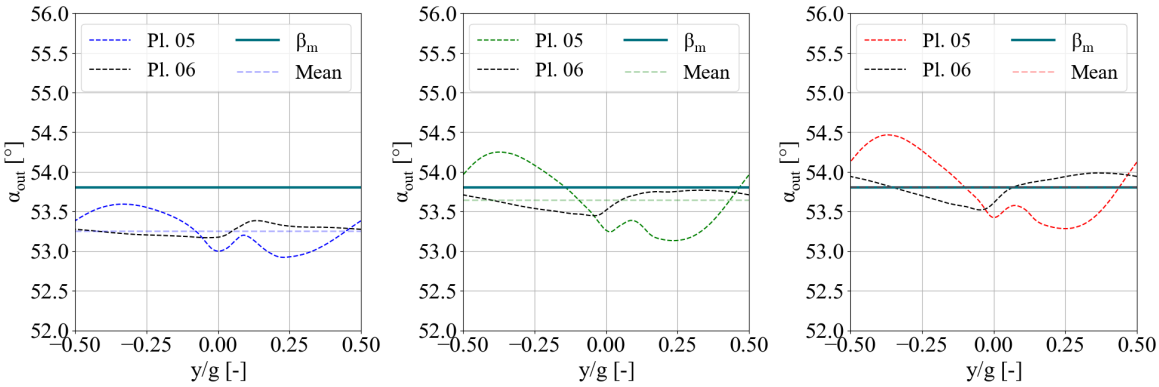

(a) Case $M = 0.7$. (b) Case $M = 0.9$. (c) Case $M = 0.95$.

Figure 7.15: Temporal and spanwise average of the flow angle in the wake. The distributions are measured at the reference planes 05 & 06 for the different considered cases. The outflow metal angle of the blade β_m is added to illustrate the deviation of the flow. Note that only the configurations with turbulence injection are presented.

Furthermore, the turbulent activity in the wake can be studied. As can be seen in the flow field shown in Figure 7.2 and Figure 7.3, the turbulence downstream of the wake is dominated by the von Karman vortex street. Indeed, the strong counterrotating vortices are ejected periodically from the TE of the blade thus forming the vortex street. The latter is dominantly a two-dimensional flow phenomenon. The vortex shedding gives rise to a cleaner and more coherent vortex street for the higher Mach numbers. Additionally, in these cases, the largest amounts of energy are contained in the turbulent structures composing the wake. To further analyse the turbulent content of the wake, the Reynolds stress tensor can be considered which is based on the autocorrelations of the velocity. Their spanwise and temporal averaged distributions along the reference planes are shown for the different configurations in Figure 7.16. There, two typical behaviours are noticeable. On the one hand, the low Mach number case is associated with the smallest Reynolds stresses. The $\overline{u'u'}$ and $\overline{v'v'}$ components are of the same order and are differentiated by spatial pitchwise shifts. The spanwise component $\overline{w'w'}$ is more or less centred and shows the third strongest fluctuations of approximately half the value of the other two diagonal components. Then follows the non-diagonal $\overline{u'v'}$ component while the remaining two off-diagonal components tend to zero on average. By travelling downstream from plane 05 to 06, the turbulence experiences an overall decay of all its components such that the previous distribution is kept but now significantly flatter. On the other hand, the two high Mach number cases are very similar with the streamwise component $\overline{u'u'}$ dominating the distributions with a clean and centred peak. The amplitudes for both cases are very similar, the moderate Mach number case even being slightly larger than the $M = 0.95$ case. The pitchwise component $\overline{v'v'}$ has a typical "M"-shape and corresponds to approximately half of the streamwise one. The $\overline{w'w'}$ and $\overline{u'v'}$ are both of the same order typically corresponding to the quarter of $\overline{u'u'}$. The other off-diagonal contributions are again zero on average. A noticeable difference can

be observed between both streamwise planes, such that the $\overline{u'v'}$ component experiences a considerably stronger decrease with respect to the simultaneous decay of the diagonal components. The striking differences observed between the low and high Mach number cases can be led back to the distinct flow behaviours of the vortex street. Indeed, for the $M = 0.7$ case, the vortex shedding is less clean and coherent while it is simultaneously more spread out, as illustrated in Figure 7.2.

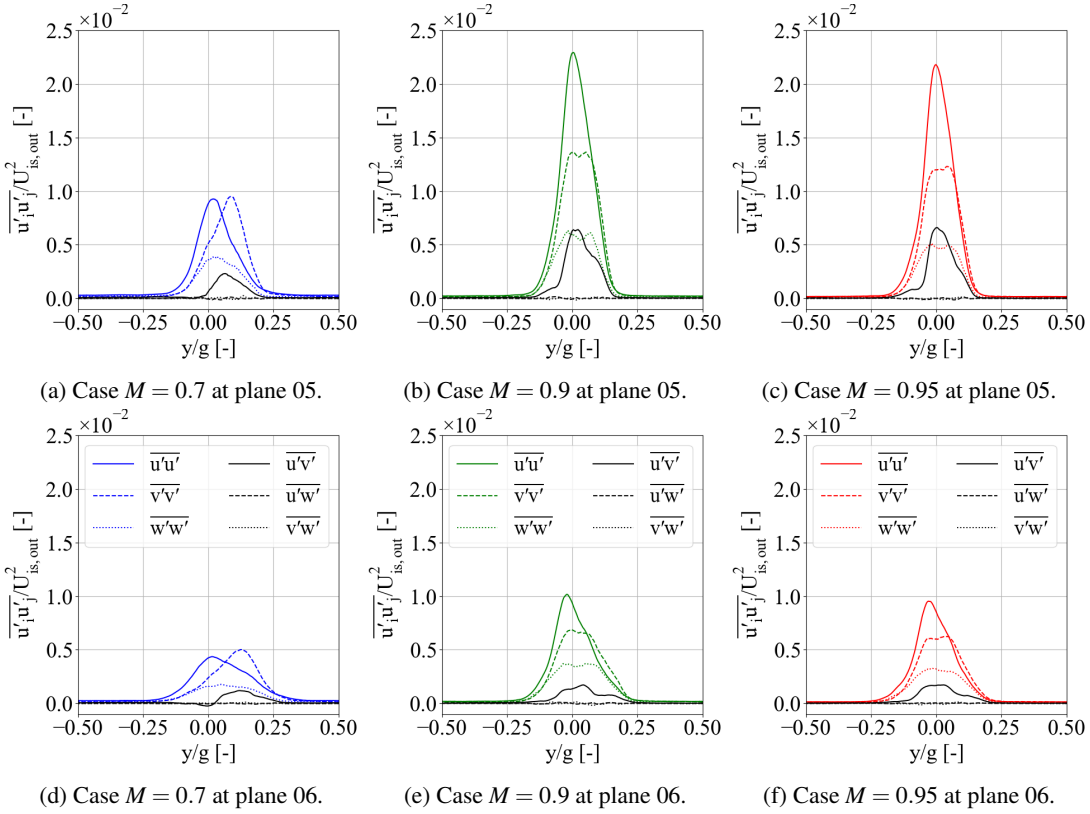

(a) Case $M = 0.7$ at plane 05. (b) Case $M = 0.9$ at plane 05. (c) Case $M = 0.95$ at plane 05.

(d) Case $M = 0.7$ at plane 06. (e) Case $M = 0.9$ at plane 06. (f) Case $M = 0.95$ at plane 06.

Figure 7.16: Temporal and spanwise average of the Reynolds stresses in the wake. The distributions are measured at the reference planes 05 & 06 for the different considered cases. Note that only the configurations with turbulence injection are presented.

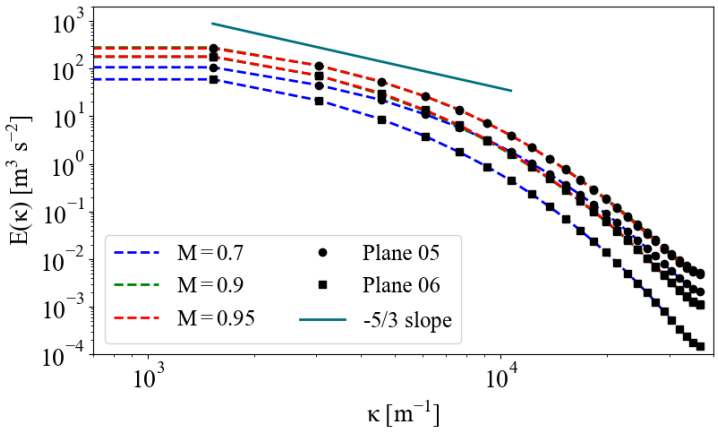

Figure 7.17: Spanwise averaged energy density spectrum extracted in the central part of the wake at the reference planes 05 & 06 for the different considered cases. Note that only the configurations with turbulence injection are presented.

To a further extent, the turbulence can be analysed from a spectral point of view. Therefore, the averaged energy density spectra for the different configurations are shown in Figure 7.17. It can be seen that considerably higher turbulence contents are present for the two higher Mach number cases. The streamwise decay of the turbulence is illustrated with respect to both reference planes. The $-5/3$ slope is added as a reference to mark the inertial subrange region associated with the turbulence cascade concept. Note that the region corresponding to the smaller scales is typically characterized by a steeper slope for plane 06. These changes in the curve have implications on the inertial subrange which is hereby enlarged for the spectra at the downstream plane.

In a third approach, the turbulence present in the wake can be characterized by the integral length scales of its structures. Therefore, the normalized length scales measured along the spanwise direction for velocity fluctuations in the respective spatial directions are illustrated in Figure 7.18. These quantities characterizing the size of the large-scale turbulent structures are based on the measured two-point autocorrelations. Note that for redundancy reasons the length scales are only presented at the reference plane 06. The central region of the distribution is typically dictated by the vortex street. This predominantly two-dimensional flow phenomenon gives rise to increased length scales in the x and y directions while the spanwise length scales are considerably smaller. These patterns can be observed for all the different Mach number cases, but they are more apparent for the higher Mach number cases in which a clean and stable vortex street is present. Also, this central region is characterized by a smooth distribution obtained by the presence of the large and coherent vortical structures in this flow region. When leaving the central pitchwise region and taking a look at the outer regions corresponding to the free stream, a fundamentally different picture can be seen. There, the distributions are characterized by small-scale oscillations and the pitch- and spanwise directions are associated with the largest integral length scales. Hereby, the spanwise direction experiences smaller oscillations and is dominating while the length scales in the x direction are very reduced. The turbulent structures in the free stream are characterized by the injected turbulence which has evolved since the injection. Indeed, the structures were subjected to elongation and variations induced by different flow features encountered when travelling downstream and passing through the turbine passage. In the free stream of the wake, fewer, smaller and only local structures of small energetic content are present compared to the energetic and large-scale vortex street. Thus, the integral length scale distributions, which are based on the computation of spatial correlations, are affected by this characteristic such that these small local variations appear. Note that the half-span of the computational domain is added as a reference to assess the sufficient spanwise thickness of the domain. Even though the flow is mainly two-dimensional due to the presence of vortex shedding, the domain span needs to be large enough to represent all the secondary flow features especially the ones of turbulent nature. The integral length scales describing the size of the turbulent structures obtained in the free stream of the wake region are thus presented in Figure 7.18. The largest length scales observed are typically of the size of a quarter of the spanwise thickness. Thus, these observations give us good confidence about the sufficient spanwise size of the domain.

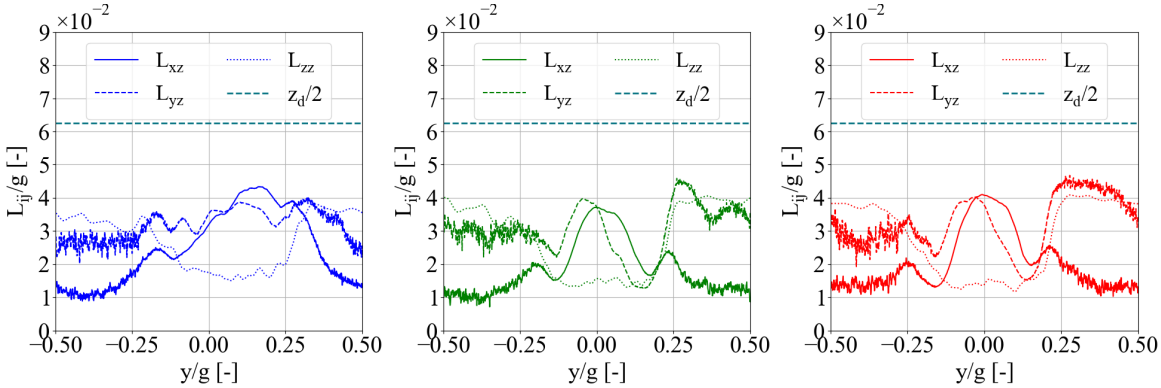

(a) Case $M = 0.7$ at plane 06. (b) Case $M = 0.9$ at plane 06. (c) Case $M = 0.95$ at plane 06.

Figure 7.18: Normalized integral length scales computed along the spanwise direction (z) for velocity fluctuations monitored in the existing spatial directions. The distributions are measured at the reference plane 06 for the different considered cases. The half of the normalized spanwise thickness of the domain ($z_d/(2g)$) is illustrated for comparison reasons. Note that only the configurations with turbulence injection are presented.

8 Conclusion

In the present work, the flow in high-speed LPT has been investigated in on- and off-design conditions. Hereby, the three outlet isentropic Mach numbers 0.7, 0.9 and 0.95 were considered combined with a low outlet isentropic Reynolds number of 70×10^3 based on the true chord. Under these mainly transonic conditions, especially compressible effects, such as shocks, were studied in detail. Next to that also the boundary layer behaviour was investigated in-depth due to their impact on losses and thus the overall performance. The numerical high-fidelity approach chosen, *i.e.*, quasi-3D DNS, allowed us to capture and extract all the complex flow phenomena happening in the flow field.

To attain this aforementioned goal, the experimental background related to the SPLEEN project was first considered by specifying the most important characteristics in terms of experimental free-stream turbulence intensity. Then, the various flow physics occurring in LPT flows were considered. In this context, the turbulence, BL and wake were redefined by highlighting their intrinsic properties and behaviours. The performance parameters as well as the losses generated in turbine flows were formalized for later use. Through an in-depth discussion of the flow behaviour in LPT based on available literature, a first understanding of the flow was obtained. Especially the interaction between transition and separation phenomena was investigated at the boundary layer level of the blade. Hereby, the dictating parameters were pointed out as the pressure gradient and the momentum Reynolds number while different separation behaviours can be encountered based on the flow properties. The evolution of the blade loading with respect to flow properties such as the free-stream turbulence or the Reynolds number were then studied. An increased Reynolds number was thus linked to improved performances characterized by a faster reattachment of the flow after separation at the suction side. The turbulence effects were especially observed at a low Reynolds number in which bypass transition was able to develop leading to a faster reattachment of the flow due to the turbulent regime properties. Afterwards, the computational framework was set by introducing the cluster Lucia, the solver ArgoDG as well as the discontinuous Galerkin method. In the continuity of this discussion, the domain and the mesh definitions were considered combined with the imposed boundary conditions characterizing the range of operating conditions spanned. Then, the turbulence injection method was introduced. The complete setup and all the procedures related to the precursor method were highlighted. The computation and results of the auxiliary simulation were presented before extracting the turbulent flow field of the targeted TI level. When analysing the evolution of injected turbulence in the main domain, some deviations with respect to the predictions could be observed. Indeed, a slower turbulent decay as well as the presence of some anisotropy in the turbulent flow features was experienced. The FSTI obtained at the blade level was nevertheless in the scope of 2.8-3.0% depending on the Mach number case. These TI values were slightly higher than the experimental value of 2.34% measured half-chord upstream of the blade, but they still lay within the targeted and satisfactory range (1.5-3.5%).

Finally, the numerical results extracted from the main simulation were discussed. In a first stage, the overall flow field was investigated to form an intuitive understanding of the flow. These first observations were then completed by in-depth studies of the blade loading, the boundary layer stability as well as the wake content. The loading of the blade studied with the isentropic Mach number distribution around the blade identified that the velocity peak at the SS was shifted downstream when considering a higher Mach number. The distribution obtained showed a close matching with the experimental data by considerably reducing some differences observed in the comparison with the numerical case without free-stream turbulence. This better matching was especially observed for the complete low Mach number case and furthermore expressed in the separation region on the PS

of each Mach number case. In these configurations, the flow effects of free-stream turbulence were thus present and well perceived. In terms of BL stability, a separation region was observed for all the Mach numbers in the rear part of the SS. However, their behaviours were fundamentally different between low and high Mach number cases. For $M = 0.7$, the separation happens the earliest, on average around 0.61% of the SS, as was identified by the skin friction as well as the velocity distribution. The laminar separation region was closed after a considerable length by the transition of the flow to a fully turbulent regime. After the reattachment, a turbulent BL profile characterized by a fuller shape developed until the TE. For the transonic and the choked Mach numbers, the interaction between the BL and the shocks became a key feature. In both cases, the separation occurred in direct proximity to the main shock location. The average separation points for $M = 0.9$ and 0.95 respectively corresponded to 0.70% and 0.72% of the SS. In this context, the shock was located slightly upstream and provoked a considerable pressure increase in the flow which magnified the adverse pressure gradient leading to premature separation of the BL flow. Through the pressure recovery effect, the flow then achieved to reattach shortly after separation thus forming a small laminar separation bubble. With the presence of the separation and the associated free shear layer, the onset of transition happened but the phenomenon evolved only slowly such that a quasi-laminar regime was observed with very reduced turbulent content. Hence, the BL profiles reaching the blade were of a large thickness and laminar shape while being additionally characterized by the APG acting in this area of the SS. The separation in the subsonic case presented strong fluctuations with periodic bursting of the separation bubble. The high Mach numbers exhibited more stable separation locations which were intrinsically linked to the shock position. The laminar separation observed in the front part of the PS was characterized by a fast reattachment combined with a separated-flow transition for all three cases. The downstream flow was fully turbulent and shaped by ejected vortices before being accelerated and potentially experiencing relaminarization. The presence of several shocks in the flow passage for the high Mach numbers blocked the propagation of acoustic perturbations generated in the wake whereas the latter could travel without restrictions in the $M = 0.7$ domain. Note that only for $M = 0.95$ the flow passage was completely choked. The BL status towards the rear of the SS had a direct impact on the wake and especially the stagnation region behind the TE. This so-called base flow region was much larger for the higher Mach numbers due to their larger momentum defect in the BL illustrated by the velocity profiles. The wake region which was characterized by the von Karman vortex street was investigated using the vorticity field. In this context, the wake for $M = 0.7$ had a more chaotic, spread-out and unstable behaviour as well as a less energetic content than the high Mach numbers. Indeed, the wakes for the latter had a clean and coherent appearance. The decay of the wake was further investigated by analysing the evolution of the Reynolds stress tensor. Finally, the losses were quantified using the entropy creation as well as the total pressure and total temperature defects. The high Mach numbers were hereby linked to considerably larger losses. A difference in the flow deviation was also observed among the considered Mach number cases. Hence, the smaller Mach numbers were associated with larger deviations.

The present work allowed us to assess the performance and the detailed flow behaviour of a high-speed LPT with elevated FSTI. Through the extraction of meaningful flow statistics, the various flow features could be investigated and characterized by especially focusing on the most important flow phenomena. Nevertheless, several considerations remain open and may need further investigation. This is especially the case for the turbulence injection procedure. Hence, considerable anisotropic behaviours of the free-stream turbulence have been observed leading to a deviation from the expected turbulent decay. In this context, the source of this discrepancy should be searched and rectified. Novel simulations with adequate setup may then be considered to evaluate the extent and the implications of the observed issues on the flow in the LPT cascade. In this context, also the strong pitchwise coherence of the free-stream turbulence may be improved by additional blending procedures. Regarding the discussion of the LPT cascade flow, more converged statistics may be accumulated over a larger number of convective times. Alternatively, other quantities such as the intermittency factor may be introduced to quantify the transition phenomenon in the BL region. The stagnation region close to the TE may also be studied in further detail by a more formal approach.

A Appendix

A.1 Turbulence injection computation

Table A.1: Mean convective velocity over the inlet region and important turbulence quantities related to the turbulence injection procedure.

Quantity	Units	Case 1	Case 2	Case 3
$\overline{U}_{in}$	[m/s]	144.06	159.52	160.11
Tu_{target}	[%]	2.20	2.20	2.20
k_{target}	[m^2/s^2]	15.060	18.437	18.567
$Tu_{extraction}$	[%]	5.214	4.936	5.647
$k_{extraction}$	[m^2/s^2]	84.614	92.998	122.642

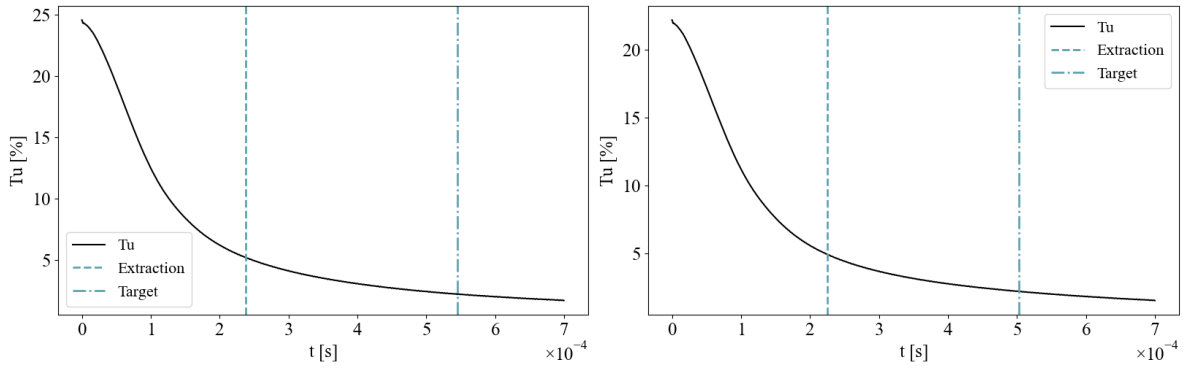

(a) (b)

Figure A.1: Temporal evolution of the turbulence intensity Tu in the turbulence box for the $M = 0.7$ case **(left)** and the $M = 0.9$ case **(right)**.

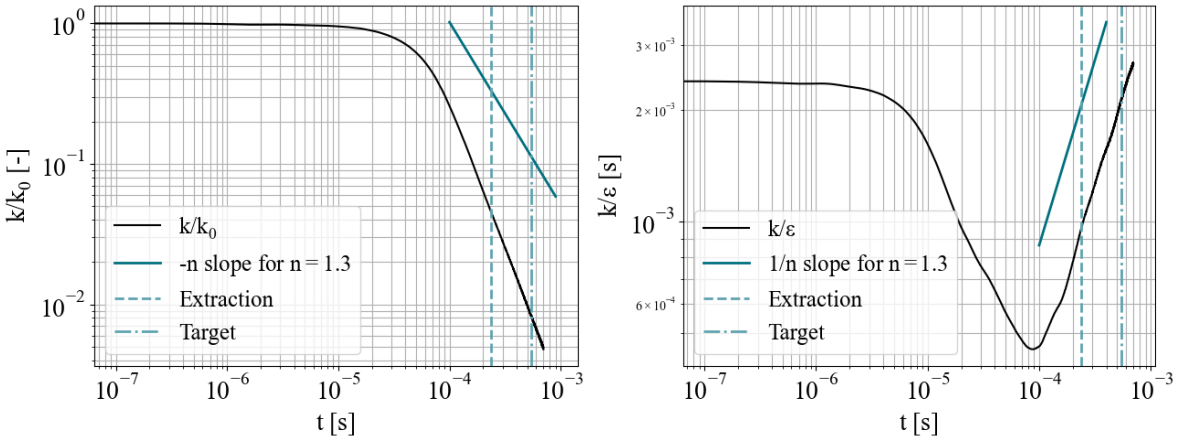

(a) (b)

Figure A.2: Temporal evolution of the normalized TKE **(left)** and the ratio of the TKE over dissipation rate **(right)** in the turbulence box for the $M = 0.7$ case.

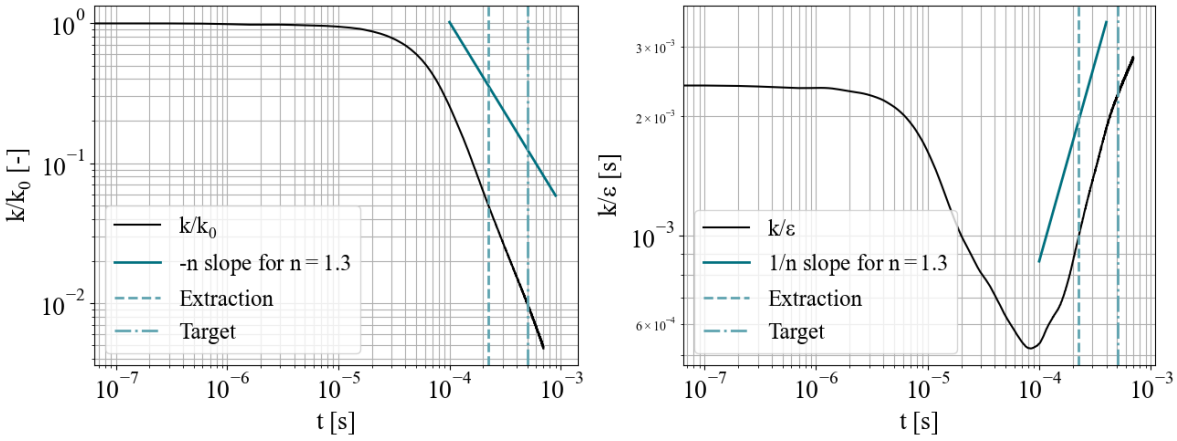

(a) (b)

Figure A.3: Temporal evolution of the normalized TKE **(left)** and the ratio of the TKE over dissipation rate **(right)** in the turbulence box for the $M = 0.9$ case.

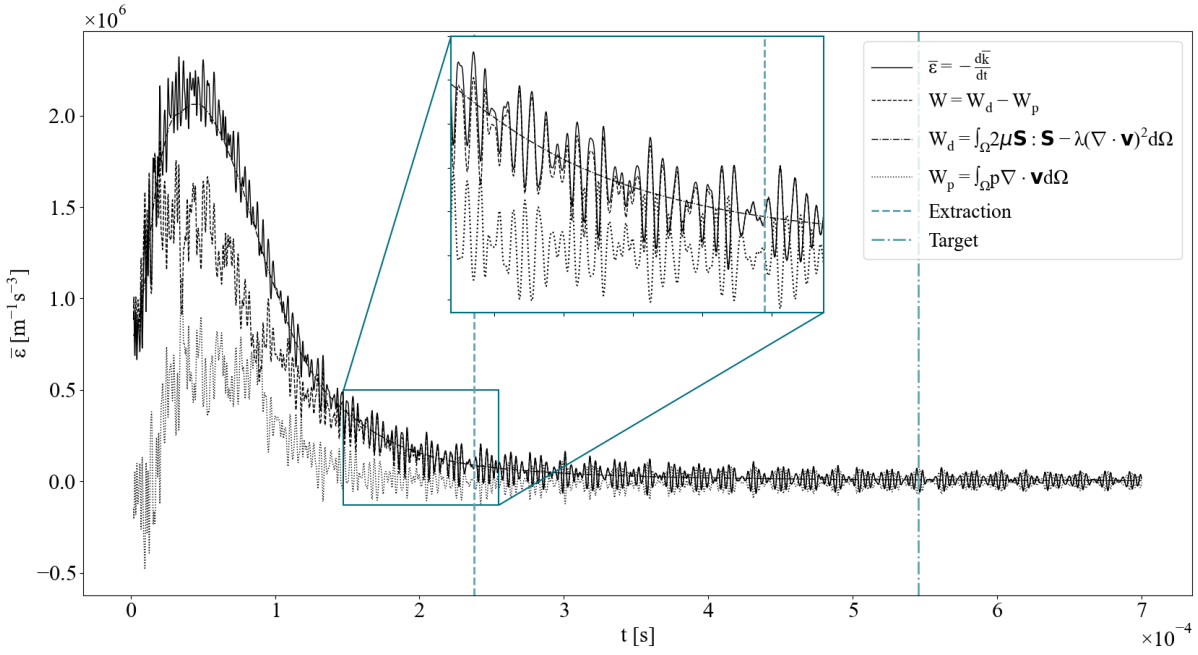

Figure A.4: Temporal evolution of the dissipation rate in the turbulence box for the $M = 0.7$ case.

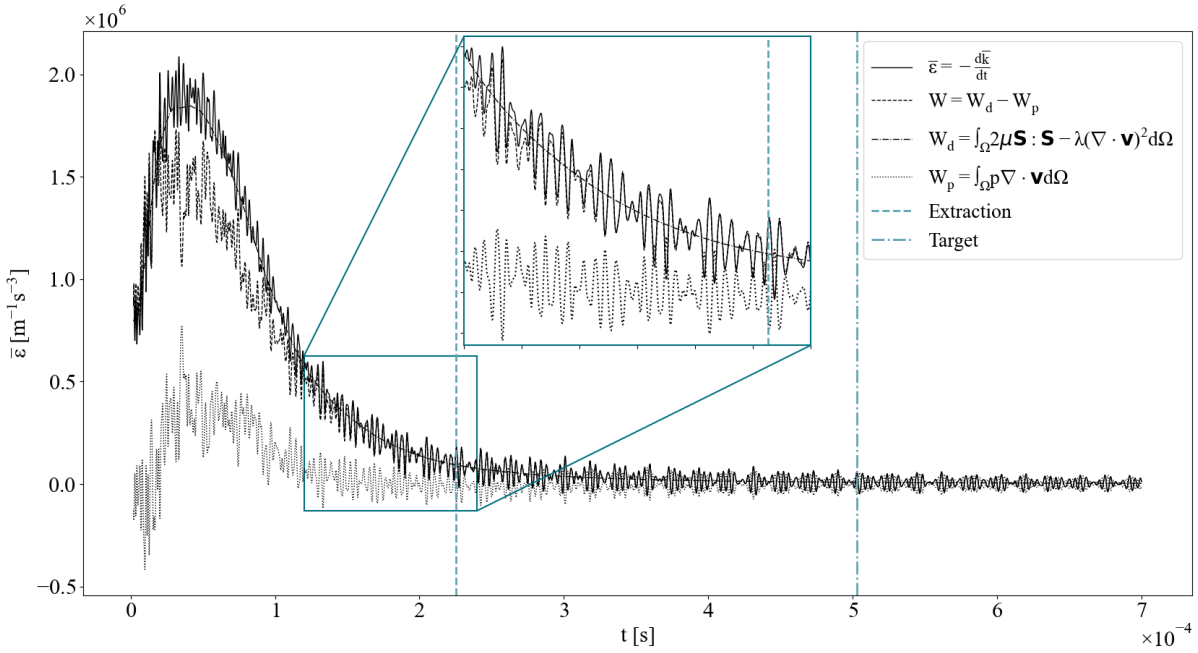

Figure A.5: Temporal evolution of the dissipation rate in the turbulence box for the $M = 0.9$ case.

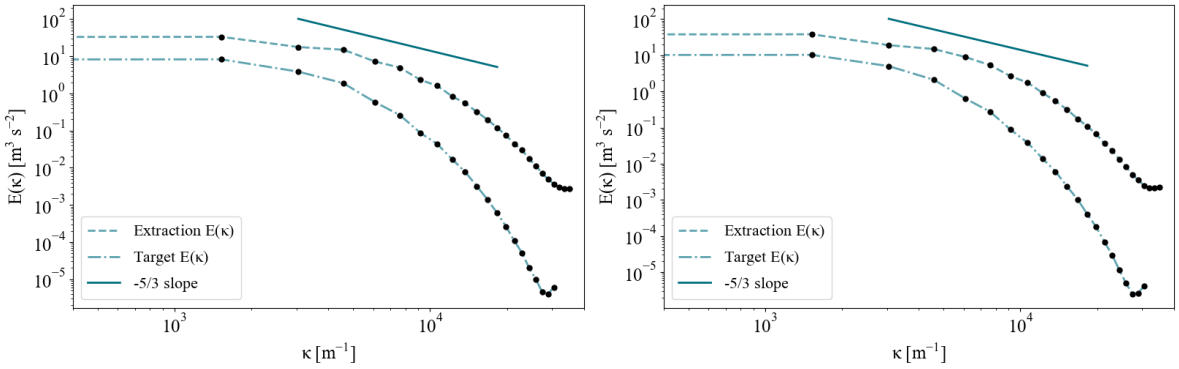

(a) (b)

Figure A.6: Energy density spectrum at the extraction instant for the $M = 0.7$ case **(left)** and the $M = 0.9$ case **(right)**.

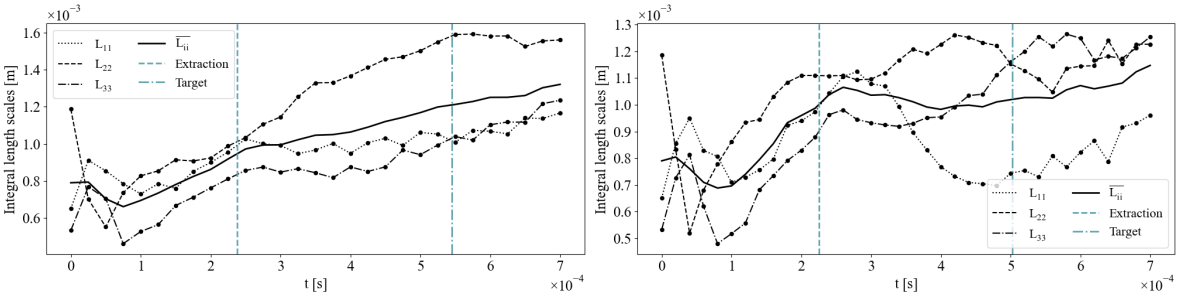

(a) (b)

Figure A.7: Temporal evolution of the integral length scales in the turbulence box for the $M = 0.7$ case **(left)** and the $M = 0.9$ case **(right)**.

List of Figures

List of Tables

References

[1] J. D. Anderson, *Fundamentals of Aerodynamics*. McGraw-Hill Education, 6th ed., 2017.

[2] A. Benyahia, L. Castillon, and R. Houdeville, "Prediction of separation-induced transition on high lift low pressure turbine blade," *Proceedings of ASME Turbo Expo 2011*, Vancouver, British Columbia, Canada, 2011.

[3] A. Bolyn, *Detailed Flow Analysis of a Transonic Low Pressure Turbine at Low Turbulence Levels*, University of Liège, 2020.

[4] M. Borbouse, *Boundary layer stability and shock interactions in a high-speed low pressure turbine cascade*, University of Liège, 2023.

[5] M. Börner and R. Niehuis, "Dynamics of Shock Waves Interacting With Laminar Separated Transonic Turbine Flow Investigated by High-Speed Schlieren and Surface Hot-Film Sensors," *Journal of Turbomachinery*, vol. 143, no. 5, ASM International, 2021, pp. 051010-051020. DOI: 10.1115/1.4050330.

[6] *CECI*, Accessed on May 8th, 2024. [Online]. Available: https://www.ceci-hpc.be/.

[7] B. Cockburn, G. E. Karniadakis, and C.-W. Sh, *Discontinuous Galerkin methods: theory, computation and applications*. Springer Science & Business Media, vol. 11, 2012.

[8] J. Dähnert, C. Lyko, and D. Peitsch, "Transition Mechanisms in Laminar Separated Flow Under Simulated Low Pressure Turbine Aerofoil Conditions," *Journal of Turbomachinery*, ASME, vol. 135, no. 1, 2013.

[9] P. A. Davidson, *Turbulence An Introduction for Scientists and Engineers*. Oxford University Press, 2004.

[10] J. D. Denton, "The 1993 IGTI Scholar Lecture: Loss Mechanisms in Turbomachines," *Journal of Turbomachinery*, vol. 115, no. 4, ASM International, 1993, pp. 621-656.

[11] N. S. Dhamankar, G. A. Blaisdell, and A. S. Lyrintzis, "Overview of Turbulent Inflow Boundary Conditions for Large-Eddy Simulations," *AIAA Journal*, vol. 56, 2017. DOI: 10.2514/1.J055528.

[12] *Documentation Lucia*, Accessed on May 8th, 2024. [Online]. Available: https://doc.lucia.cenaero.be/.

[13] V. Dolejší and M. Feistauer, *Discontinuous Galerkin Method: Analysis and Applications to Compressible Flow*. Springer Series in Computational Mathematics, vol. 48, 2015.

[14] A. Dufau, J. Marty, D. Man, and E. Piot, "High-Fidelity Simulations of the Flow Around T106C Cascade at Low Reynolds Number: The Effects of Freestream Turbulence and Stagger Angle," *ASME Turbo Expo 2022*, June 2022, ROTTERDAM, Netherlands.

[15] A. Dufau, J. Marty, D. Man, and E. Piot, "The effect of Reynolds number on the flow around the T106C very high lift low pressure turbine linear cascade," *ETC 15 - European Turbomachinery Conference*, April 2023, Budapest, Hungary.

[16] P. A. Durbin and B. A. P. Reif, *Statistical Theory and Modeling for Turbulent Flows*. John Wiley & Sons Ltd, 2nd ed., 2011.

[17] M. Fiore and N. Gourdain, "Reynolds, Mach, and Freestream Turbulence Effects on the Flow in a Low-Pressure Turbine," *Journal of Turbomachinery*, vol. 143, no. 10, ASM International, 2021, pp. 101009-1010022. DOI: 10.1115/1.4050919.

[18] F. N. Frenkiel, "The Decay of Isotropic Turbulence," *Jounral of Applied Mechanics*, vol. 15, no. 4, 1948, pp. 311-321.

[19] K. Fukami, Y. Nabae, K. Kawai, and K. Fukagata, "Synthetic turbulent inflow generator using machine learning," *Physical review Fluids*, ed. 4, 064603, 2019. DOI: 10.1103/PhysRevFluids.4.064603.

[20] A. Garai, L. T. Diosady, S. M. Murman, and N. K. Madavan, "DNS flow in a low-pressure turbine cascade using a discontinuous-Galerkin spectral-element method," *Proceedings of ASME Turbo Expo 2015: Turbine Technical Conference and Exposition*, June 2015, Montreal, Canada.

[21] A. Garai, L. T. Diosady, S. M. Murman, and N. K. Madavan, "DNS of low-pressure turbine cascade flows with elevated inflow turbulence using a discontinuous-Galerkin spectral-element method," *Proceedings of the ASME Turbo Expo 2016: Turbomachinery Technical Conference and Exposition*, June 2016, Seoul, South Korea.

[22] C. Geuzaine and J.-F. Remacle, "Gmsh: A 3-d finite element mesh generator with built-in pre-and post-processing facilities," *International journal for numerical methods in engineering*, vol. 79, no. 11, 2009, pp. 1309–1331.

[23] M. Hao, J. Hope-Collins, and L. di Mare, "Generation of turbulent inflow data from realistic approximations of the covariance tensor," *Physics of Fluids*, ed. 34, 115140, 2022. DOI: 10.1063/5.0106664.

[24] A. Hatman and T. Wang, "A Prediction Model for Separated-Flow Transition," *Journal of Turbomachinery*, ASME, vol. 121, no. 3, 1999, pp. 594–602.

[25] K. Hillewaert, "Development of the discontinuous Galerkin method for high resolution, large scale CFD and acoustics in industrial geometries," Ph.D. dissertation, Université catholique de Louvain, 2013.

[26] C. Hirsch, *Numerical Computation of Internal and External Flows. Volume 1: Fundamentals of Computational Fluid Dynamics*. Butterworth-Heinemann, 2nd ed., 2007.

[27] J. Hourmouziadis, "Aerodynamic design of low pressure turbine," *AGARD Lecture Series*, vol. 187, 1989.

[28] A. Keating and U. Piomelli, "A dynamic stochastic forcing method as a wall-layer model for large-eddy simulation," *Journal of Turbulence*, vol. 7, 2006. DOI: 10.1080/14685240612331392460.

[29] A. Keating, U. Piomelli, E. Balaras, and H.-J. Kaltenbach, "A priori and a posteriori tests of inflow conditions for large-eddy simulation," *Journal of fluids*, vol. 16, 2004. DOI: 10.1063/1.1811672.

[30] M. Khateeb, *Impact of Operating Conditions on the Transitional Flow in a Low- pressure Fast Turbine Cascade*, University of Liège, 2021.

[31] J. Kim and C. Lee, "Deep unsupervised learning of turbulence for inflow generation at various reynolds numbers," *Journal of Computational Physics*, ed. 406, 109216, 2020. DOI: 10.1016/j.jcp.2019.109216.

[32] A. N. Kolmogorov, "The Local Structure of Turbulence in Incompressible Viscous Fluid for Very Large Reynolds Numbers," *Proceedings of the Royal Society of London*, vol. 434:9-13, 1991.

[33] P. K. Kundu and I. M. Cohen, *Fluid Mechanics*. Academic Press, 2nd ed., 2001.

[34] J. Larsson, "Blending technique for compressible inflow turbulence: Algorithm local- ization and accuracy assessment," *Journal of Computational Physics*, vol. 228, 2009. DOI: 10.1016/j.jcp.2008.10.027.

[35] S. Lavagnoli, G. Lopes, L. Simonassi, and A. F. M. Torre, *SPLEEN - High Speed Turbine Cascade – Test Case Database*, Zenodo, Jun. 23, 2023. [Online]. Available: 10.5281/zenodo.8075795.

[36] S. Lee, S. K. Lele, and P. Moin, "Direct numerical simulation of isotropic turbulence interacting with a weak shock wave," *Journal of Fluid Mechanics*, ed. 251, pp. 533-562, 1993. DOI: 10.1017/S0022112093003519.

[37] W. Lou and J. Hourmouziadis, "Separation Bubbles Under Steady and Periodic-Unsteady Main Flow Conditions," *Journal of Turbomachinery*, ASME, vol. 122, no. 4, 2000, pp. 634-643.

[38] T. Lund, X. Wu, and K. Squires, "Generation of inflow data for spatially-developing boundary layer simulations," *Journal of Computational Physics*, ed. 140, 233–258, 1998. DOI: 10.1006/jcph.1998.5882.

[39] R. E. Mayle, "The 1991 IGTI Scholar Lecture: The Role of Laminar-Turbulent Transition in Gas Turbine Engines," *Journal of Turbomachinery*, vol. 113, no. 4, ASM International, 1991, pp. 509-536.

[40] J. Michálek, M. Monaldi, and T. Arts, "Aerodynamic Performance of a Very High Lift Low Pressure Turbine Airfoil (T106C) at Low Reynolds and High Mach Number With Effect of Free Stream Turbulence Intensity," *Journal of Turbomachinery*, ASME, vol. 134, no. 1, 2012.

[41] V. Michelassi, L.-W. Chen, R. Pichler, and R. D. Sandberg, "Compressible Direct Numerical Simulation of Low-Pressure Turbines - Part II: Effect of Inflow Disturbances," *Proceedings of ASME Turbo Expo 2014: Turbine Technical Conference and Exposition*, June 2014, Düsseldorf, Germany.

[42] MTU, *Pratt & Whitney GTF engine*, https://www.mtu.de/engines/commercial-aircraft-engines/narrowbody-and-regional-jets/gtf-engine-family/.

[43] R. Pacciani, M. Marconcini, A. Arnone, and F. Bertini, "A CFD study of low Reyndolds number flow in high lift cascade," *Proceedings of ASME Turbo Expo 2010: Power for Land, Sea and Air*, June 2010, Glasgow, UK.

[44] T. Passot and A. Pouquet, "Numerical simulation of compressible homogeneous flows in the turbulent regime," *Journal of Fluid Mechanics*, vol. 181, 1987, pp. 441-466.

[45] S. B. Pope, *Turbulent Flows*. Cambridge University Press, 2000.

[46] M. Quadrio, *Turbulence: Physics and Modeling*. [Lecture notes]. Politecnico di Milano, 2023-2024.

[47] M. Rasquin, J.-F. Thomas, T. Toulorge, P. Bechlars, M. Franke, and K. Hillewaert, "Direct numerical simulations of airfoil cascades for the improvement of turbulence models through database generation," *In Proceedings of 15th European Conference on Turbomachinery Fluid dynamics & Thermodynamics, ETC15, April 24-28, 2023*, Budapest, Hungary. ETC15, 2023.

[48] L. F. Richardson, *Weather prediction by numerical process*. Cambridge University Press, 1922.

[49] P. E. Roach, "The generation of nearly isotropic turbulence by means of grids," *International Journal of Heat and Fluid Flow*, vol. 8, no. 2, 1987, pp. 82-92.

[50] R. S. Rogallo, "Numerical Experiments in Homogeneous Turbulence," *NASA Technical Memorandum*, 1981.

[51] K. Sabnis and H. Babinsky, "A review of three-dimensional shock wave–boundary-layer interactions," *Progress in aerospace sciences*, vol. 143, 2023.

[52] N. D. Sandham, "Shock-Wave/Boundary-Layer Interactions," *NATO, Science and technology organization*, RTO-EN-AVT-195, 2012.

[53] H. Schlichting and K. Gersten, *Boundary-Layer Theory*. Springer, 9th ed., 2017.

[54] J. T. Schmitz, S. C. Morris, R. Ma, *et al.*, "Highly loaded low-pressure turbine: design, numerical and experimental analysis," *Proceedings of ASME Turbo Expo 2010: Power for Land, Sea and Air*, June 2010, Glasgow, UK.

[55] L. Sedov, *Similarity and Dimensional Methods in Mechanics*. CRC Press, 10th ed., 1993.

[56] C. Sieverding and M. Manna, "A Review on Turbine Trailing Edge Flow," *International Journal of Turbomachinery, Propulsion and Power*, vol. 5, no. 2, 2020, pp. 1-55.

[57] L. Simonassi *et al.*, "An experimental test case for transonic low-pressure turbines - part 1 : Rig Design, instrumentation and experimental methodology," *Volume 10B : Turbomachinery - Axial Flow Turbine Aerodynamics ; Deposition, Erosion, Fouling, and Icing ; Radial Turbomachinery Aerodynamics*, 2022.

[58] L. Simonassi *et al.*, "An experimental test case for transonic low-pressure turbines - part 2 : Cascade aerodynamics at on- and off-design Reynolds and Mach numbers," *Volume 10B : Turbomachinery - Axial Flow Turbine Aerodynamics ; Deposition, Erosion, Fouling, and Icing ; Radial Turbomachinery Aerodynamics*, 2022.

[59] *SPLEEN project*, Accessed on May 2th, 2024. [Online]. Available: https://www.h2020-spleen.eu/.

[60] W. Sutherland, "LII. The viscosity of gases and molecular force," *The London, Edinburgh, and Dublin Philosophical Magazine and Journal of Science*, ser. 5, vol. 36, iss. 223, 1893, pp. 507-531. DOI: 10.1080/14786449308620508.

[61] G. I. Taylor, "The spectrum of turbulence," *Proceedings of the Royal Society of London*, vol. 164:476–490, 1938.

[62] V. Terrapon, *Computational Fluid Dynamics*. [Lecture notes]. University of Liège, 2023-2024.

[63] V. Terrapon and T. Andrianne, *Aerodynamics*. [Lecture notes]. University of Liège, 2023-2024.

[64] Y. de Valk, *A novel construction of wind tunnel models for wind energy applications*, University of Twente, 2019.

[65] R. Vázquez and D. Torre, "The Effect of Mach Number on the Loss Generation of LP Turbines," *ASME Turbo Expo 2012: Turbine Technical Conference and Exposition. Copenhagen, Denmark*, 2012.

[66] M. Vera, H. P. Hodson, and R. Vázquez, "The Effect of Mach Number on LP Turbine wake-blade interaction," *Unsteady Aerodynamics, Aeroacoustics and Aeroelasticity of Turbomachines. Springer.*, 2006.

[67] *VKI - Research*, Accessed on May 3th, 2024. [Online]. Available: https://www.vki.ac.be/index.php/research-consulting-mainmenu-107.

[68] X. Wu, K. D. Squires, and T. S. Lund, "Large eddy simulation of a spatially developing turbulent boundary layer," *Supercomputing '95:Proceedings of the 1995 ACM/IEEE Conference on Supercomputing*, San Diego, CA, USA, 1995. DOI: 10.1145/224170.224408.

[69] X. Wu, "Inflow Turbulence Generation Methods," *Annual Review of Fluid Mechanics*, vol. 49, 2017, pp. 23-49.

[70] Z. Xiong, S. Nagarajan, and S. K. Lele, "Simple method for generating inflow turbulence," *AIAA Journal*, vol. 42, 2004. DOI: 10.1016/j.jcp.2008.10.027.

[71] S. Xu and M. Martin, "Assessment of inflow boundary conditions for compressible turbulent boundary layers," *Physics of Fluids*, ed. 16, 2623–2639, 2004. DOI: 10.1063/1.1758218.

[72] M. Zdravkovich, *Flow around circular cylinders. Volume 1: Fundamentals*. Oxford University Press, 1997.

[73] P. Zehner, "Étude aéroacoustique de l'interaction orthogonale pale/tourbillon," Ph.D. dissertation, Ecole nationale supérieure d'arts et métiers - ENSAM, 2018.